UC Berkeley
UC Berkeley Electronic Theses and Dissertations

Title
Precision measurement of the fine-structure constant with atom interferometry

Permalink
https://escholarship.org/uc/item/4nm4g4dt

Author
Zhong, Weicheng

Publication Date
2020

Peer reviewed|Thesis/dissertation

Precision measurement of the fine-structure constant with atom interferometry

by

Weicheng Zhong

A dissertation submitted in partial satisfaction of the

requirements for the degree of

Doctor of Philosophy

in

Physics

in the

Graduate Division

of the

University of California, Berkeley

Committee in charge:

Professor Holger Müller, Chair
Professor Hartmut Häffner
Professor Eli Yablonovitch

Fall 2020

Precision measurement of the fine-structure constant with atom interferometry

Abstract

Precision measurement of the fine-structure constant with atom interferometry

by

Weicheng Zhong

Doctor of Philosophy in Physics

University of California, Berkeley

Professor Holger Müller, Chair

The fine-structure constant α is ubiquitous in physics, and a comparison among different experiments provides a powerful test of the Standard Model of particle physics. We have recorded the most accurate measurement of $\alpha = 1/137.035999046(27)$ at an accuracy of 0.20 parts per billion (ppb) via measuring h/m_{Cs}, the quotient of the Planck constant and the mass of a cesium-133 atom. Our tools are simultaneous conjugate Ramsey-Bordé atom interferometers based on a cesium atomic fountain. Using Bragg diffraction and Bloch oscillations, we have demonstrated the largest phase (12 million radians) of any Ramsey-Bordé interferometer and controlled the systematic effects at a level of 0.12 ppb. Comparing the Penning trap measurements with the Standard Model prediction of the electron gyromagnetic moment anomaly a_e based on our α result, a 2.5-σ tension has been observed. This tension provides hints for new physics beyond the Standard Model.

One of the largest systematic effects of our α measurement comes from the gravity gradient γ. In order to suppress this effect in the next-generation α measurement, we have demonstrated a new atom interferometer configuration - offset simultaneous conjugate interferometers (OSCIs). We create two pairs of simultaneous conjugate interferometers and precisely control the offset between them with Bragg diffraction and Bloch oscillations. The multichannel readouts of OSCIs allow us to not only cancel the effect of γ, but also reduce the undesired diffraction phase from Bragg diffraction beam splitters.

Other ongoing and planned upgrades of the next-generation α measurement have also been presented in this thesis, including an over-sized vacuum chamber and a high-power pulsed laser system. With these upgrades, we expect to improve the accuracy of α by one to two orders of magnitude.

Contents

List of Figures

List of Tables

Acknowledgments

First and foremost, I would like to thank my advisor Prof. Holger Müller for giving me the opportunity to join his group and work on the α project. I would not have accomplished my Ph.D. without his support and guidance.

The α project has a long history. Many researchers have contributed to it. I am extremely grateful to have had the opportunity to work with Richard H. Parker, Chenghui Yu and Zachary Pagel. Richard has taught me how to plan and organize a complicated research project, how to analyze and present experimental data, and how to write a research paper. Chenghui has taught me a lot of experimental skills with great patience. He has shown me the details about the project when I first joined the group. Zachary has worked hard on the new α measurement. He has led and organized the team so that project can still progress even during the COVID pandemic.

I would also like to thank other researchers that I have worked with: Madeline Bernstein, Jack Roth, Andrew Neely, Spencer Kofford, Eric Planz, Aini Xu and Joyce Kwan. I am also grateful for our collaborators from the Lawrence Berkeley National Laboratory: David Brown, Russel Wilcox, Joe Silber, Azriel Goldschmidt and Ian Hinchliffe. I deeply appreciate their contributions to my Ph.D. project.

I also acknowledge my thesis committee: Prof. Hartmut Häffner and Prof. Eli Yablonovitch for providing helpful comments during the preparation of this thesis.

Chapter 1

Introduction

1.1 The Fine Structure Constant α

The fine structure constant α is a fundamental physics constant characterizing the strength of the electromagnetic interaction between elementary charged particles. It relates the binding energy of an electron-proton system to the electron rest energy by the formula

$$hcR_\infty = \frac{1}{2}\alpha^2 m_e c^2,\tag{1.1}$$

where h is the Planck constant, c is the speed of light in vacuum, R_∞ is the Rydberg constant, and m_e is the mass of an electron. Historically, α has been measured by various methods from different fields of physics , such as the AC Josephson effect [92], the quantum Hall effect [44], the electron anomalous magnetic moment effect [86, 39], as well as photon recoil in atom interferometry [91, 16, 66] and so on, see Figure 1.1. The overall agreement of these measurements is a powerful confirmation of the consistency of theory and experiment across physics. In particular, two types of measurements have been prevailed in their accuracy in the past two decades. The first one is determining α from measurements of the electron anomalous magnetic moment $a_e = (g_e-2)/2$ by using the Standard Model of particle physics, including quantum electrodynamics to the fifth order and muonic as well as hadronic physics (the red data points in Figure 1.1) [5, 54]. The second one is based on the measurements of the quotient of the Planck constant and the mass of a neutral atom h/m_{At} in atom interferometry (the green data points in in Figure 1.1) [91]. Comparison of the results from these two kinds of experiments provides a stringent test of the Standard Model and is a powerful probe for new physics beyond.

We have demonstrated the most accurate measurement of α

$$\frac{1}{\alpha} = 137.035999046(27)$$

with an accuracy of 0.20 parts per billion (ppb) through measuring h/m_{Cs} using an atom interferometer, where m_{Cs} is the mass of a cesium-133 atom [66].
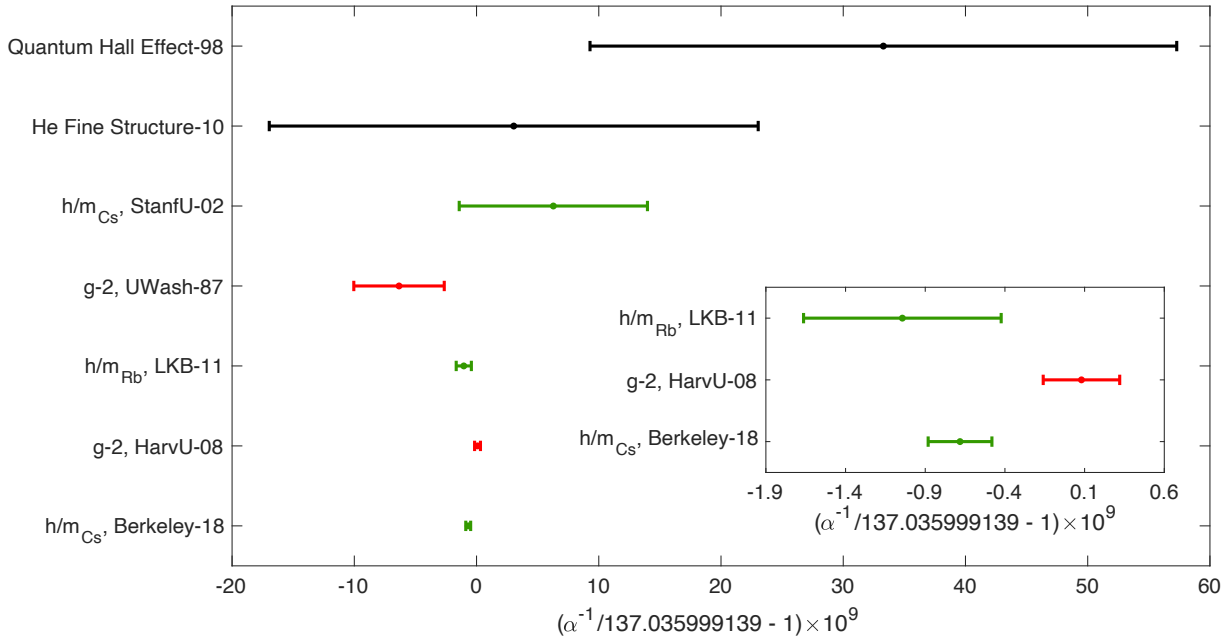
Figure 1.1: Results of selected α measurements, plotted as $\delta\alpha/\alpha$ on a relative scale in parts per billion [86, 92, 44, 51, 91, 39, 16, 66]. "0" on the plot is the CODATA 2014 recommended value [57]. The green points are from photon recoil experiments; the red ones are from electron $g_e - 2$ measurements. The inset is a close-up view of the bottom three measurements. Error bars indicate 1σ uncertainty. Berkeley-18 measurement is the one that we will talk about in this thesis.

1.2 Testing the Standard Model through a_e

In the Standard Model of particle physics, the electron's gyromagnetic anomaly a_e can be expressed as a function of α. Its contributions come from three types of interactions, electromagnetic, electroweak and hadronic [5]:

$$a_e(\alpha) = a_e(\text{QED}) + a_e(\text{weak}) + a_e(\text{hadron}). \qquad (1.2)$$

The dominant contribution $a_e(\text{QED})$ can be expanded as a power series of α,

$$a_e(\text{QED}) = \sum_{n=1}^{\infty} A_e^{(2n)} \left(\frac{\alpha}{\pi}\right)^n + \sum_{n=1}^{\infty} A_{\mu,\tau}^{(2n)} \left(\frac{m_e}{m_\mu}, \frac{m_e}{m_\tau}\right)^{(2n)} \left(\frac{\alpha}{\pi}\right)^n. \qquad (1.3)$$

The first series on the RHS of the above equation is the mass-independent contribution of the electron sector of the Standard Model. Each nth-order term is the sum of all n^{th} order Feynman diagrams. The coefficients $A_e^{(2n)}$ have been analytically calculated up to the 4th order, and a numerical calculation of the 5th order (involving $> 10{,}000$ Feynman diagrams)

with certain theoretical uncertainty is also available. The second series is the contribution of the muon and tauon. It is a function of lepton mass ratios. Its terms have been calculated up to the 4th order and contribute only a negligible uncertainty [5, 4, 3]. All these contributions to a_e as well as their uncertainties are summarised in Figure 1.2.

Based on this theory, an experimental measurement of a_e can be used to derive α under the framework of the Standard Model. An accuracy of 0.24 ppb has been achieved along this path [39, 3, 57]. Alternatively, if an independent measurement of α using other methods, e.g., measurements of h/m_{At} using atom interferometry, is available, one can plug α into Equation 1.2 to theoretically predict $a_e(\alpha)$, and compare it to experimental measurements. This kind of comparison is sensitive to a broad range of previously unmeasurable physics, both within the Standard Model and beyond. Within the Standard Model, it provides a stringent test of our understanding of QED theory as well as electroweak and hadronic physics; beyond the Standard Model, it can provide hints for dark-sector particles, such as dark photons and dark-axial bosons (see Section 4.6).

1.3 Measuring α using h/m_{At}

Atom interferometers measure α based on measuring the recoil kinetic energy transferred from or to an atom of mass m_{At} after scattering a photon that carries momentum $\hbar k$ [91, 16, 66], where $\hbar = h/2\pi$ is the reduced Plance constant and k is the photon wavenumber. This recoil kinetic energy is given by $\hbar\omega_r$, where

$$\omega_r = \frac{\hbar k^2}{2m_{\text{At}}} \tag{1.4}$$

is the recoil frequency. With an accurate monitor of k by an optical frequency comb, h/m_{At} can therefore be measured [91, 16, 66]. α is then determined via the relationship

$$\alpha^2 = \frac{2R_\infty}{c} \frac{m_{\text{At}}}{m_e} \frac{h}{m_{\text{At}}} \tag{1.5}$$

Here the speed of light c is a defined constant with no uncertainty; the Rydberg constant R_∞ is known to 3 ppt accuracy [57]. The atom-to-electron mass ratio m_{At}/m_e is expressed as

$$\frac{m_{\text{At}}}{u} \frac{u}{m_e}$$

where u is the atomic mass unit. The cesium mass m_{Cs}/u is known to 0.06 ppb accuracy [8] and the electron mass m_e/u is known to 29 ppt accuracy [57]. The overall accuracy of α is limited by h/m_{At}.

The determination of R_∞ from hydrogen and deuterium spectroscopy includes corrections from the Lamb shift using QED theory [78]. The most accurate determination of the electron's atomic mass m_e/u requires a calculation of a g-factor where QED is needed [35]. The QED contributions to α in Equation 1.5 through these quantities are of order 1 ppm.
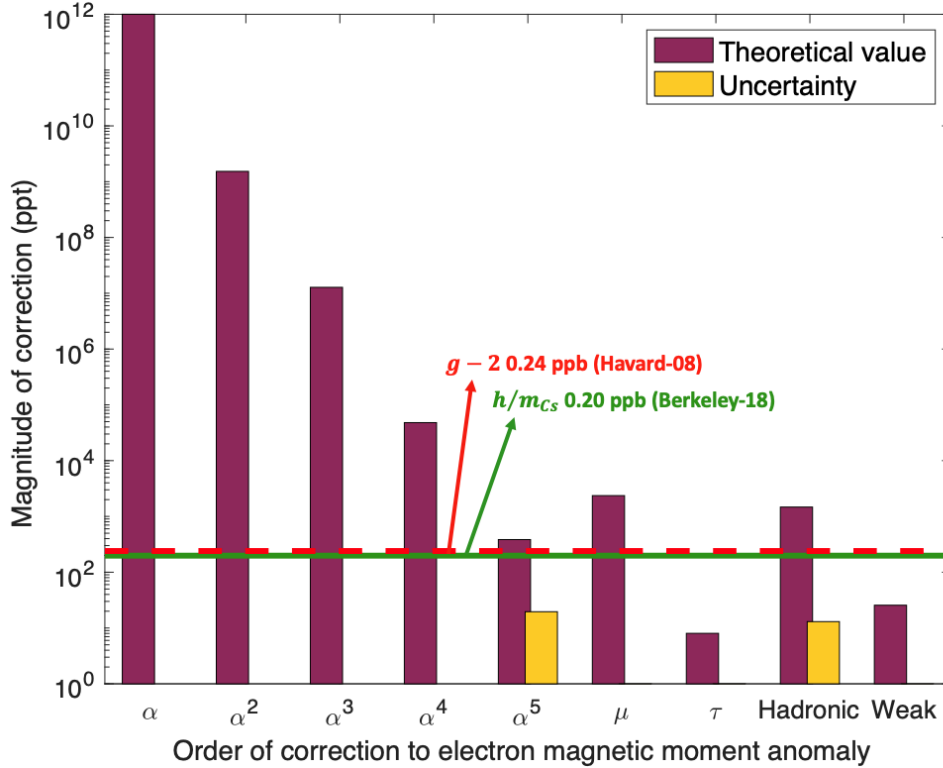
Figure 1.2: Magnitude of contributions to the electron's magnetic-moment anomaly $(a_{e, \text{term}}/a_{e, \text{total}})$ in the unit of part-per-trillion (ppt). Terms labeled from α to α^5 are contributions from mass-independent QED terms. Mass-dependent QED contributions from muon and tauon are labeled as μ and τ, respectively. Contributions from weak interaction as well as hadronic physics are also labeled accordingly. Red bars show the magnitude and orange ones the uncertainty $(\delta a_{e, \text{term}}/a_{e, \text{total}})$. The red dashed line indicates the uncertainty of the Harvard a_e measurement. The green dashed line indicates the calculated uncertainty using our fine structure constant value.

But the uncertainties of these contributions are of order 1 ppt, much smaller than the uncertainty of h/m_{At}. A measurement of h/m_{At} from atom interferometry is free from QED. The predicted a_e using α from Equation 1.5 therefore provides a test of the QED theory when compared to its experimental measurements. The sensitivity of this kind of comparison is currently at the order of 0.2 ppb, limited by the accuracy of penning trap measurements of a_e and atom interferometry measurements of h/m_{At}.

Before our measurement, an accuracy of 0.62 ppb in α has been achieved at Laboratoire Kastler Brossel (LKB) by rubidium-h/m_{Rb} measurements [16]. In our recent measurement

using cesium atoms, we have recorded

$$\frac{h}{m_{\mathrm{Cs}}} = 3.0023694721(12) \times 10^{-9} \ \mathrm{m^2/s} \tag{1.6}$$

with an accuracy of 0.40 ppb. The overall accuracy of α thus has reached 0.20 ppb [66]. One of the largest systematic effects of our measurement comes from the gravity gradient γ. In order to suppress this effect, we have demonstrated a new atom interferometer configuration - offset simultaneous conjugate interferometers (OSCIs) (see Chapter 5). This geometry paves the way for measurements of α below the 20-ppt level.

One may think h/m_{Cs} can be calculated directly using the values of h and m_{Cs}. However, in the old international system of units (SI), h has an uncertainty of 1.2 ppb; m_{Cs} can be calculated via the relationship $m_{\mathrm{Cs}} = m_{\mathrm{Cs}}/u \times u$, and the atomic mass unit u has an uncertainty of 12 ppb [57]. It turns out more accurate to measure the quotient h/m_{Cs} as a whole. In the new SI system adopted in 2019, the Planck constant is defined to have the exact value $h = 6.62607015 \times 10^{-3}$ J $\cdot$ s [1]. Measuring h/m_{At} now can be interpreted as measuring the mass of a neutral atom m_{At}.

The vacuum permeability μ_0 used to have an exact defined value $\mu_0 = 4\pi \times 10^{-7}$ H/m. This is not true since the new SI system. μ_0 is related to α via the relationship

$$\mu_0 = \frac{2\alpha}{e^2} \frac{h}{c}. \tag{1.7}$$

In the new SI system, since e, h and c now have exact values, μ_0 is directly proportional to α. A measurement of α is also a measurement of μ_0. This also applies to the vacuum permittivity $\epsilon_0 = 1/(\mu_0 c^2)$. In CODATA 2018 recommended values, μ_0 and ϵ_0 both have an uncertainty of 0.15 ppb, the same as α.

1.4 Outline of this Thesis

In Chapter 2, we review the basic theory of atom interferometry. In Chapter 3, we introduce the apparatus as well as the timing sequence used in the experiments. Chapter 4 will focus on our α measurement. The theory and the apparatus of this measurement have been documented in Reference [96, 52, 29]. The implications of the result have been discussed in Reference [96]. However, the data collection and analysis procedures have not been documented yet. We will present these details in this chapter. Chapter 5 talks about OSCIs, which will be employed in the next-generation α measurement to cancel the systematic effects from gravity gradient. Finally, in Chapter 6 we will introduce other progress towards the next-generation α measurement.

---

[1]https://physics.nist.gov/cgi-bin/cuu/Value?h

Chapter 2

Theory

2.1 Overview

Atom interferometers are powerful tools for practical applications as well as fundamental physics experiments. They have been used for inertial sensing [70, 37, 82, 27, 94], testing Einstein's Equivalence Principle (EEP) [34, 77, 83, 99, 26], measuring Newton's gravitational constant G [32, 75], and searching for dark-sector particles [28, 38]. Similar to an optical interferometer, an atom interferometer splits matter waves into different paths and recombines them in a coherent manner [46]. Sequences of laser pulses are used to split, direct and recombine the atomic matter waves along different trajectories, acting as beam splitters and mirrors. Through measuring the resulting interference fringes, we can extract the phase difference accumulated between the waves on the paths. Quantities that enter this phase difference then can be accurately determined.

In the simplest scenario, consider an atom initially in some state $|\psi_1\rangle$. A beam splitter, which usually consists of a pair of counter-propagating laser pulses with specifically chosen durations, frequencies, polarizations and intensities, will drive this atom into a superposition of two states $|\psi_1\rangle$ and $|\psi_2\rangle$ with equal probability. The two states have different momenta due to photon recoils. So the trajectories of the two states start to split, forming the two arms of the interferometer. More beam splitters and mirrors are then applied to control the trajectories of the two arms. The trajectories will also be affected by external potentials, such as gravity. During this process, the states in the two arms will acquire phase differently due to various mechanisms. In the end, a final beam splitter is applied when the two arms overlap to mix the wave functions of the two arms, resulting in two output ports. The probability of detecting the atom from each of them then will be a function of the phase difference accumulated between the two arms. Mathematically, this process can be described as

$$|\psi_f\rangle = \hat{U}_{\text{Splitter}} \hat{U}_{\text{Evolution}} \hat{U}_{\text{Splitter}} |\psi_i\rangle , \tag{2.1}$$

where $|\psi_i\rangle$ is the initial state of the atom

$$\psi_i = \begin{bmatrix} 1 \\ 0 \end{bmatrix}, \tag{2.2}$$

$\hat{U}_{\text{Splitter}}$ represents the beam splitter

$$\hat{U}_{\text{Splitter}} = \frac{1}{\sqrt{2}} \begin{bmatrix} 1 & i \\ i & 1 \end{bmatrix}, \tag{2.3}$$

and $\hat{U}_{\text{Evolution}}$ summarizes the phases that two arms acquire between the initial and final beam splitters

$$\hat{U}_{\text{Evolution}} = \begin{bmatrix} e^{i\phi_1} & 0 \\ 0 & e^{i\phi_2} \end{bmatrix}. \tag{2.4}$$

Substituting the above operators into Equation 2.1, the final state of the atom is

$$\psi_f = \frac{1}{2} \begin{bmatrix} e^{i\phi_1} - e^{i\phi_2} \\ ie^{i\phi_1} + ie^{i\phi_2} \end{bmatrix}. \tag{2.5}$$

The probability of the atom being in each state is

$$P_1 = |\langle \psi_1 | \psi_f \rangle|^2 = \sin^2 \frac{\Delta\phi}{2}, \tag{2.6a}$$

$$P_2 = |\langle \psi_2 | \psi_f \rangle|^2 = \cos^2 \frac{\Delta\phi}{2}, \tag{2.6b}$$

where $\Delta\phi = \phi_1 - \phi_2$ is the differential phase acquired between the two arms. We see that the probabilities P_1 and P_2 are functions of $\Delta\phi$. By measuring P_1 and P_2, $\Delta\phi$ can therefore be determined.

To read out these probabilities, we usually manipulate millions to billions of atoms at one time, and measure the atom population in each state after interference. To get rid of the dependence of the signal on the total population, which may vary from shot to shot because of instabilities in experiments, we usually do a relative measurement

$$I = \frac{N_1 - N_2}{N_1 + N_2} = C \cdot \cos(\phi_1 - \phi_2) + O, \tag{2.7}$$

where N_1 and N_2 are the atom populations in the two states after interference, and they are respectively proportional to the probabilities P_1 and P_2; C is the contrast; O is some offset.

Generally speaking, the phase that an atom acquires during this process can be attributed into two sources: the free evolution phase and the atom-light interaction phase. The calculation of the free evolution phase is reviewed in Section 2.2. Mechanisms of two types of beam splitters, namely Raman transition and Bragg diffraction, and their associated atom-light interaction phases are introduced in Section 2.3 and 2.4. Different geometries of atom interferometers have different applications. In Section 2.5, we will talk about Mach-Zehnder interferometers. In particular, Ramsey-Bordé interferometers have been used for the α measurement. It will be introduced in Section 2.6.

2.2 Free Evolution Phase

Consider an atom with mass m that evolves in a potential $V(z)$. The Lagrangian describing this system is

$$L(z, \dot{z}) = \frac{1}{2}m\dot{z}^2 - V(z). \tag{2.8}$$

Assume initially the atom is in state $|\psi(z_a, t_a)\rangle$ at space-time (z_a, t_a). According to Feynman's formulation of quantum mechanics, the wave function $|\psi(z_b, t_b)\rangle$ at space-time (z_b, t_b) is given by

$$|\psi(z_b, t_b)\rangle = e^{iS_{cl}/\hbar} |\psi(z_b, t_b)\rangle, \tag{2.9}$$

where S_{cl} is the the classical action

$$S_{cl}[t_a, z_a; t_b, z_b] = \int_{t_a}^{t_b} L[z(t), \dot{z}(t)]dt. \tag{2.10}$$

Here $z(t)$ and $\dot{z}(t)$ are the classical trajectory and velocity. They can be derived from the Euler-Lagrange equation

$$\frac{\partial L}{\partial z} - \frac{d}{dt}\frac{\partial L}{\partial \dot{z}} = 0. \tag{2.11}$$

Therefore, the free evolution phase that an atom interferometer measures can be easily determined by calculating the difference between the classical actions of the two arms of the interferometer

$$\phi_{\text{free}} = \frac{S_{cl}^1 - S_{cl}^2}{\hbar}. \tag{2.12}$$

One caveat is that Equation.2.9 only holds when the Lagrangian has a quadratic form with respect to z and $\dot{z}$ [81]. One simple example of this kind of Lagrangian is an atom in a uniform gravitational field

$$L(z, \dot{z}) = \frac{1}{2}m\dot{z}^2 - mgz. \tag{2.13}$$

When the Lagrangian is not quadratic, corrections to Equation 2.9 will be required. But we will not talk about that here.

The Lagrangian in Equation 2.13 is of particular importance, as many atom interferometer experiments are performed in ultra-high vacuum environment where the only significant potential that atoms sense is gravity. However, one limitation of Equation 2.13 is that it assumes a uniform gravitational field. In reality, gravity is different at different heights on the earth. Usually, we will need to expend gravity to first order

$$g(z) = g + \gamma z, \tag{2.14}$$

where the constant γ is the gravity gradient. We will treat the effect of gravity gradient as a perturbation to the original Lagrangian. This perturbation is given by

$$\delta L(z) = \frac{1}{2}m\gamma z^2. \tag{2.15}$$

According to the perturbation theory, the phase shift due to perturbations can be calculated by integrating the Lagrangian perturbation along the unperturbed path [81]. Therefore, the phase shift due to gravity gradient is

$$\phi_{\text{free},\gamma} = \frac{1}{\hbar} \int_{t_0}^{t_1} (\delta L[z_1(t)] - \delta L[z_2(t)])dt, \tag{2.16}$$

where z_1 and z_2 are the trajectories of the two arms determined using the unperturbed Lagrangian in Equation 2.13.

2.3 Raman Transition

Before

$$|g_1\rangle, p = 0$$

$$\hbar k_1 \qquad\qquad \hbar k_2$$

After

$$2\hbar k_2 \qquad |g_2\rangle, p = \hbar(k_1 + k_2)$$
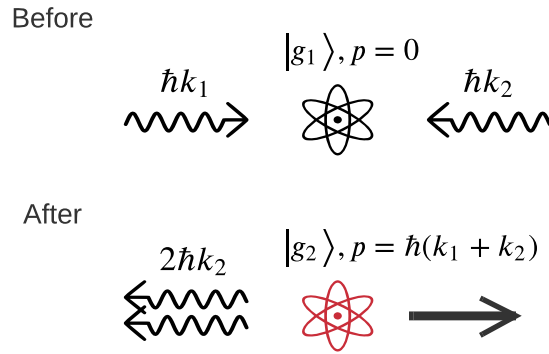
Figure 2.1: An atom undergoes stimulated Raman transition. The atom absorbs a photon with wave vector k_1, and emits a photon with wave vector k_2 in the other direction via stimulated emission. This process drives the atom to another hyperfine state, transfers the photon momentum to the atom due to momentum conservation, and imprints a laser phase on the atom's wave function.

Stimulated Raman transition is an important technique used in atom interferometry to split atomic wave functions coherently. Imagine an atom initially in an electronic state $|g_1\rangle$ has momentum $p = 0$. The atom is illuminated by two counter-propagating laser pulses, as shown in Figure 2.1. The two laser pulses have frequencies ω_1 and ω_2, respectively. Their wave vectors are k_1 and k_2, respectively. We can define an effective frequency $\omega_{\text{eff}} = \omega_1 - \omega_2$, and an effective wave vector $k_{\text{eff}} = k_1 + k_2$. If ω_{eff} is close to the splitting between $|g_1\rangle$ and another hyperfine state $|g_2\rangle$, the atom will absorb a photon with frequency ω_1, and emit a photon with frequency ω_2 via stimulated emission. After this process, the atom will be driven to $|g_2\rangle$. The momentum of the atom will change by $\hbar k_{\text{eff}}$ due to momentum conservation. This process is also coherent. It will change the phase of the atomic wave function by $\phi_1 - \phi_2$, where ϕ_1 and ϕ_2 are the phases of the two photons. The probability of this process can be well controlled by the duration, frequency and intensity of the laser pulses. Due to these

properties, stimulated Raman transition is an ideal candidate for beam splitters in atom interferometry.
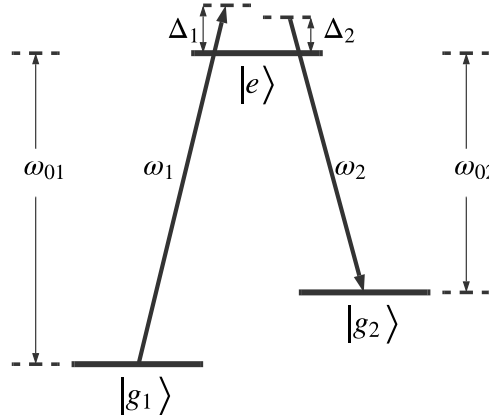
Figure 2.2: Atomic energy level structure of a three-level system. Two ground states $|g_1\rangle$ and $|g_2\rangle$ are coupled to an excited state $|e\rangle$ by two optical fields. The population can be driven between the ground stats as in an effective two-level system.

To understand the mechanism of Raman transition, we can model the atom as a three-level system, as shown in Figure.2.2. Taking the hyper-fine excited state $|e\rangle$ to have zero energy, the two hyper-fine ground states $|g_1\rangle$ and $|g_2\rangle$ have internal energy levels as $-\hbar\omega_{01}$ and $-\hbar\omega_{02}$, respectively. Two laser pulses $\boldsymbol{E_1} = \boldsymbol{E_{01}}\cos(k_1 z - \omega_1 t)$ and $\boldsymbol{E_2} = \boldsymbol{E_{02}}\cos(-k_2 z - \omega_2 t)$ couple the ground states to the excited state. Each of them is detuned by Δ_1 or Δ_2 from resonance. The Hamiltonian describing this system can be written as

$$
H = \hbar \begin{bmatrix}
\dfrac{p^2}{2m\hbar} - \omega_{01} & 0 & \dfrac{\Omega_1}{2}e^{-i(k_1 z - \omega_1 t)} \\[3mm]
0 & \dfrac{p^2}{2m\hbar} - \omega_{02} & \dfrac{\Omega_2}{2}e^{-i(-k_2 z - \omega_2 t)} \\[3mm]
\dfrac{\Omega_1^*}{2}e^{i(k_1 z - \omega_1 t)} & \dfrac{\Omega_2^*}{2}e^{i(-k_2 z - \omega_2 t)} & \dfrac{p^2}{2m\hbar}
\end{bmatrix}.
\tag{2.17}
$$

In the above equation, p is the momentum of the center of mass of the atom, and m is the mass of the atom. The diagonal elements describe the free evolution of the atomic wave function, which are combinations of external kinetic energy and internal electronic energy levels; the off-diagonal elements describe the atom-light interactions. Ω_1 and Ω_2 are the single-photon Rabi frequencies defined as

$$
\Omega_\alpha = \frac{-\langle g_\alpha| \, \boldsymbol{E_{0\alpha}} \cdot \boldsymbol{d} \, |e\rangle}{\hbar}.
\tag{2.18}
$$

They describe the strength of the coupling from the ground level $|g_\alpha\rangle$ through field $\boldsymbol{E_\alpha}$ to the excited level $|e\rangle$ ($\alpha = 1$ or 2). In practice, the intensity of the laser pulses is not very

high and the detuning is much less then the resonant frequency $\Delta_\alpha \ll \omega_{0\alpha}$, so we have used the dipole and rotating-wave approximations in the above Hamiltonian [80]. We have also assumed the cross-couplings, such as coupling between $|g_2\rangle$ and $|e\rangle$ through $\boldsymbol{E_1}$ or coupling between $|g_1\rangle$ and $|e\rangle$ through $\boldsymbol{E_2}$, are negligible. We also neglect spontaneous emission since the laser pulses are usually detuned far enough $\Delta_\alpha \gg \Gamma$ (Γ is spontaneous decay rate of the excited state $|e\rangle$).

The state vector of the atomic wave function can be factored into the external components $|p\rangle$ and the internal components $|\alpha\rangle$. Notice that when the atom absorbs or emits a photon, the atom will acquire or lose the photon's momentum, due to momentum conservation. If we define the momentum of state $|g_1\rangle$ as p_0, then the momentum of state $|e\rangle$ and state $|g_2\rangle$ will be $p_0 + \hbar k_1$ and $p_0 + \hbar k_{\text{eff}}$, respectively. Therefore, we can write the state vector as $|\psi\rangle = c_1 |g_1, p_0\rangle + c_e |e, p_0 + \hbar k_1\rangle + c_2 |g_2, p_0 + \hbar k_{\text{eff}}\rangle$, or in the matrix form

$$|\psi\rangle = \begin{bmatrix} c_1 \\ c_2 \\ c_e \end{bmatrix}. \tag{2.19}$$

The coefficients c_α carry the time dependence of the state.

The evolution of the state can be solved from the Schrödinger equation

$$i\partial_t |\psi\rangle = H |\psi\rangle. \tag{2.20}$$

One thing that complicates the Schrödinger equation is that the Hamiltonian in Equation 2.17 is time dependent. It involves oscillatory terms at optical frequencies. To simplify the math, we usually apply a unitary transformation

$$U = \begin{bmatrix} e^{-i\omega_1 t} & 0 & 0 \\ 0 & e^{-i\omega_2 t} & 0 \\ 0 & 0 & 1 \end{bmatrix} \tag{2.21}$$

to the Hamiltonian and the state vector. The transformation rule for the Hamiltonian is $\tilde{H} = UHU^\dagger + i\hbar(\partial_t U)U^\dagger$, and for the state vector $|\tilde{\psi}\rangle = U |\psi\rangle$. Under this transformation, the Hamiltonian becomes

$$\tilde{H} = \hbar \begin{bmatrix} \dfrac{p^2}{2m\hbar} + \Delta_1 & 0 & \dfrac{\Omega_1}{2}e^{-ik_1 z} \\ 0 & \dfrac{p^2}{2m\hbar} + \Delta_2 & \dfrac{\Omega_2}{2}e^{ik_2 z} \\ \dfrac{\Omega_1^*}{2}e^{ik_1 z} & \dfrac{\Omega_2^*}{2}e^{-ik_2 z} & \dfrac{p^2}{2m\hbar} \end{bmatrix}. \tag{2.22}$$

The state vector becomes

$$|\tilde{\psi}\rangle = \begin{bmatrix} \tilde{c}_1 \\ \tilde{c}_2 \\ c_e \end{bmatrix} = \begin{bmatrix} e^{-i\omega_1 t}c_1 \\ e^{-i\omega_2 t}c_1 \\ c_e \end{bmatrix}. \tag{2.23}$$

We see that under this transformation, the time-dependent terms in the atom-light interaction part are gone. This transformation is the so-called rotating frame transformation, as in this frame, the ground state $|g_\alpha\rangle$ is rotating with the optical frequency ω_α, or equivalently, its electronic energy level is shifted up by $\hbar\omega_\alpha$. From here on, our derivation will be in this rotating frame. The tilde symbol will be omitted for brevity.

Let's plug the Hamiltonian and the state vector into the Schrödinger equation and write down the equation of motion for each state explicitly,

$$i\hbar\dot{c}_1 = [\frac{p_0^2}{2m} + \hbar\Delta_1 - \hbar\Delta]c_1 + \frac{\hbar\Omega_1}{2}e^{-ik_1z}c_e, \tag{2.24a}$$

$$i\hbar\dot{c}_2 = [\frac{(p_0 + \hbar k_{\text{eff}})^2}{2m} + \hbar\Delta_2 - \hbar\Delta]c_2 + \frac{\hbar\Omega_2}{2}e^{ik_2z}c_e, \tag{2.24b}$$

$$i\hbar\dot{c}_e = [\frac{(p_0 + \hbar k_1)^2}{2m} - \hbar\Delta]c_e + \frac{\hbar\Omega_1^*}{2}e^{ik_1z}c_1 + \frac{\hbar\Omega_2^*}{2}e^{-ik_2z}c_2. \tag{2.24c}$$

Here we have shifted all energy levels by $-\hbar\Delta$, where $\Delta = (\Delta_1 + \Delta_2)/2$ (equivalently, we added an phase term $e^{i\Delta t}$ to all states). From the equations above, we see that the excited state evolves with a natural frequency $|\Delta|$, while the two ground states evolving with frequencies $|\Delta_\alpha - \Delta|$. Usually $|\Delta_1 - \Delta_2| \ll |\Delta|$, so the excited state evolves much faster than the two ground states. We can assume c_e damps to equilibrium instantaneously compared to c_1 and c_2, thus can be eliminated adiabatically ($\dot{e} = 0$). Also notice that $p^2/2m \ll \hbar|\Delta|$ ($p^2/(2m\hbar)$ is usually around $\sim$ kHz for atoms moving at velocities of $\sim$ mm/s, and $|\Delta|$ is at the level of $\sim$ 10 MHz). From Equation 2.24c we have

$$c_e \approx \frac{\Omega_1^*}{2\Delta}e^{ik_1z}c_1 + \frac{\Omega_2^*}{2\Delta}e^{-ik_2z}c_2. \tag{2.25}$$

Substituting the above equation into Equation 2.24a and Equation 2.24b, we get

$$i\hbar\dot{c}_1 = [\frac{p_0^2}{2m} + \hbar\Delta_1 + \hbar\omega_{\text{AC1}}]c_1 + \frac{\hbar\Omega_R}{2}e^{-ik_{\text{eff}}z}c_2,$$

$$i\hbar\dot{c}_2 = [\frac{(p_0 + \hbar k_{\text{eff}})^2}{2m} + \hbar\Delta_2 + \hbar\omega_{\text{AC2}}]c_2 + \frac{\hbar\Omega_R^*}{2}e^{ik_{\text{eff}}z}c_e,$$

or in the matrix form

$$i\hbar\frac{d}{dt}\begin{bmatrix} c_1 \\ c_2 \end{bmatrix} = \begin{bmatrix} \frac{p_0^2}{2m} + \hbar\Delta_1 + \hbar\omega_{\text{AC1}} & \frac{\hbar\Omega_R}{2}e^{-ik_{\text{eff}}z} \\ \frac{\hbar\Omega_R^*}{2}e^{ik_{\text{eff}}z} & \frac{(p_0 + \hbar k_{\text{eff}})^2}{2m} + \hbar\Delta_2 + \hbar\omega_{\text{AC2}} \end{bmatrix}\begin{bmatrix} c_1 \\ c_2 \end{bmatrix}. \tag{2.27}$$

Here we have removed the energy shift $\hbar\Delta$. ω_R is the two-photon Rabi frequency defined as

$$\omega_R = \frac{\Omega_1\Omega_2^*}{2\Delta}, \tag{2.28}$$

and the ac-Stark shift

$$\Omega_{\mathrm{AC}\alpha} = \frac{\|\Omega_\alpha\|^2}{4\Delta}.$$ (2.29)

Equation 2.27 is just the Schrödinger equation of an effective two-level system with the state vector $|\psi_{\mathrm{eff}}\rangle = c_1 |g_1, p_0\rangle + c_1 |g_2, p_0 + \hbar k_{\mathrm{eff}}\rangle$ and the Hamiltonian

$$H_{\mathrm{eff}} = \hbar \begin{bmatrix} \dfrac{p^2}{2m\hbar} + \Delta_1 + \omega_{\mathrm{AC1}} & \dfrac{\Omega_R}{2} e^{-ik_{\mathrm{eff}}z} \\ \dfrac{\Omega_R^*}{2} e^{ik_{\mathrm{eff}}z} & \dfrac{p^2}{2m\hbar} + \Delta_2 + \omega_{\mathrm{AC2}} \end{bmatrix}.$$ (2.30)

Solution to a two-level system can be found in many literatures [80]. Assuming the initial condition as $c_{1,0}$ and $c_{2,0}$, we have

$$\begin{bmatrix} c_1(t) \\ c_2(t) \end{bmatrix} = \begin{bmatrix} \cos\dfrac{\tilde{\Omega}t}{2} - i\dfrac{\Delta_R}{\tilde{\Omega}}\sin\dfrac{\tilde{\Omega}t}{2} & -i\dfrac{\Omega_R}{\tilde{\Omega}}e^{-ik_{\mathrm{eff}}z}\sin\dfrac{\tilde{\Omega}t}{2} \\ -i\dfrac{\Omega_R^*}{\tilde{\Omega}}e^{ik_{\mathrm{eff}}z}\sin\dfrac{\tilde{\Omega}t}{2} & \cos\dfrac{\tilde{\Omega}t}{2} + i\dfrac{\Delta_R}{\tilde{\Omega}}\sin\dfrac{\tilde{\Omega}t}{2} \end{bmatrix} \begin{bmatrix} c_{1,0} \\ c_{2,0} \end{bmatrix},$$ (2.31)

where Δ_R is the generalized detuning

$$\begin{aligned} \Delta_R &= (\frac{p_0^2}{2m\hbar} + \Delta_1 + \omega_{\mathrm{AC1}}) - (\frac{(p_0 + \hbar k_{\mathrm{eff}})^2}{2m\hbar} + \Delta_2 + \omega_{\mathrm{AC2}}) \\ &= (\Delta_1 - \Delta_2) + (\omega_{\mathrm{AC1}} - \omega_{\mathrm{AC2}}) - k_{\mathrm{eff}}(v_0 + v_r), \end{aligned}$$ (2.32)

and $\tilde{\Omega}$ the generalized Rabi frequency

$$\tilde{\Omega} = \sqrt{\Delta_R^2 + \|\Omega_R\|^2}.$$ (2.33)

Assuming initially the atom is in the state $|g_1, p_0\rangle$ and $\Delta_R = 0$, we have

$$\begin{bmatrix} c_1(t) \\ c_2(t) \end{bmatrix} = \begin{bmatrix} \cos\dfrac{\tilde{\Omega}t}{2} \\ -i\dfrac{\Omega_R^*}{\tilde{\Omega}}e^{ik_{\mathrm{eff}}z}\sin\dfrac{\tilde{\Omega}t}{2} \end{bmatrix}.$$ (2.34)

We see that the probability in each state $\|c_\alpha\|^2$ oscillates with the frequency $\tilde{\Omega}$. We can thus define a laser pulse with the duration $\pi/\tilde{\Omega}$ as a π-pulse, which will drive the atom from one state to the other state with probability 1. Similarly, we can also define a $\pi/2$-pulse, which has a duration $\pi/(2\tilde{\Omega})$. A $\pi/2$ pulse has 50% chance to drive the atom from one state to another. π-pulses and $\pi/2$-pulses are of particular importance in atom interferometry. They work as mirrors and beam splitters as their counterparts in light interferometers. Another thing we should notice is that c_2 has a phase shift $k_{\mathrm{eff}}z$ relative to c_1. That means the atom will acquire the laser phase when it undergoes Raman transition.

So far we have assumed the atom is a three-level system and have neglected other excited states. We have also neglected cross-couplings by assuming electric field E_α only couples $|e\rangle$ and $|g_\alpha\rangle$. In a real precision experiment, these facts will lead to systematic effects like ac-Stark shift, thus need to be treated very carefully.

If the two laser pulses counter-propagate, $k_{\text{eff}} = k_1 + k_2$. The generalized detuning from Equation 2.32 is velocity dependent. Therefore, the driving efficiency of Raman transition depends on an atom's velocity. We will use this property to select a velocity subgroup of atoms from a cold atom cloud, see Section 3.2. On the contrary, if the two laser pulses co-propagate, by replacing k_2 with $-k_2$ in the above derivations, we have $k_{\text{eff}} = k_1 - k_2 \approx 0$. The generalized detuning will be velocity independent. A velocity-independent Raman transition pulse will be used in our experiments as a state selection pulse, see Section 3.2.

Raman transition has its limitations. It only transfers the momentum of two photons every time. This will limit the sensitivity of the atom interferometers. As atoms stay in two different electronic states, there are many associated systematic effects, such as the differential ac-Stark shift. Bragg diffraction has proven to be a beam-splitter technique better in these aspects.

2.4   Bragg Diffraction
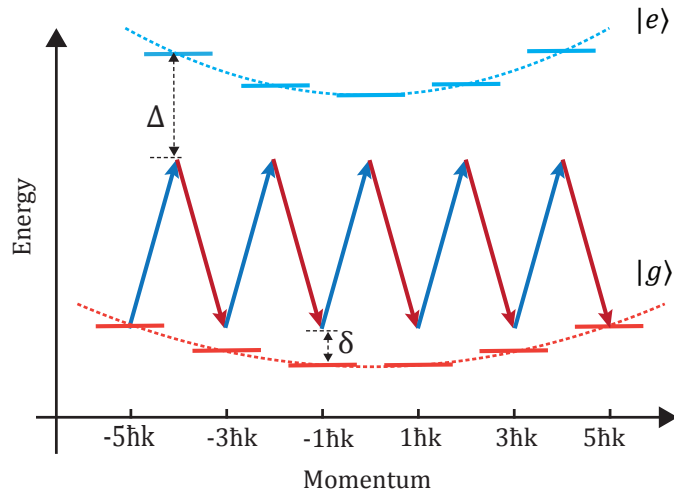
Figure 2.3: 5th-order Bragg diffraction. Counter-propagating laser pulses drive the atom between different momentum states of the same internal electronic ground state. Bragg diffraction will transfer multiple photon momenta every time, and leave the atom in the same internal state during the process.

Much like Raman transition, during Bragg diffraction, an atom is illuminated by a pair of counter-propagating laser pulses with frequency ω_1 and ω_2, respectively. But unlike Raman

transition, the atom absorbs n photons with frequency ω_1 and emits n photons with frequency ω_2 at one time. The internal electronic state of the atom will not change during this process. As the two pulses couple different momentum states of the same internal electronic state, the frequency difference between the two pulses (< 1MHz) is much smaller than the hyper-fine splitting of the atom (~ 10GHz). One easy way to find the resonant condition of Bragg diffraction is to use energy and momentum conservation. Assume the initial and the final velocity of the atom are v_i and v_f. From energy conservation, we have

$$\frac{1}{2}m(v_f^2 - v_i^2) = n\hbar(\omega_1 - \omega_2). \tag{2.35}$$

From momentum conservation, we have

$$m(v_f - v_i) = n\hbar(k_1 + k_2). \tag{2.36}$$

Solving the above two equations, we get

$$v_f = 2nv_r + v_i, \tag{2.37}$$

where $v_r = \hbar(k_1 + k_2)/(2m)$ is the recoil velocity;

$$\omega_1 - \omega_2 = 4(n + n_0)\omega_r, \tag{2.38}$$

where $\omega_r = mv_r^2/2$ is the recoil energy, and n_0 is defined as v_i/v_r.

For a more rigorous derivation, let's study Bragg diffraction in a semi-classical way. Bragg diffraction drives atoms between different momentum states of the same internal state, as shown in Figure 2.3. Here we have chosen a reference frame such that the initial velocity of the atom is zero. Imagine a pair of laser pulses $\boldsymbol{E_1} = \boldsymbol{E_{01}}\cos(kz - \omega t)$ and $\boldsymbol{E_2} = \boldsymbol{E_{02}}\cos(-kz - \omega t)$ are applied on an atom. The two laser beams have the same frequency but opposite wave vectors. The Hamiltonian describing this system is

$$H = \hbar \begin{bmatrix} \dfrac{p^2}{2m\hbar} - \omega_0 & \dfrac{\Omega_1}{2}\mathrm{e}^{-i(kz-\omega t)} + \dfrac{\Omega_2}{2}\mathrm{e}^{-i(-kz-\omega t)} \\ \dfrac{\Omega_1^*}{2}\mathrm{e}^{i(kz-\omega t)} + \dfrac{\Omega_2^*}{2}\mathrm{e}^{i(-kz-\omega t)} & \dfrac{p^2}{2m\hbar} \end{bmatrix}. \tag{2.39}$$

The state vector is $|\psi\rangle = c_g\,|g, p_g\rangle + c_e\,|e, p_e\rangle$, or in the matrix form

$$|\psi\rangle = \begin{bmatrix} c_g \\ c_e \end{bmatrix}. \tag{2.40}$$

Similar to Raman transition, let's first apply a rotating-frame transformation,

$$U = \begin{bmatrix} \mathrm{e}^{-i\omega t} & 0 \\ 0 & 1 \end{bmatrix} \tag{2.41}$$

The Hamiltonian becomes

$$
H = \hbar \begin{bmatrix} \dfrac{p^2}{2m\hbar} + \Delta & \dfrac{\Omega_1}{2}e^{-ikz} + \dfrac{\Omega_2}{2}e^{ikz} \\ \dfrac{\Omega_1^*}{2}e^{ikz} + \dfrac{\Omega_2^*}{2}e^{-ikz} & \dfrac{p^2}{2m\hbar} \end{bmatrix},
\tag{2.42}
$$

and the state vector becomes

$$
|\psi\rangle = \begin{bmatrix} \tilde{c}_g \\ c_e \end{bmatrix} = \begin{bmatrix} e^{-i\omega t}c_g \\ c_e \end{bmatrix}.
\tag{2.43}
$$

Plug the Hamiltonian and the state vector into the Schrödinger equation and write down the equations of motion explicitly, we get

$$
i\hbar\dot{c}_g = \frac{p_g^2}{2m}c_g + \left(\frac{\hbar\Omega_1}{2}e^{-ikz} + \frac{\hbar\Omega_2}{2}e^{ikz}\right)c_e,
\tag{2.44a}
$$

$$
i\hbar\dot{c}_e = \left(\frac{p_e^2}{2m} - \hbar\Delta\right)c_e + \left(\frac{\hbar\Omega_1^*}{2}e^{ikz} + \frac{\hbar\Omega_2^*}{2}e^{-ikz}\right)c_g,
\tag{2.44b}
$$

where we have shifted the energy levels of both electronic state down by $\hbar\Delta$. After adiabatically eliminating the excited state:

$$
c_e = \left(\frac{\Omega_1^*}{2\Delta}e^{ikz} + \frac{\Omega_2^*}{2\Delta}e^{-ikz}\right)c_g,
\tag{2.45}
$$

we get the equation of motion of the ground state

$$
i\hbar\dot{c}_g = -\frac{\hbar^2}{2m}\frac{\partial^2 c_g}{\partial z^2} + \hbar\frac{\|\Omega_1\|^2 + |\Omega_2|^2 + \Omega_1^*\Omega_2 e^{2ikz} + \Omega_1\Omega_2^* e^{-2ikz}}{4\Delta}c_g,
\tag{2.46}
$$

or

$$
i\hbar\dot{c}_g = -\frac{\hbar^2}{2m}\frac{\partial^2 c_g}{\partial z^2} + \hbar\left(\omega_{AC} + \frac{\Omega_R^*}{2}e^{2ikz} + \frac{\Omega_R}{2}e^{-2ikz}\right)c_g,
\tag{2.47}
$$

where the ac-Stark shift ω_{AC} and the two-photon Rabi frequency Ω_R are defined in Equation 2.28 and 2.29.

Equation 2.47 can be viewed as the Schrödinger equation of an atom loaded in periodic optical lattices. Assuming Ω_R is real, the effective potential of the optical latices is $\hbar(\omega_{AC} + \Omega_R\cos 2kz)$. According to Bloch theorem, c_g can be expanded as a sum of Fourier series

$$
c_g = e^{ik_q z}\sum_{l=-\infty}^{\infty} g_{2l}(t)e^{2ilkz},
\tag{2.48}
$$

where the quasi-wavenumber k_q describes the initial velocity of the atom. Each term have different momentum $2l\hbar k$, with g_{2l} the probability amplitude of the atom in that momentum state. Substituting the above solution into Equation 2.47, and factoring out the terms that have the same momentum, we get

$$
i\dot{g}_{2l} = [\omega_r(2l + l_0)^2 + \omega_{AC}]g_{2l} + \frac{\Omega_R^*}{2}g_{2(l-1)} + \frac{\Omega_R}{2}g_{2(l+1)},
\tag{2.49}
$$

where we have defined the recoil frequency $\omega_r = \hbar k^2/2m$ and $l_0 = k_q/k$. This is an infinity set of coupled differential equations. Each of them can be viewed as coupling from g_{2l} to $g_{2(l-1)}$ and $g_{2(l+1)}$ as a two-photon process.

Neglect the ac-Stark shift and assume Ω_R is real. When the duration of the laser pulse is short $t \ll 1/\omega_r$ (the Raman-Nath regime), the frequency spread of the laser pulse is larger than the energy difference between adjacent momentum states, and the kinetic term becomes negligible. Equation 2.49 can be simplified as

$$i\dot{g}_{2l} = \frac{\Omega_R}{2}(g_{2(l-1)} + g_{2(l+1)}). \tag{2.50}$$

This equation can be satisfied by Bessel functions [60]:

$$g_{2l}(t) = (-\mathrm{i})^l J_l(\Omega_R t). \tag{2.51}$$

In this scenario, imagine initially all atoms are in the zero momentum state: $g_0(0) = 1$, $g_{l \neq 0}(0) = 0$. A pulse that has duration τ will drive the atoms to the momentum state $2l\hbar k$ with probability $\|g_{2l}(\tau)\|^2$. Since all momentum states have certain probabilities to be occupied after the pulse, the driving efficiency of the pulse will be low.

On the contrary, if the laser pulse is long enough (the Bragg regime), the momentum state $|p = -n\hbar k\rangle$ will be coupled to the momentum state $|p = n\hbar k\rangle$ due to energy conservation, and all the intermediate states will adiabatically eliminated. Under this limit, the system can be viewed as a two-level system with the effective Rabi frequency [60]

$$\Omega_{\mathrm{eff}} = \frac{\Omega_R^n}{(8\omega_r)^{n-1}} \frac{1}{[(n-1)!]^2}. \tag{2.52}$$

The driving efficiency of such a Bragg pulse will reach 100%.

In a real experiment, the Bragg pulse length is usually set to an intermediate regime. We want the pulse length to be short so that there is less single photon scattering, but not too short so it can still have high driving efficiency. We will also use Gaussian temporal-profile pulses, instead of square pulses, as a square pulse has frequency sidebands that will drive atoms to unwanted momentum states. Therefore, Ω_R will be time-dependent. With these facts, it is hard to find an analytical solution to Equation 2.49. Instead, we solve the truncated equation series numerically. Assume initially atoms are in the $-n$th momentum state. An nth-order Bragg pulse will mostly populate the momentum states between $-n$ and n. We can truncate Equation 2.49 at some limit n_{max} ($n_{max} \geqslant n$). The equation series becomes

$$i\dot{g}_{-n_{max}} = \omega_r n_{max}^2 g_{-n_{max}} + \frac{\Omega_R}{2} g_{-n_{max}+2}$$

$$i\dot{g}_{-n_{max}+2} = \omega_r(-n_{max}+2)^2 g_{-n_{max}+2} + \frac{\Omega_R}{2}(g_{-n_{max}} + g_{-n_{max}+4}),$$

$$i\dot{g}_{-n_{max}+4} = \omega_r(-n_{max}+4)^2 g_{-n_{max}+4} + \frac{\Omega_R}{2}(g_{-n_{max}+2} + g_{-n_{max}+6}),$$

$$\ldots \tag{2.53}$$

$$i\dot{g}_{n_{max}-4} = \omega_r(n_{max}-4)^2 g_{n_{max}-4} + \frac{\Omega_R}{2}(g_{n_{max}-2} + g_{n_{max}-6}),$$

$$i\dot{g}_{n_{max}-2} = \omega_r(n_{max}-2)^2 g_{n_{max}-2} + \frac{\Omega_R}{2}(g_{n_{max}} + g_{n_{max}-4}),$$

$$i\dot{g}_{n_{max}} = \omega_r n_{max}^2 g_{n_{max}} + \frac{\Omega_R}{2} g_{n_{max}-2},$$

where the two-photon Rabi frequency $\Omega_R = \Omega_{R0}\text{Exp}(-t^2/2w^2)$ is now time-dependent and has a Gaussian temporal profile. This set of equations can be solved numerically.

Figure 2.4 shows an example of the effect of a $\pi/2$ 5th-order Bragg diffraction pulse. n_{max} is set to be 11; the amplitude of the time-dependent two-photon Rabi frequency is $\Omega_{R0} = 30.29\omega_r$; the width of the Gaussian temporal profile is $w = 0.23588667\omega_r^{-1}$; and the pulse has a during of $3w$ [95]. The upper plot shows the population change. Atoms are initially in the $n = -5$ state. With the Bragg diffraction pulse, the $n = -5$ and $n = 5$ states are eventually equally populated. During this process, atoms have certain probabilities to be in the intermediate states.

The large-momentum-transfer mechanism of Bragg diffraction improves sensitivity, but also poses challenges. It will lead a systematic effect known as the diffraction phase. For a two-photon process e.g. Raman transition, that only couples two states, if the atom population in one state is $\sin^2\phi$, due to population conservation, the population in the other state must be $\cos^2\phi$. The phase difference between these two state then will always be $\pi/2$. But for Bragg diffraction, this population conservation no longer holds: atoms has certain probabilities to be in unwanted states. The lower plot of Figure 2.4 shows the phase difference between the $n = 5$ state and $n = -5$ state. We see that as the total population in the $n = 5$ state and $n = -5$ state deviates from 1 during the pulse, this differential phase deviates from $-\pi/2$. After the pulse, about 99.4% atoms are either in $n = -5$ or $n = 5$ state. The differential phase between these two states deviates from $-\pi/2$ by 5 mrad. In a real experiment, this diffraction phase depends on a lot of parameters, such as pulse duration, pulse intensity, atom velocity, and so on. It can be as large as several hundred milliradians. This is one of the major systematic sources of our experiment. We will talk about them in detail in subsequent chapters.

Another challenge about Bragg diffraction is that it requires much higher power than Raman transition. Bragg diffraction requires an intensity proportional to n^2 for constant
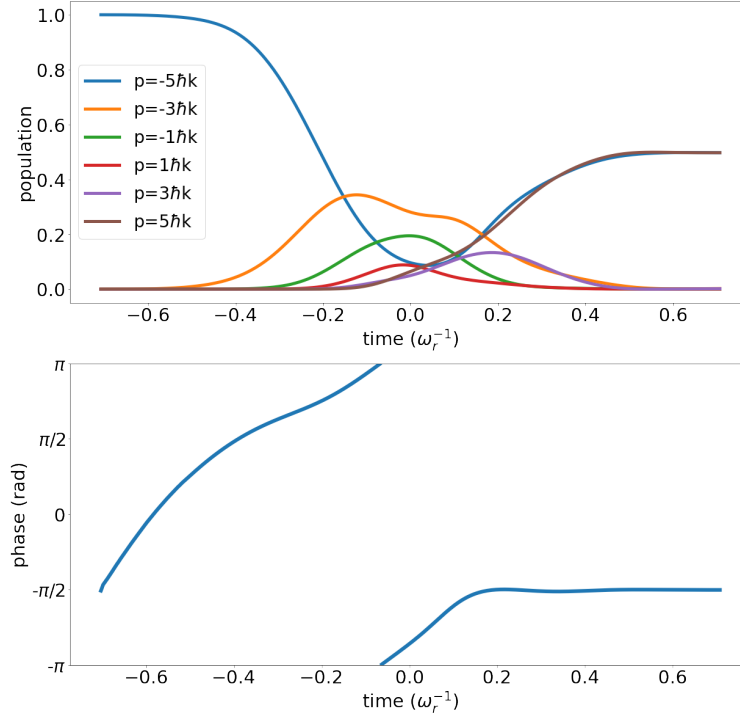
Figure 2.4: Top: The population of different momentum states as a function of time for a Gaussian $\pi/2$ Bragg pulse. The Bragg order $n = 5$. Bottom: The phase difference between the $|p = -5\hbar k\rangle$ momentum state and the $|p = 5\hbar k\rangle$ momentum state as a function of time for the Bragg pulse.

pulse duration, or n^4 for constant single-photon scattering rate at an increased detuning [60]. To drive 5th-order Bragg diffraction in our experiment, we have used Ti:Sapphire lasers which can output up to 6W power. In order to further increase the Bragg order, new laser system that can generate much stronger laser pulses will be required. As a comparison, diode lasers that outputs tens of mW power is able to drive Raman transition in very high precision measurements [69].

2.5 Mach-Zehnder Interferometer

The first interferometer geometry we will look into is the Mach-Zehnder geometry, as shown in Figure 2.5. A Mach-Zehnder interferometer has three evenly-spaced laser pulses. The first pulse is a $\pi/2$-pulse, which splits the atomic wave function into two. The two wave functions travel along different trajectories due to having different momenta. The second pulse is a π-pulse. It acts as a mirror and will reflect both trajectories. The third pulse is another $\pi/2$-pulse. It mixes the wave functions from the two trajectories when they spatially

overlap. When Raman transition is used for beam splitters and mirrors, the phase we can read out from this type of interferometer is

$$\Phi_{\mathrm{MZ}} = kgT^2, \tag{2.54}$$

where k is the wave number of the laser pulse, g is the gravity acceleration, and T is the pulse separation time. As the two arms of the interferometer spend equal amount of time in the two internal electronic and external momentum states, the overall free evolution phase is cancelled between the two arms. Φ_{MZ} comes solely from atom-light interactions.
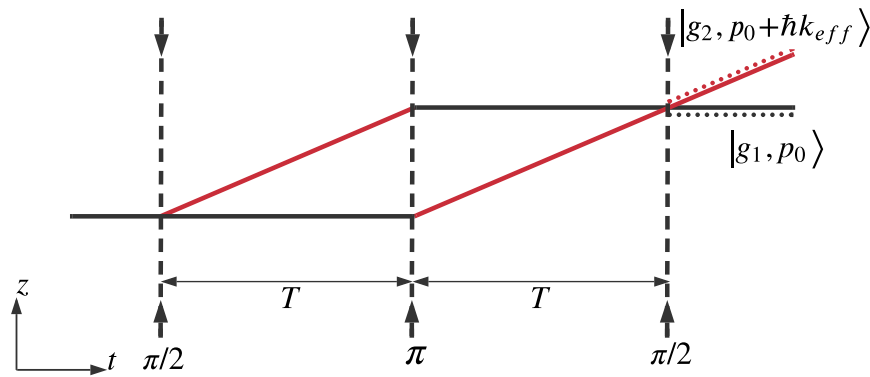
Figure 2.5: A Mach-Zehnder atom interferometer using Raman transition as beam splitters and mirrors. Dashed lines represent pairs of counter-propagating laser pulses. $\pi/2$ Raman pulses act as beam splitters; π Raman pulses act as mirrors.

Since k can be measured very accurately via a frequency comb, Mach-Zehnder interferometers have been applied to measure gravity acceleration g since its first demonstration by Mark Kasevich and Steven Chu at Stanford in 1991 [46]. There have also been many variations of this type of experiment. For example, experiments that run Mach-Zehnder interferometers with different distances to a source mass have been used to measure the Newton's gravitational constant G [32], and detect dark matter and dark energy [28]; experiments that perform Mach-Zehnder interferometers with different species of atoms have been used to test Einstein's Equivalence principle [99]. There are also proposals for detecting gravitational waves using Mach-Zehnder interferometers [41]. In our measurement of the fine structure constant α, we use Bragg diffraction as beam splitteres and run two Mach-Zehnder interferometers at different heights simultaneously. By taking the differential phase between the two interferometers, we measured the gravity gradient γ, which is one of the largest systematic source in our measurement of α, see Section 4.5.

2.6   Ramsey-Bordé Interferometer

History

Our measurement of α is based on the Ramsey-Bordé configuration. Before we introduce the theory, let's first review the its history.

Ramsey-Bordé atom interferometers were first proposed by Christian J. Bordé in 1989 as a tool for measuring acceleration and rotation [7]. In his proposal, the atom source came from a thermal atomic beam and the beam splitters were effected by Raman transitions. The experiment was later realized by F. Riehle *et al* from J. Helmcke's group [73].

In 1993, David Weiss, Brenton Young and Steven Chu from Stanford demonstrated this interferometer configuration using laser-cooled atoms for the first time, and applied it to the measurement of $\hbar/m_{\mathrm{Cs}}$ [88, 87]. In their experiment, they used Raman transitions as beam splitters. They performed two interferometers at the same time, but read out the interference fringes from each of them separately.

One year later, Martin Weitz, Brenton Young, and Steven Chu used adiabatic population transfer as beam splitters [90]. Adiabatic population transfer has the advantage over Raman transition of being insensitive to the small changes in experimental parameters such as intensity and frequency of the laser pulses. It is also immune to ac Stark shift, a troublesome systematic effect when using Raman transitions. In 2002, a 7.9ppb accuracy in α was achieved by Andreas Wicht *et al* from Chu's group with this geometry.

Holger Müller, Sheng-wey Chiow *et al* from Chu's group proposed the simultaneous conjugate interferometer configuration to cancel the effects of vibration in 2006. They also proposed to use multi-photon Bragg diffraction as beam splitters to increase the sensitivity of the interferometers [59]. They demonstrated it in 2009 with a Bragg order of $n = 10$ [18].

To further increase the sensitivity and suppress systematic effects, Bloch oscillations were introduced in the geometry by Pei-Chen Kuan, Shau-Yu Lan, Brian Estey and Holger Müller [29, 30] from UC Berkeley. Before the work of this thesis, $n = 8$ for Bragg diffraction and $N = 20$ for Bloch oscillations have been achieved.

Ramsey-Bordé Interferometers with Bragg Diffraction

Figure 2.6 shows a Ramsey-Bordé interferometer using Bragg diffraction as beam splitters. Consider an atom initially in the momentum state $|0\rangle$. An nth-order $\pi/2$ Bragg pulse consisting of frequency ω_1 and ω_2 is applied on the atom and drives it into a superposition of $|0\rangle$ and $|n\rangle$ with equal probability. The two momentum states start to split, forming the two arms of the interferometer. After free-falling for time T, a second $\pi/2$ pulse is applied to split the states into four trajectories. Only the two resulting $|0\rangle$ states will be used to create interference. With another time T', a third $\pi/2$ pulse is applied. The frequency of the down-going component of this Bragg pulse is shifted by ω_m so that it drives Bragg diffraction in the other direction. The upper arm now is in the $|-n\rangle$ state. Finally, after time T, a forth $\pi/2$ pulse which is identical to the third one is used to combine the wave packets to create

interference. Since we use Bragg diffraction as beam splitters, the atom stays in the same internal electronic state during the whole process. We will have to wait for enough time for the wave packets to be spatially resolved so that we can read out interference fringes. According to Equation 2.38, the resonant condition of Bragg diffraction, the frequencies of the laser pulses should satisfy $\omega_1 - \omega_2 = 4n\omega_r$ and $\omega_m = 8n\omega_r$.
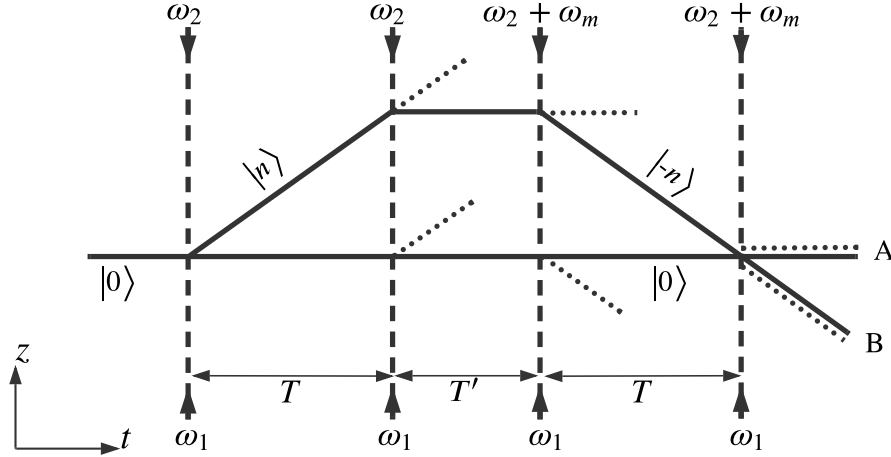
Figure 2.6: Atom trajectories in a Ramsey-Bordé atom interferometer. Dashed lines with arrows represent pairs of counter-propagating laser pulses that drive nth order Bragg diffraction. The frequency of the third and forth Bragg pulses is shifted by ω_m relative to the first and second Bragg pulses.

In the absence of systematic effects, the phase we can read out from this type of interferometer is

$$\Phi_{\mathrm{RB}} = 8n^2\omega_r T - 2nkg(T + T')T - n\omega_m T + n\omega_m T\frac{v_0}{c}, \tag{2.55}$$

where $k = (\omega_1 + \omega_2)/c$ is the averaged wave vector of the first two Bragg pulses, ω_r is the recoil frequency, and v_0 is the velocity of the atom at the moment of the first Bragg pulse [95]. This phase can be understood intuitively. Because the upper arm of the interferometer has none zero velocity relative to the lower arm, the first term $8n^2\omega_r T$ is proportional to the kinetic energy difference between the two arms. The two arms spend time at different heights, sensing different gravitational potentials, so the second term is related to g. The last two Bragg pulses have different averaged wave vectors when compared to the first two Bragg pulses, so the third and forth terms depend on ω_m.

For the forth term of Φ_{RB} in Equation 2.55, it can be interpreted as a separation phase. Because of the frequency shift ω_m, the interferometer will not be fully closed at the moment of the last Bragg pulse. There will be a vertical separation of $\delta z = n\hbar\omega_m T/(mc)$ in the end, as shown in Figure 2.7. This separation is small when compared to the coherent length of the atom. So we will still be able to observe interference. But it will introduce a separation

Figure 2.7: The Ramsey-Bordé interferometer is not fully closed due to ω_m.
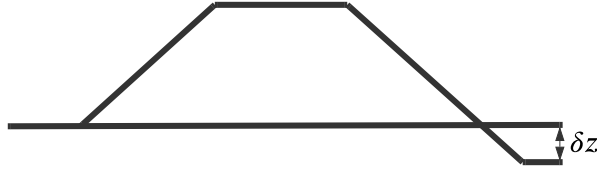
phase

$$\phi_{\text{separation}} = \frac{mv_0\delta z}{\hbar} = n\omega_m T \frac{v_0}{c}. \tag{2.56}$$

This term may seem to violate Lorentz invariance: if we choose a different reference frame, v_0 will be different, so the total phase will be different. But keep in mind that ω_m will have to be Doppler shifted if we use a different reference frame. Say the new reference frame has a velocity v' relative to our lab frame, the third term of Φ_{RB} becomes $-m\omega_m T(1 - v'/c)$ and the separation phase becomes $n\omega_m T(v_0 - v')/c$ in this new frame. The dependence on v' cancels. The total phase doesn't change.

H

Simultaneous Conjugate Ramsey-Bordé Interferometers

Since Φ_{RB} from a Ramsey-Bordé interferometer depends on the recoil frequency $\omega_r = \hbar k^2/(2m)$, Ramsey-Bordé interferometers can therefore be used to measure h/m and, from that, the fine structure constant α. However, Φ_{RB} also depends on g, which means it will be sensitive to other accelerations like vibrations. Without mechanically stabilizing the optics, we can make a simple modification to the geometry to get rid of the g-dependent term and the effects from vibrations.

For the down-propagating component of the third and forth Bragg pulses, instead of sending only one frequency $\omega_2 + \omega_m$, we can send two frequencies $\omega_2 \pm \omega_m$, as shown in Figure 2.8. The frequency pair $\{\omega_1, \omega_2 + \omega_m\}$ will drive the atom from state $|0\rangle$ to state $|-n\rangle$, and the frequency pair $\{\omega_1, \omega_2 - \omega_m\}$ will drive the atom from state $|n\rangle$ to state $|2n\rangle$. This creates two simultaneous conjugate Ramsey-Bordé interferometers. The phases that they measure are

$$\Phi_{\text{RB}\pm} = \pm 8n^2\omega_r T \mp n\omega_m T + 2nkg(T + T')T + \Phi_{\text{vibration}}, \tag{2.57}$$

where $\Phi_{\text{RB}+}$ is the phase from the upper interferometer, and $\Phi_{\text{RB}-}$ from the lower interferometer. $\Phi_{\text{vibration}}$ is the phase shift introduced by vibrations. Systematic effects as well as the separation phase have been omitted for clarity.

If we don't mechanically stabilize the optics, the random change in $\Phi_{\text{vibration}}$ will completely wash out the interference fringe from each interferometer. But as the two interferom-
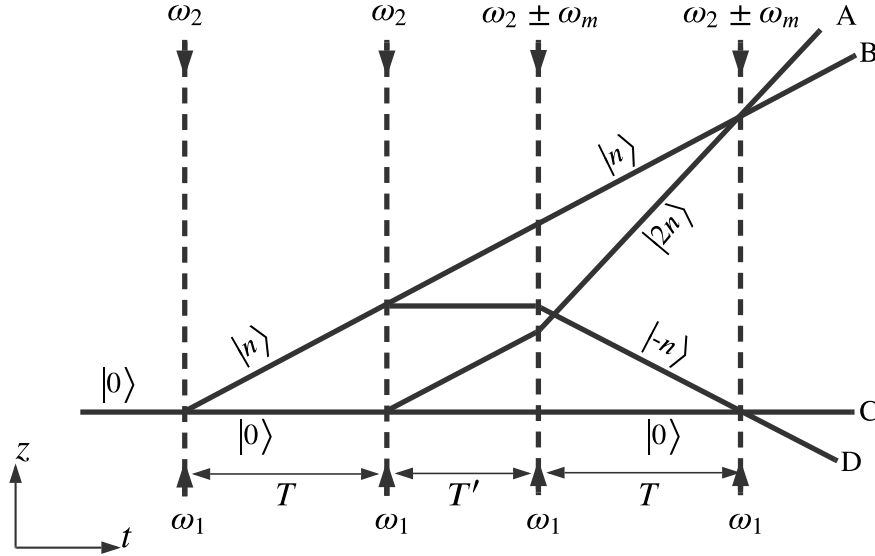
Figure 2.8: Simultaneous conjugate Ramsey-Bordé interferometers. The down-propagating component of the last two Bragg pulses contains two frequencies $\omega_2 \pm \omega_m$.

eters run simultaneously, $\Phi_{\text{vibration}}$, as well as the $2nkg(T + T')T$ term, is a common mode effect of the two interferometers. We can use techniques like ellipse fitting [31, 33] to extract the differential phase between the two interferometers. This differential phase is

$$\Phi_d = \Phi_{\text{RB}+} - \Phi_{\text{RB}-} = 16n^2\omega_r T - 2n\omega_m T. \tag{2.58}$$

Theory of ellipse fitting is introduced in Section 4.1.

With Bloch Oscillations

While the simultaneous conjugate geometry cancels the effects from vibrations, it can be improved in many aspects. In terms of sensitivity, when we use this geometry to measure the recoil frequency, the total measured phase can be viewed as $\Phi_{\text{total}} = 16n^2\omega_r T$ (see Section 4.4). In order to improve the sensitivity, we would want to increase this total measured phase. In terms of systematic effects, this geometry doesn't cancel the diffraction phase from Bragg diffraction beam splitters. The diffraction phase is caused primarily by off-resonant Bragg scattering in the third and fourth laser pulses, where multiple frequencies for the Bragg beams are used to simultaneously address both interferometers [30, 65]. It would be good if we can increase ω_m to move the off-resonant component further off resonance. Bloch oscillations have proved to be beneficial in these aspects.

Bloch oscillation describes the oscillation of a particle confined in a periodic potential when a constant force is acting on it. In atomic physics, an atom trapped in optical lattices

will undergo Bloch oscillations when the frequencies of lattice beams are ramping at a constant rate [13, 68]. Assuming the ramp rate is r, in the lab frame, the lattices have a constant acceleration rate $r/2k$. Therefore, in the rest frame of the lattices, there is a constant force

$$F = -\frac{rm}{2k}$$

acting on the atom, where m is the mass of the atom. The atom has a well defined quasi-momentum $\hbar k_q$ as determined by the band structure of the lattice, where k_q is the quasi-wavenumber taken from the first Brillouin zone $[-k, k)$ (see Equation 2.48). With the presence of the constant force F, the quasi-wavenumber evolves as

$$k_q(t) = k_q(0) + \frac{Ft}{\hbar}. \tag{2.59}$$

When $k_q(t)$ approaches k, the right edge of the first Brillouin zone, if the linear ramp is slow enough, it will wrap back into the first Brillouin zone from the left edge $-k$, and starts the linear evolution again. This can be understood as a first-order Bragg transition undergone via adiabatic passage. As the atom accelerates in one direction, the increasing Doppler shift brings its detuning closer to two-photon resonance. The atom then adiabatically passes through the transition, and receives $2\hbar k$ momentum kick [19]. Therefore, in the rest frame of the optical lattices, the quasi-momentum oscillates between $-\hbar k$ and $\hbar k$. The period of this oscillation is

$$T_B = \frac{2\hbar k}{|F|} = \frac{4\hbar k^2}{rm}. \tag{2.60}$$

Now switch back to the lab frame, the momentum of the atom will increase by $2\hbar k$ after every T_B. By holding the atom in the lattice and ramping the frequencies of the lattice beams for N periods (N Bloch oscillations), we can increase the momentum of the atom by $2N\hbar k$.

In our experiment, we apply Bloch oscillations between the second and third Bragg pulses, as shown in Figure 2.9. After the second Bragg pulse, the upper interferometer is in the momentum state $|n\rangle$ and the lower interferometer is in the momentum state $|0\rangle$. They are adiabatically loaded into two optical lattices. The two optical lattices accelerate and drive Bloch oscillations in opposite directions. After N periods, the upper interferometer is in the momentum state $|n + N\rangle$, and the lower interferometer is in the momentum state $|-N\rangle$. They are then adiabatically unloaded from the lattices by turning down the power of the lattice beams gradually.

The Bloch oscillation beams can be generated in the same way as the multi-frequency Bragg pulses: one frequency ω_1 propagates upwards and two frequencies $\omega_2 \pm \omega_b$ propagates downwards. The frequency pair $\{\omega_1, \omega_2 + \omega_b\}$ addresses the lower interferometer, and the frequency pair $\{\omega_1, \omega_2 - \omega_b\}$ addresses the upper interferometer. ω_b is swept from $4n\omega_r$ to $(4n+8N)\omega_r$ when N Bloch oscillations are used. For adiabatically loading into and unloading from the optical lattices, the Bloch oscillation beams should have trapezoid temporal profiles.

In order for the third and forth Bragg beams to stay resonant for nth order Bragg diffraction, $\omega_m = 8(n + N)\omega_r$.

The differential phase we can read out from this geometry is

$$\Phi_d = 16n(N + n)\omega_r T - 2n\omega_m T. \tag{2.61}$$

Comparing to Equation 2.58, the total measured phase is increased from $16n^2\omega_r T$ to $16n(n+N)\omega_r T$. By applying hundreds of Bloch oscillations, we can greatly improve the sensitivity of the interferometers. In the meantime, ω_m is increased from $8n\omega_r$ to $8(n + N)\omega_r$, helping suppress systematic effects like the diffraction phase.

In practice, the maximum number of Bloch oscillations that we can use is limited by various loss and decoherence mechanisms. Since a Bloch oscillation is an adiabatic process, an atom may leave the lattice during every Bloch period due to Landau-Zener tunneling [97]. Single photon scattering will also cause the loss of the atoms. As a result, applying Bloch oscillations will lower the signal size exponentially. If the Bloch beams have wave front distortions, atoms addressing by Bloch beams will experience decoherence due to varying ac-Stark shifts. We will talk about these limitations in Chapter 4.
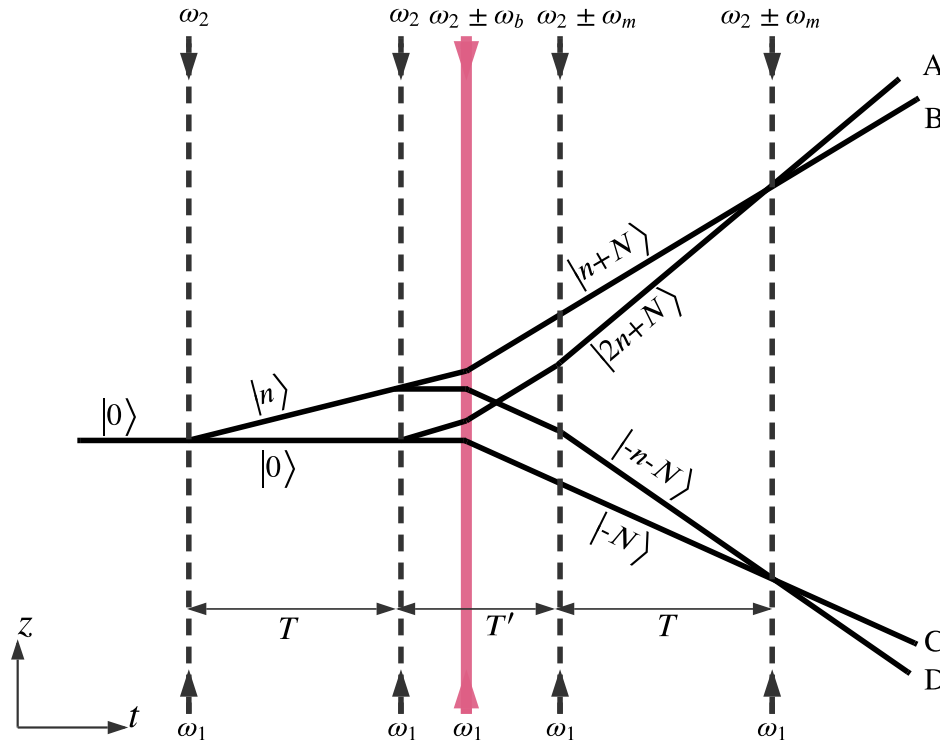

Figure 2.9: Simultaneous conjugate interferometers with Bloch oscillations. The pink band represents the Bloch oscillation sequences.

Chapter 3

Apparatus

3.1 Overview

In this chapter, we will review the apparatus and the timing sequence used in the experiment.

Having simple energy structure to manipulate, alkali atoms have been used in most atom interferometry experiments. We use cesium-133 atoms in our experiments. Specifically, we use the cesium D_2 line for trapping, cooling and interferometry. A diagram of the cesium D_2 transition hyperfine structure is shown in Figure 3.1 [79]. Cesium D_2 line includes the transitions from the $6^2S_{1/2}$ ground state to the $6^2P_{3/2}$ excited state. The $6^2S_{1/2}$ ground state has two hyperfine levels $F = 3$ and $F = 4$, separated by about $9.19\,\mathrm{GHz}$. The $6^2P_{3/2}$ excited state has four hyperfine levels $F' = 2$ to $F' = 5$, separated by several hundreds of MHz. The wavelength of D_2 transitions is around $852\,\mathrm{nm}$, which is accessible by semiconductor lasers and Ti:Sapphire lasers.

The experiments are performed in an ultra-high vacuum environment to reduce scatterings from background atoms. Increasing the free-fall time of the atoms in vacuum will allow us to increase the pulse separation time, thus improve the sensitivity. To achieve this goal, the experiments are performed with an atomic fountain, where we launch the atoms upward to double the free fall time. We also implement various trapping and cooling techniques to cool down the temperature of the atoms, so we can have a longer coherence time and better signal-to-noise ratio.

Figure 3.2 shows the design of the vacuum chamber and the optical system for generating Bragg and Bloch beams. The chamber has three parts. From bottom to top, the first part is for trapping atoms with Magneto-Optical Trap. We also launch the atoms in that chamber. This chamber is referred to as the MOT chamber later in this thesis. The second part is for Raman sideboard cooling when the atoms move upward, and for detection when the atoms fall back. It will be referred to as the detection chamber later. The third part is a 1.6m long tube. This is where interferometry happens. Inside this tube, there are three layers of μ-metal shields that isolate the atoms from environment magnetic fields. Inside the μ-metal shields is a solenoid winded around an aluminum tube, which creates magnetic fields along

$F' = 5$

251.00(2) MHz

12.815(9) MHz

$F' = 4$

$6^2P_{3/2}$

201.24(2) MHz

$F' = 3$

151.21(2) MHz

$F' = 2$

351.725 718 50(11)THz

351.730 549 61(11) THz

$F = 4$

4.021776 GHz

9.192 631 770 GHz

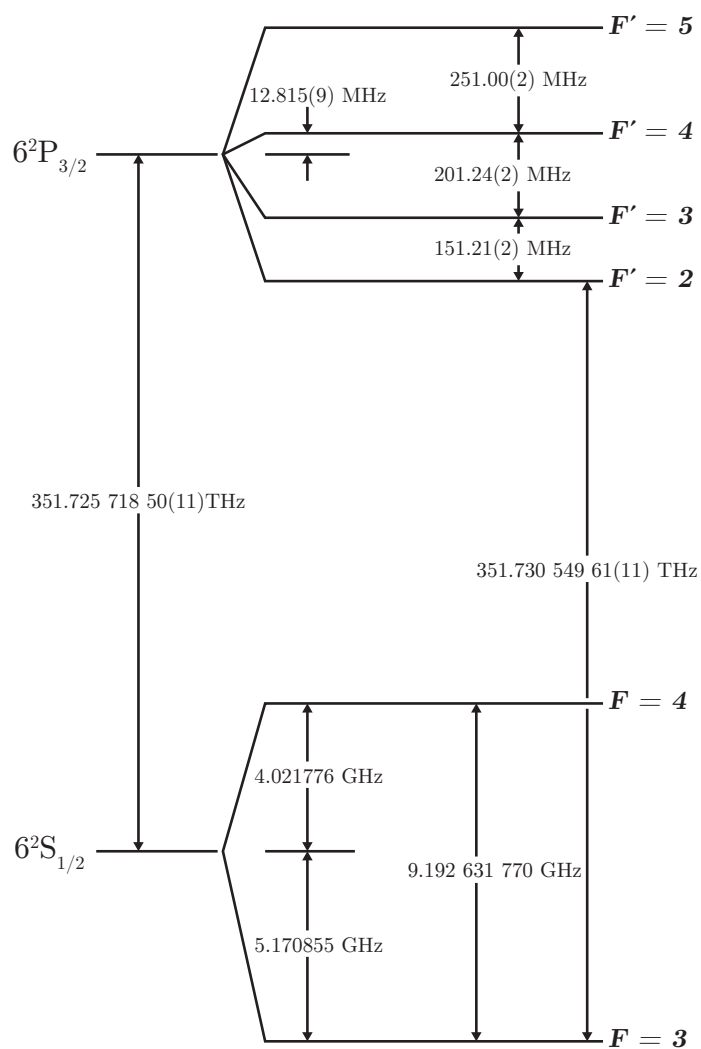$6^2S_{1/2}$

5.170855 GHz

$F = 3$

Figure 3.1: Cesium D_2 transition hyperfine structure, with frequency splittings between the hyperfine energy levels [79].

the vertical direction that will define the quantum axis for the atoms. The vacuum pressure in the chamber has been pumped down to 10^{-9} torr.

The optical system of our experiments can be divided into three subsystems: a spectroscopy, the atom cloud preparation system and the coherent manipulation system. For the spectroscopy, a reference laser (New Focus Vortex TLB-6917) is frequency stabilized to the cesium $F = 3 \to F' = 2$ D$_2$ transition using a hybrid Doppler-free frequency modulation and modulation transfer spectroscopy [100]. All other lasers used in the experiments are locked to the spectroscopy with various locking methods. The atom cloud preparation system includes the optics for trapping, launching, cooling and detecting atoms. The light sources of this part are semiconductor lasers. Acousto-optic modulators (AOMs) and electro-optic modulators (EOMs) are used to shift the frequency of the lasers for different purposes. Tapered amplifiers are used to amplify the power of the lasers when needed. The coherent manipulation system generates Bragg and Bloch beams with a Ti:Sapphire laser. AOMs are used to shape the temporal profiles, tune the frequencies, and control the timing of the laser beams. This part is shown in Figure 3.2.

The experimental timings are controlled by two programmable National Instrument cards (PCI-6534 and PCI-DIO-32HS) which creates TTL signals for atom preparation and to initiate the interferometer sequence. Once the interferometer sequence starts, the separation time between the Bragg and Bloch beams are precisely controlled by SRS DG535 and DG645 pulse generators. All frequencies of electronics, such as pulse generators and function generators, are referenced to a rubidium frequency standard which is itself stabilized to the global positioning system.

The apparatus is mainly inherited from previous generations of researchers. One can refer to their theses [95, 52, 29] for a detailed description about the apparatus. In the following sections, we will focus on the experiment sequence and the coherent manipulation system.
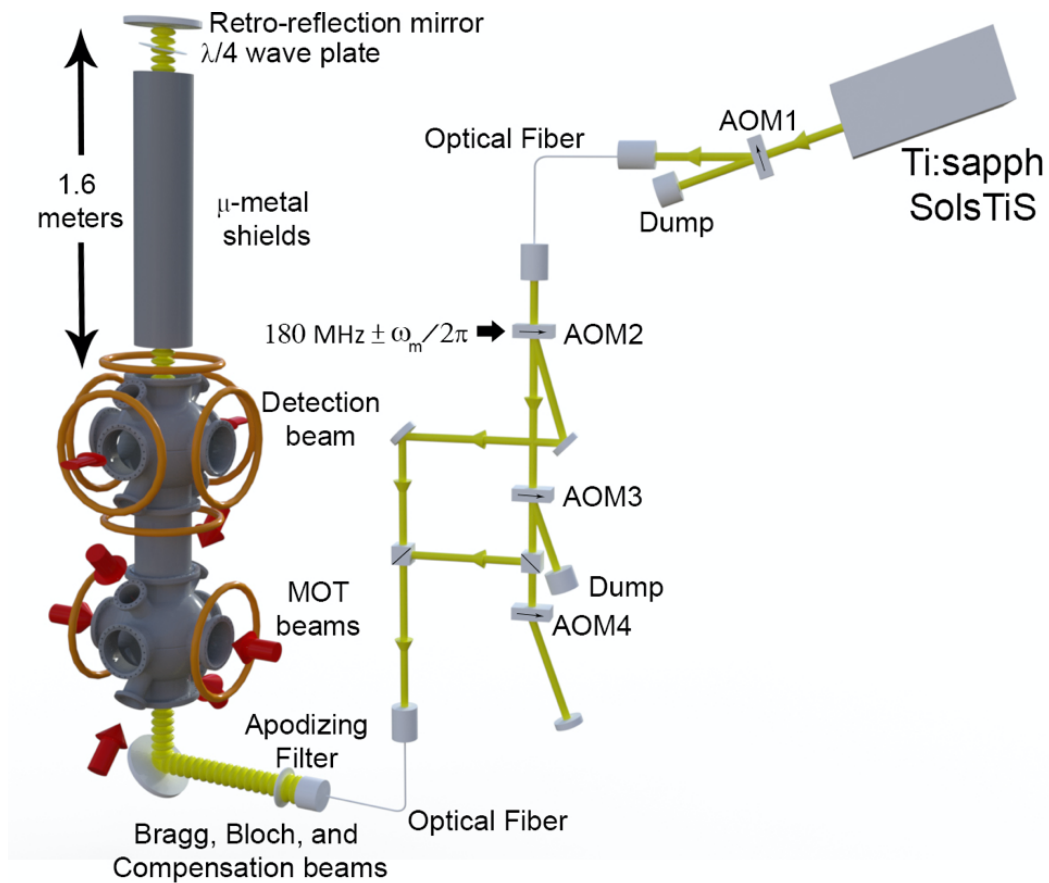
Figure 3.2: Experimental apparatus, including the vacuum chamber and the optical system for generating Bragg and Bloch beams.

3.2 Experiment sequence

Figure 3.3 shows the timing sequence used in the experiment. The whole sequence takes 2.4 seconds. It can be roughly split into three stages: atom cloud preparation (including magneto-optical trap, atomic fountain, Raman sideband cooling, rapid adiabatic passage, state selection and velocity section), interferometry and detection. We introduce them one by one.
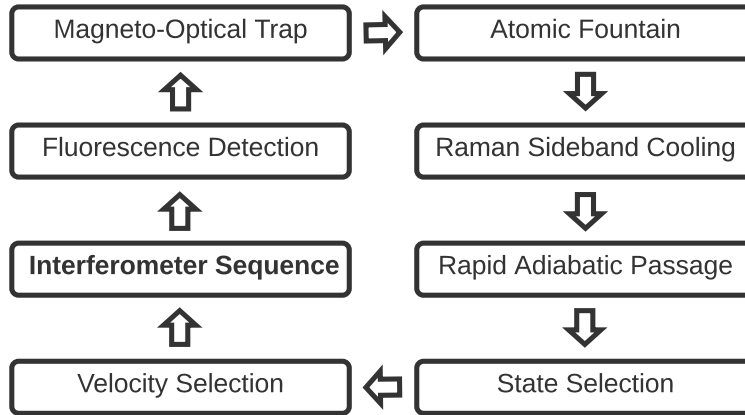
Figure 3.3: The overall experimental time sequence.

Magneto-Optical Trap

In an atom interferometer, every atom interferes with itself. The interactions between atoms are considered as systematic effects and should be suppressed. In theory, running the experiment with one atom per shot and integrating for long enough time will give us the same result. In practice, in order to accelerate the integration, we usually trap billions of atoms to an atom cloud and operate on all trapped atoms at one time. One standard technique for creating an atom cloud is Magneto-optical trapping (MOT) [72]. It captures atoms from room-temperature atom vapor using counter-propagating lasers and magnetic fields. The atom population density in the atom cloud created by MOT usually is not very high, and the captured atoms can still be considered as thermal atoms. This is ideal for atom interferometry, as the interatomic potential is negligible in the atom cloud.

In our experiment, MOT happens in the first second of the sequence. Cesium atoms are first captured from cesium vapor with a 2D MOT in a separate glass vacuum chamber (not shown in Figure 3.2). This 2D MOT contains two pairs of counter-propagating beams, which confine the motion of atoms in the transverse dimension. The resulting atom flux in the longitudinal direction will be injected into the main MOT chamber through a differential pumping tube and captured by a 3D MOT. The 3D MOT has three pairs of counter-propagating beams, with one pair along the horizontal direction (x-axis), and two

pairs forming an 'X' shape in the vertical plane (y-z plane), as shown in Figure 3.2. These three pairs of beams completely confine the motion of the atoms. The quadruple magnetic field used for the 3D MOT is generated by two big coils in an anti-Helmholtz configuration along the x-axis. By loading atoms with two separate vacuum chambers, we can have a high cesium partial pressure in the 2D MOT chamber for fast loading, while having a low vacuum pressure in the main MOT chamber to reduce background scattering during interferometry.

After loading for 1 second, the 2D MOT laser beams and magnetic fields are turned off. The large magnetic fields for 3D MOT are shut off by turning off the current in the MOT coils. But as the MOT chamber is made of steel, the Eddy current induced by the change of magnetic flux will last for many milliseconds. This Eddy current will cause secondary magnetic filed, which will affect the next step of the experiment. Therefore, the laser beams for 3D MOT are kept unchanged for another 30 ms to prevent trapped atoms from escaping while the Eddy current is decaying. After this is done, the remaining atom cloud contains about 10^9 atoms. They are in the $F = 4$ ground state.

Atomic Fountain

After Eddy current decays, we use the Moving Molasses technique to launch the atom cloud [63]. The trap frequency f_{trap} of the MOT beams are initially 15.5 MHz red detuned from the cesium $F = 4 \rightarrow F' = 5$ D$_2$ transition. We keep the frequency of the two horizontal MOT beams unchanged. The frequency of the two upper MOT beams are decreased by ϵ, and the frequency of the two lower MOT beams are increased by ϵ. Once the frequencies are shifted, photons from the lower MOT beams are more likely to be absorbed by the atoms comparing to photons from the upper MOT beams, as their frequency is closer to resonance. This gives the atoms an overall upward recoil. After the atoms gaining a velocity v, the resonant frequency of the atoms will change by $f_{\text{trap}}v/c$ due to the Doppler effect. The motion of the atoms reaches equilibrium again when the Doppler effect cancels the applied frequency shift. Therefore, we can estimate the equilibrium launch velocity of the atom cloud from

$$f_{\text{trap}}\frac{v_{\text{launch}}}{\sqrt{2}c} = \epsilon, \tag{3.1}$$

where v_{launch} is the launch velocity of the atoms. The $\sqrt{2}$ comes from the fact that the upper and lower MOT beams are 45 degrees along the vertical launch direction. In our experiment, we set ϵ to 4 MHz. The trap frequency is about 252 THz for 852 nm light. This gives us a launch velocity of about 4.8 m/s.

The atom cloud from the MOT has a theoretical Doppler temperature limit, which is 125 μK for cesium. This temperature is too high to be useful for atom interferometry experiment. At this temperature, the thermal expansion rate of the atom cloud along the vertical direction will outweigh the momentum differences between the interferometer's different output ports (which can be characterized by the recoil temperature, 200 nK for cesium). The output ports of the interferometer will not be resolved. To further cool down the temperature of the atom cloud, polarization gradient cooling (PGC) is applied right after moving molasses [89, 85]:

after loading the atoms in the moving molasses for 2 ms, the laser beam intensity is lowed by a factor of 2 and the detuning is increased. After another 1 ms, the laser beam intensity is then ramped off adiabatically to release the atoms from the moving molasses lattices. PGC reduces the temperature of the atom cloud to 2 μK, as measured by the time-of-flight technique.

Note that the atom cloud has a radius about 1 mm and the MOT beam has a waist of 1.6 cm. All the steps we have talked about so far are effected by the same laser beams and happen at about the same height. After PGC, we let the atom cloud fly into the detection chamber for further preparation.

Raman Sideband Cooling

Despite the micro kelvin temperature achieved after PGC, the atom cloud is still not cold enough for interferometry. In the vertical direction, the thermal expansion rate is still larger than the momentum differences between the interferometer's different output ports. In the transverse dimension, since the Bragg and Bloch beams have Gaussian wavefronts, the fast thermal expansion rate of the atom cloud will increase the intensity inhomogeneity across the atom cloud. This will lower the driving efficiencies of the Bragg and Bloch beams, and lower the signal-to-noise ratio. To further narrow the velocity distribution of the atoms, Raman Sideband cooling (RSC) is applied when the atoms reach the center of the detection chamber. For detailed theory about RSC, one can refer to the thesis [47]. RSC lasts for 2.8 ms. After RSC, the temperature of the atom cloud is measured to be around 300 nK by time-of-flight, which is at the same level as the recoil temperature of cesium.

Adiabatic rapid passage

RSC pumps the atoms to the magnetic sensitive state $F = 3$, $m_F = 3$. In order to suppress the systematic effects associated with magnetic fields, such as the Zeeman shift, we would want the atoms to stay in a magnetic insensitive $m_F = 0$ state. Therefore, adiabatic rapid passage (ARP) is applied right after RSC. ARP drives the atoms to the magnetic insensitive state $F = 4$, $m_F = 0$ with high power micro wave [56]. After that, the atoms fly into the interferometer chamber.

State Selection

The driving efficiency of ARP is not perfect. After ARP, there are still some atoms left in the $F = 3$ state. ARP also has some probability to drive the atoms to the magnetic sensitive sub-levels of the $F = 4$ state. To clean out all those unwanted atoms, a sequence of state selection pules are applied. A pulse that is resonant with the $F = 3 \rightarrow F' = 2$ cycling transition (henceforth referred to as the 3-state blow-away pulse) first removes the residual atoms in the $F = 3$ state after ARP. A velocity insensitive Raman transition pulse then drives the atoms from the $F = 4$, $m_F = 0$ state to the $F = 3$, $m_F = 0$ state. A pulse that is resonant with the $F = 4 \rightarrow F' = 5$ cycling transition (henceforth referred to as the 4-state

blow-away pulse) then blows away the residual atoms in all magnetic sub-levels of the $F = 4$ state. With this sequence of pulses, all atoms are now in the $F = 3$, $m_F = 0$ state.

The velocity insensitive Raman pulse, as well as the velocity sensitive Raman pulse for velocity selection that we will talk about later, is generated in a similar way as the Bragg and Bloch pulses (see Section 3.3). The differences include: the temporal profiles of the Raman pulses are shaped to be square by AOM2 (see Figure 3.2); an EOM is used in the frequency component which double-passes AOM4 to introduce a ∼9.19 GHz shift; the driving frequency of this EOM as well as AOM4 are tuned either to drive velocity insensitive or velocity sensitive Raman transitions; the intensity of all Raman pulses are tuned to be slightly lower than maximum efficiency to prevent from over-driving.

Velocity Selection

As mentioned in the RSC subsection, the temperature of the atom cloud after RSC reaches the level of several hundred nano kelvin, and the spread of atoms' velocity distribution is at the level of 1 recoil velocity v_r (for cesium, $v_r \approx 3.5$ mm/s). This is still not narrow enough for Bragg diffraction. Bragg diffraction requires the atoms to have a velocity distribution narrower than $1v_r$ along the vertical direction, so they can have similar Doppler effect, thus similar driving efficiency. Since the velocity difference between two output ports of an interferometer is on the order of v_r, a narrower vertical velocity distribution also makes it easier for the two outputs of one interferometer to be spatially resolved when they fall through the detection region. Therefore, we apply a sequence of pulses to select a vertical-velocity subgroup of atoms and discard others: a velocity sensitive Raman pulse is applied to drive the atoms within a narrow vertical-velocity range from the $F = 3$, $m_F = 0$ state to the $F = 4$, $m_F = 0$ state, a second velocity sensitive Raman pulse then drives the atoms back to the $F = 3$, $m_F = 0$ state. After each velocity sensitive Raman pulse, residual atoms are blown away with a 3-state or 4-state blow-away beam.

After this sequence of velocity-selection pulses, there are about 10^7 atoms left in the $F = 3, m_F = 0$ state. They have a vertical velocity spread about 0.1 v_r. These atoms are ready for the interference sequence.

Inteferometry

One interference sequence consists of several Bragg diffraction pulses and Bloch oscillation sequences. Different combinations of them will lead to different atom interferometer configurations. Details about the experimental realization of the Bragg and Bloch beams will be discussed in the next section. In general, we want interference to happen as soon as possible relative to start of the experimental sequence. As the atom cloud are thermal expanding during the flight, applying the interference sequence earlier means the atom cloud will be smaller when it interacts with the laser pulses. The laser intensity will be more uniform across the atom cloud. This helps to improve the contrast. Applying the interference sequence earlier also allows the output ports to have more time to separate, thus makes it

easier for detection. This becomes more critical when there are more output ports, such as the OSCIs that we will talk about in Chapter 5. Another thing we need to pay attention to is, we want to avoid applying Bragg or Bloch beams when the atom trajectory reaches the apex. At the apex, the velocity of the atoms is close to zero. The Doppler shift vanishes at the apex, so the frequency of the up-going and down-going beams degenerate (see Section 3.3).

Detection

We detect the atoms with a pair of large 100 mm diameter, f = 100 mm lenses, which collect the atom fluorescence and focus the light onto a 2 mm × 2 mm silicon photodetector. Atoms are driven on the cycling $F = 4$, $m_F = 4 \rightarrow F' = 5$, $m_{F'} = 5$ transition with circularly polarized light. The fluorescence beam and the detector are apertured so as to detect only the central part of the atomic cloud.

3.3   Coherent Manipulation

Ti:Sapphire Lasers

The Bragg and Bloch beams, as well as the state selection and velocity selection Raman pulses, are generated by a MSquared SolsTis titanium:sapphire laser, which can output up to 6 W of single-frequency 852 nm light when pumped by a Verdi V18 DPSS laser. Historically, we use a special MSquared laser with its etalons being removed, so that it can outputs enough power (see reference [52]). The frequency of this special MSquared laser is stabilized with the help of a Coherent 899 titanium:sapphire laser: the Coherent 899 laser is pumped by a Verdi V10 DPSS laser, and can output around 450 mW of 852 nm light; it is phase-locked to the reference laser with a tuneable offset of several GHz; the output of the Coherent 899 laser is then injected into the special MSquared laser to force stimulated emission at the injection frequency. We have used this special MSquared laser for the α measurement (see Chapter 4). In early 2018, after we are done with the measurement, we replaced the special MSquared laser with a newer-version one, which can be directly phase locked to the reference laser with a tuneable offset while outputting enough power of single frequency 852 nm light. The new MSquared laser has been used for the OSCI experiment (see Chapter 5), and will be used for the new α measurement in the future (see Chapter 6).

Single-frequency Bragg Beam Splitter

As discussed in Section 2.6, for a Simultaneous Conjugate Ramsey-Bordé interferometer, the first pair of Bragg beam splitters have the frequency components ω_1 and ω_2, and the second pair has frequencies ω_1 and $\omega_2 \pm \omega_m$. The first pair of Bragg beam splitters are referred to as the single-frequency Bragg beam splitters, and the second pair as the multi-frequency

Bragg beam splitters. Figure 3.2 shows how these frequencies are generated and applied to the atoms.

The frequency of our spectroscopy laser is on resonant with the $F = 3 \rightarrow F' = 4$ D_2 transition. We denote this frequency as $f_{3,4'}$. The MSquared laser is phase-locked to the spectroscopy with some offset. Its frequency is

$$f_{\text{MSquared}} = f_{3,4'} + \Delta - \delta,$$

where Δ is an offset set by a microwave generator. For the fine-structure constant measurement and the OSCI experiments, this offset is set to 14 GHz. δ is a radio frequency set by a DDS. It is around 80 MHz. To generate a single-frequency Bragg pulse, AOM1 first shapes a Gaussian pulse in a closed feedback loop (see Thesis [52]). The driving frequency of AOM1 is 80 MHz. The Gaussian pulse is truncated at 3σ and has a total width of 14.5 μs. The power of this Gaussian pulse is then split into two pulses by AOM2. AOM2 is driven at 180 MHz. The diffracted pulse from AOM2 is the ω_2 component of the single-frequency Bragg pulse. Its frequency thus can be calculated as

$$f_2 = f_{3,4'} + \Delta - \delta + f_{\text{AOM1}} + f_{\text{AOM2}} = f_{3,4'} + \Delta - \delta + 260 \text{ MHz}.$$

For the undiffracted pulse from AOM2, AOM3, which also runs at 180 MHz, is used to tune the power of this pulse by diffracting some power into a beam dump. The remaining power then double-passes AOM4, which shares the same frequency source as δ. The resulting pulse becomes the ω_1 component of the single-frequency Bragg beam splitter. Its frequency can be calculated as

$$f_1 = f_{3,4'} + \Delta + \delta + f_{\text{AOM1}} = f_{3,4'} + \Delta + \delta + 80 \text{ MHz}.$$

With these efforts, the effective frequency of the single-frequency Bragg pulse is

$$\omega_{\text{eff}} = 2\pi(f_1 - f_2) = 2\pi(2\delta - 180 \text{ MHz}), \tag{3.2}$$

and the average wave number

$$k = \frac{k_1 + k_2}{2} = \frac{\pi}{c}(f_1 + f_2) = \frac{2\pi}{c}(f_{3,4'} + \Delta + 170 \text{ MHz}). \tag{3.3}$$

The effective frequency ω_{eff} only depends on δ. By fine tuning δ, we can make the pulse resonant with different orders of Bragg diffractions. To compensate the Doppler effect introduced by gravity acceleration so that the atoms see constant laser frequencies across all Bragg and Bloch beams, we add a linear frequency ramp on top of δ during the interferometer sequence:

$$\delta = \delta_0 + \Lambda t. \tag{3.4}$$

The ramp rate $\Lambda = g/\lambda \approx 11.5$ MHz/s. When δ is ramped, the averaged wave number k doesn't change. This makes the data analysis process a lot easier, as k is directly used to compute h/m from the measured recoil frequency.

The two frequency components ω_1 and ω_2 are overlapped with orthogonal linear polar-izations using a polarized beam splitter, and then delivered to the bottom of the vacuum chamber through a single-mode optical fiber, as shown in Figure 3.2. After passing through a quarter-wave plate, these two frequency components become oppositely circular polarized. They then enter the vacuum chamber through the bottom mirror. Let's denote the two frequency components as $\omega_{1+\uparrow}$ and $\omega_{2-\uparrow}$ (+ or $-$ denotes the polarization, $\uparrow$ or $\downarrow$ denotes the direction of propagation). There is a mirror and a quarter-wave plate on the top of the chamber. The two frequency components are retro-reflected with two passes through the quarter-wave plate, reversing their polarizations. Therefore, the retro-reflected pulse has the frequency components $\omega_{1-\downarrow}$ and $\omega_{2+\downarrow}$. Bragg diffraction only happens when the two counter-propagating pulses have the same circular polarization, or parallel linear polarization [95]. In our setup, only the frequency pair $\{\omega_{1+\uparrow}, \omega_{2+\downarrow}\}$ or $\{\omega_{2-\uparrow}, \omega_{1-\downarrow}\}$ can be used to drive Bragg diffraction. When the velocity of the atoms are not zero, these two pairs will not be on resonant at the same time due to Doppler effect. We fine tune δ to make $\{\omega_{1+\uparrow}, \omega_{2+\downarrow}\}$ on resonant with the nth-order Bragg diffraction.

Multi-frequency Bragg Beam Splitter

The multi-frequency Bragg beam splitter is generated in a similar way as the the single-frequency one. But for the multi-frequency pulse, AOM2 is driven with with two frequencies 180 MHz $\pm\, \omega_m$, instead of a single frequency. The frequencies of the $\omega_2 \pm \omega_m$ component become

$$f_{2\pm} = f_{3,4'} + \Delta - \delta + f_{\mathrm{AOM1}} + f_{\mathrm{AOM2}} = f_{3,4'} + \Delta - \delta + 260\,\mathrm{MHz} \,\pm\, \omega_m.$$

ω_m is around 2 MHz when 5th-order Bragg diffraction and 125 Bloch oscillations are used. It is low enough so that the deflection efficiencies of AOM2 for the two frequencies are nearly equal. The two frequencies can also be coupled into the fiber with the same coupling efficiency. This way of generating the frequency pair $\omega_2 \pm \omega_m$ ensures that both components have the same optical paths, which results in a constant intensity balance and low differential phase noise between the two components.

Because AOM2 is driven with two frequencies, there is necessarily a beat in the detected optical power due to interference of the two frequencies. Therefore, the undeflected order from AOM2 also has a beat due to energy conversation. This will introduce unwanted sidebands on the ω_1 component of the Bragg pulse. To solve this problem, AOM3 is driven with the same frequency as AOM2 but with a phase that is shifted by 90 degrees. When the transmitted optical power from AOM2 reaches a maximum, the RF power of AOM3 is tuned so that AOM3 will deflects the excess power into the beam dump. Figure 3.4 shows the temporal profile of the ω_1 frequency component of a multi-frequency Bragg beam splitter. It is detected by placing a photo detector after AOM3. While it is very close to a Gaussian pulse, we can still observe some residual modulation at the peak of this pulse.

For all Bragg beam splitters in a Simultaneous Conjugate Ramsey-Bordé interferometer, we adjust the RF power of AOM2, AOM3 and AOM4, so that all pulses have about the
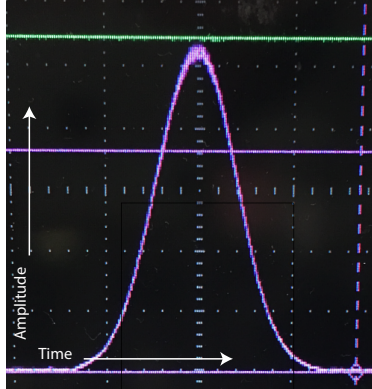
Figure 3.4: The ω_1 frequency component of a multi-frequency Bragg beam splitter. It is detected by placing a photo detector after AOM3.

same optical power in the ω_1 component, and the same optical power in the ω_2, $\omega_2 + \omega_m$ and $\omega_2 - \omega_m$ components. This ensures that the four Bragg beam splitters have roughly the same $\pi/2$ intensity.

Bloch Oscillations

The way of generating a Bloch oscillation sequence is very similar to the way of generating a multi-frequency Bragg beam splitter. For the Bloch oscillation sequence, AOM1 generates a trapezoid pulse, instead of a Gaussian pulse. The trapezoid pulse has a 100 μs rising edge for adiabatically loading the atoms into the optical lattice when Bloch oscillation begins, and a 100 μs failing edge for adiabatically unloading when Bloch oscillation ends. The duration for a single Bloch oscillation is $T_B = 66.3556$ μs. The total duration of an Nth-order Bloch oscillation sequence is NT_B, including the rising and falling edges. When 200 Bloch oscillations are used, the sequence lasts more than 13 ms. AOM2 and AOM3 run at the frequency of 180 MHz $\pm$ ω_b during a Bloch oscillation sequence, where ω_b ramps from $4n\omega_r$ to $(4n + 8N)\omega_r$ (see Section 2.6).

Chapter 4

Fine Structure Constant Measurement

4.1 Overview

Phase Formula

Figure 4.1 shows the interferometer geometry that we used for the α measurement. The theory of this geometry is introduced in Section 2.6; the experimental realization of Bragg and Bloch beams is discussed in Section 3.3. The overall differential phase between the upper and lower interferometers is given by [95]

$$\Phi_d = -2nT\omega_m + 16n(n + N)\omega_r T + \Phi_\gamma + \Phi_{\delta k} + \Phi_{\text{separation}} + \Phi_0, \tag{4.1}$$

where n is the Bragg diffraction order; N is the number of Bloch oscillations; T is the pulse separation time (see Figure 4.1); ω_m is the frequency modulation applied to the last two Bragg beam splitters; ω_r is the recoil frequency that we want to measure; Φ_0 is the diffraction phase from Bragg beam splitters. Higher order effects Φ_γ, $\Phi_{\delta k}$ and $\Phi_{\text{separation}}$ are introduced below.

The two simultaneous Ramsey-Bordé interferometers are at different heights. The local gravity they measure are slightly different. Therefore, Φ_d includes a term Φ_γ which is proportional to the acceleration gradient,

$$\Phi_\gamma = \frac{4}{3}\gamma n\omega_r T\Big[n\big(2T^2 + 3TT_2' + 3(T_1'^2 + T_2'^2)\big) \tag{4.2}$$
$$+ 2N\Big(T^2 + 3T\big(T_2' - \frac{NT_B}{2}\big) + 3T_2'(T_2' - NT_B) + \big(N^2 - \frac{1}{4}\big)T_B^2\Big)\Big].$$

Here T_B is the duration of a single Bloch oscillation; T_1' and T_2' are separation times defined in Figure 4.1; γ is the local acceleration gradient, such as the gravity gradient.
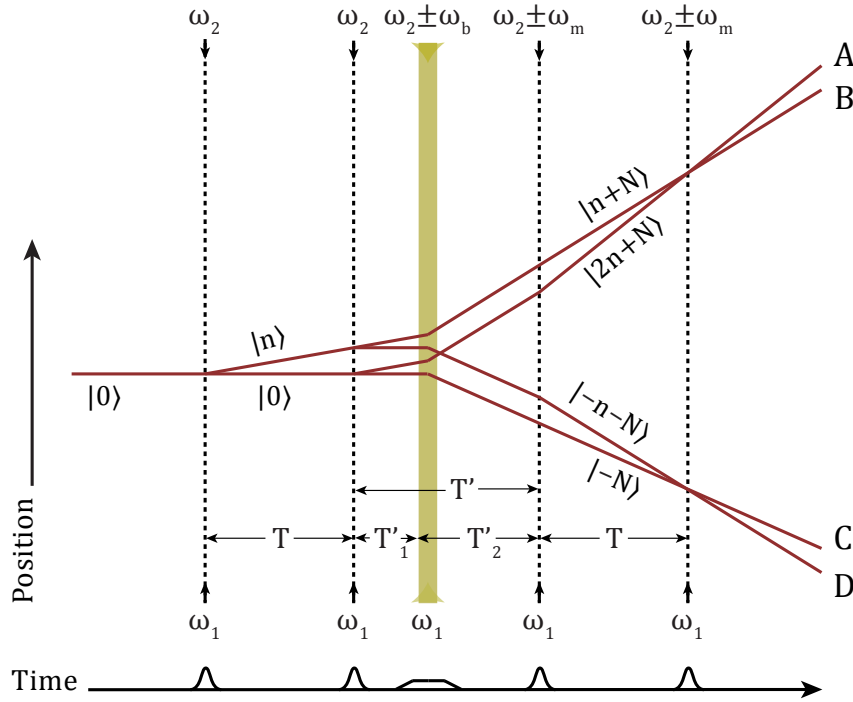
Figure 4.1: Simultaneous conjugate Ramsey-Bordé atom interferometers with Bloch oscillations. Solid lines denote the atoms' trajectories; dashed lines represent laser pulses driving Bragg diffractions; yellow band represents laser beams for Bloch oscillations. $|n\rangle$ denotes a momentum eigenstate with momentum $2n\hbar k$. Gravity is neglected in this figure. A to D are the four output ports. Bragg pulses have Gaussian temporal profiles. Bloch oscillation beams have trapezoid temporal profiles.

For the third and fourth beam splitters, the effective wave-vectors addressing the upper and lower interferometers differ by ω_m/c. This difference results in a phase shift

$$\Phi_{\delta k} = \frac{gnT(3T + 2T_1' + 2T_2')\omega_m}{c} - 4n^2\omega_r T\frac{\omega_m}{\omega_L}, \tag{4.3}$$

where $\omega_L = (\omega_1 + \omega_2)/2$ is the average laser frequency.

As mentioned in Section 2.6, the two interferometers are not fully closed at the moment of the last Bragg beam splitter. Therefore, there is a separation phase shift $\Phi_{\text{separation}}$ that depends on the initial velocity of the atom

$$\Phi_{\text{separation}} = -\frac{2nT\omega_m v_0}{c}. \tag{4.4}$$

Finally, due to the multi-port nature of Bragg diffraction, Φ_d includes the diffraction phase Φ_0 from Bragg beam splitters. Here Φ_0 will be treated as a constant. Higher order variations on the diffraction phase will be treated as systematic effects, and considered separately.

The acceleration gradient γ in Equation 4.1 has been measured in situ from an independent experiment (see Section 4.5). For a specific setting of k (or ω_L), n, N, T, T_1', T_2' T_B, and ω_m, once Φ_d is measured, the only unknowns in Equation 4.1 are ω_r and Φ_0. To determine ω_r, we can scan the pulse separation time T. At every T, we measure Φ_d, and calculate the theoretical value of ω_m that would lead to zero Φ_d. This theoretical ω_m is then fitted as a function of T. ω_r and Φ_0 will be determined as the fitting parameters.

Ellipse Fitting
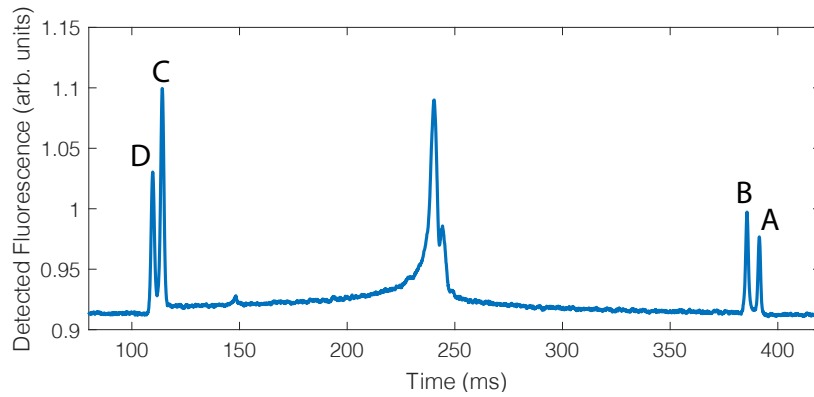
Figure 4.2: Fluorescence observed at $n = 5$, $N = 125$, $T = 5$ ms. The four outer peaks correspond to the four output ports A to D of the interferometers (see Figure 2.8) . Atoms left behind by Bloch oscillations form the central peaks; they do not contribute to the measurement.

We use a technique called ellipse fitting to extract the differential phase between the two simultaneous conjugate interferometers [33, 31].

After interference, the wave functions of the four output ports will fall through the detection beam one by one. The fluorescence signal is then recorded. Figure 4.2 shows the typical signal we observe when 5th-order Bragg beam splitters and 125 Bloch oscillations are applied. Peak A and B are from the upper interferometer, and peak C and D are from the lower interferometer (see Figure 2.8). Atoms left behind by Bloch oscillations form the central peaks; they do not contribute to the measurement. As mentioned in Section 2.1, the normalized signal from the two output ports of an interferometer is a sinusoidal function of the phase that the interferometer measures. In our scenario, the signals that we can get from the two interferometers are

$$x = \frac{C - D}{C + D} = C_x \cdot \cos(\Phi_c + \frac{\Phi_d}{2}) + O_x, \tag{4.5}$$

$$y = \frac{A - B}{A + B} = C_y \cdot \cos(\Phi_c - \frac{\Phi_d}{2}) + O_y. \tag{4.6}$$

Here x and y are the signals, C_x and C_y are the contrasts, O_x and O_y are the offsets. Φ_c is the common-mode phase of the two interferometers. Φ_d is the differential phase between the two interferometers, given by Equation 4.1.

If Φ_c is constant, then only one interferometer is needed to measure Φ_d: one can scan Φ_d by adding a modulation $\delta\omega_m$ to ω_m; this will trace out an oscillating fringe; by fitting the fringe to a cosine function, one can determine Φ_d at $\delta\omega_m = 0$. In reality, as discussed in Section 2.6, Φ_c is sensitive to vibration. Without stabilizing the top retro-reflection mirror, Φ_c fluctuates more than π radians per shot, washing out the fringe. Therefore, we use ellipse fitting to read out Φ_d instead: we plot the signal from the upper interferometer against the signal from the lower interferometer; vibration will trace out an ellipse; from the shape of the ellipse, we can determine Φ_d.

Figure 4.3 demonstrates the ellipse fitting technique. The normalized signal from the lower (x) or upper (y) interferometer varies shot by shot due to vibration. It has no apparent interference pattern. But due to the correlation between the two signals, plotting x against y will trace out an ellipse. To understand that, we just need to cancel the common mode phase Φ_c in Equation 4.6. x and y are related as

$$
\frac{1}{C_x^2}x^2 - \frac{2\cos\Phi_d}{C_xC_y}xy + \frac{1}{C_y^2}y^2 + \left(\frac{2O_y\cos\Phi_d}{C_xC_y} - \frac{2O_x}{C_x^2}\right)x + \left(\frac{2O_x\cos\Phi_d}{C_xC_y} - \frac{2O_y}{C_y^2}\right)y \tag{4.7}
$$
$$
+ \left(\frac{O_x^2}{C_x^2} + \frac{O_y^2}{C_y^2} - \frac{2O_xO_y\cos\Phi_d}{C_xC_y} - \sin^2\Phi_d\right) = 0.
$$

Equation 4.7 has the form of an ellipse function:

$$
a_1x^2 + a_2xy + a_3y^2 + a_4x + a_5y + a_6 = 0. \tag{4.8}
$$

With enough data points, we can fit these coefficients a_1 - a_6. Φ_d then can be calculated as

$$
\Phi_d = \cos^{-1}\left(\frac{-a_2}{2\sqrt{a_1a_2}}\right) \tag{4.9}
$$

We can also compute the contrasts:

$$
C_x^2 = \frac{4a_3(a_6(a_2^2 - 4a_1a_3) + a_3a_4^2 + a_1a_5^2 - a_2a_4a_5)}{(a_3^2 - 4a_1a_3)^2} \tag{4.10}
$$
$$
C_y^2 = \frac{4a_1(a_6(a_2^2 - 4a_1a_3) + a_3a_4^2 + a_1a_5^2 - a_2a_4a_5)}{(a_3^2 - 4a_1a_3)^2} \tag{4.11}
$$

To fit these coefficients, one may think we just need to minimize the residual sum of squares $||\mathbf{Da}||^2$, where $\mathbf{a} = [a_1, a_2, a_3, a_4, a_5, a_6]^T$ is the vector of coefficients that we want to optimize; $\mathbf{D} = [\mathbf{x}_1, \mathbf{x}_2, \cdots, \mathbf{x}_n]^T$ is a matrix consisting of measured data $\mathbf{x}_i =$
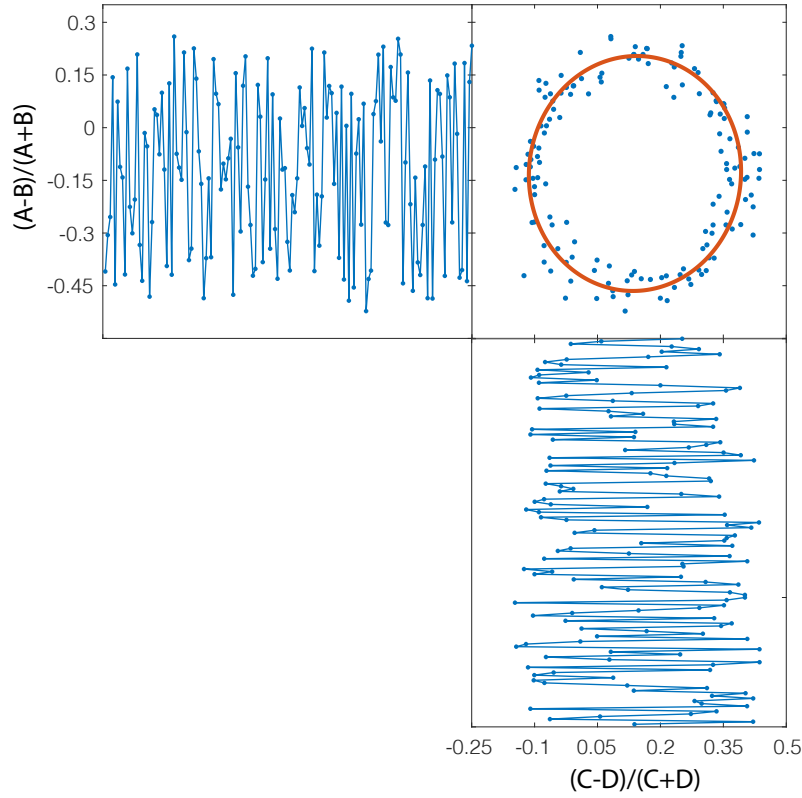
Figure 4.3: Ellipse fitting. x is the normalized signal from the lower interferometer; y is the normalized signal from the upper interferometer. Due to vibration, these signals have no apparent interference patterns. However, plotting x against y will trace out an ellipse. From the shape of the ellipse the differential phase can be determined.

$[x_i^2, x_i y_i, y_i^2, x_i, y_i, 1]^T$. But this will lead to a trivial solution $\mathbf{a} = \mathbf{0}$. To avoid this problem, we impose a constraint $4a_1 a_3 - a_2^2 = 1$, or in the matrix form $\mathbf{a}^T \mathbf{C} \mathbf{a} = 1$, where

$$\mathbf{C} = \begin{bmatrix} 0 & 0 & 2 & 0 & 0 & 0 \\ 0 & -1 & 0 & 0 & 0 & 0 \\ 2 & 0 & 0 & 0 & 0 & 0 \\ 0 & 0 & 0 & 0 & 0 & 0 \\ 0 & 0 & 0 & 0 & 0 & 0 \\ 0 & 0 & 0 & 0 & 0 & 0 \end{bmatrix}.$$

In summary, the coefficients of the ellipse can be fitted by solving a constrained optimization problem:

$$\min_{\mathbf{a}} \quad ||\mathbf{D}\mathbf{a}||^2 \tag{4.12}$$
$$\text{s.t.} \quad \mathbf{a}^T \mathbf{C} \mathbf{a} = 1$$

Note that $||\mathbf{Da}||^2 = \mathbf{a}^T\mathbf{D}^T\mathbf{Da}$. Using a Lagrange multiplier λ, the above equation can be simplified as

$$\mathbf{D}^T\mathbf{Da} - \lambda\mathbf{Ca} = 0. \tag{4.13}$$

λ and $\mathbf{a}$ are the eigenvalue and eigenvector of the equation and can be solved easily. There are usually multiple eigen-solutions to this equation. It has been proved that the eigenvector with the negative eigenvalue is the best fit for $\mathbf{a}$ [31].

Phase Measurement

As mentioned in Section 2.6, the resonant condition for the third and forth Bragg beam splitters is $\omega_m = 8(n + N)\omega_r$. We don't know ω_r accurately before the measurement (that is why we need to run the experiment!). However, we can approximate ω_r with the value of the Planck constant $\hbar$, the cesium mass in the atomic mass unit m_{Cs}/u, and the value of the atomic mass unit u. ω_m then can be calculated as:

$$\omega_m = 8(n + N)\tilde{\omega}_r = 8(n + N)\frac{\hbar k^2}{2(m_{Cs}/u)u}. \tag{4.14}$$

The tilde symbol above ω_r is to denote that it is a calculated value. Due to historical reasons, we used the CODATA 1998 recommended values [58], where $\hbar$ has an uncertainty of 78 ppb, and u has an uncertainty of 79 ppb (the uncertainty of m_{Cs}/u is negligible compared to these values). The value of k used in the above equation is also a theoretical value defined by our spectroscopy. It is slightly different from the true value (see Section 4.5). In short, $\tilde{\omega}_r$ calculated in this way has a large uncertainty. But it is close enough to calculate a value for ω_m that will make the interferometers work.

One problem with the ω_m calculated in the above way is that Φ_d will be close to zero, since the term $-2nT\omega_m$ almost cancels the term $16n(n + N)\omega_r$ in Equation 4.1. The signals x and y that we can get from the two simultaneous interferometers will be roughly co-linear (see Equation 4.6). If we plot x against y, we will get a diagonal line, instead of a circle. Simulations have shown that when Φ_d deviates from $\pi/2$, the fitting error from ellipse fitting will increase. In the extreme case when Φ_d is close to 0, the ellipse fitting algorithm would fail to get an accurate phase [52]. To solve this problem, we add additional modulations $\pm\delta\omega_m$ to ω_m, where

$$\delta\omega_m = \frac{\pi}{4nT}. \tag{4.15}$$

Replacing ω_m with $\omega_m \pm \delta\omega_m$ in Equation 4.1, the differential phase we can measure becomes

$$\Phi_{d\pm} = 2nT\delta\omega_m \mp \left[\frac{gnT(3T + 2T_1' + 2T_2')}{c} - \frac{4n^2\omega_r T}{\omega_L}\right]\delta\omega_m \mp \Phi_d \tag{4.16}$$

$$= \frac{\pi}{2} \mp \left[\frac{gnT(3T + 2T_1' + 2T_2')}{c} - \frac{4n^2\omega_r T}{\omega_L}\right]\delta\omega_m \mp \Phi_d.$$

The second term in the above equation comes from the change in $\Phi_{\delta k}$. Note the phase we measure with the ellipse fitting technique is always positive. As the second and third terms in $\Phi_{d\pm}$ are small, $\Phi_{d\pm}$ will be close to $\pi/2$. Figure 4.3 shows an ellipse with the $+\delta\omega_m$ modulation at $T = 5$ ms, $n = 5$ and $N = 125$. The ellipse with the $-\delta\omega_m$ modulation looks very similar. Having Φ_{d+} and Φ_{d-}, Φ_d can be calculated as

$$\Phi_d = \frac{\Phi_{d-} - \Phi_{d+}}{2}. \tag{4.17}$$

4.2 Data Collection

In the experiment, we use 5th-order Bragg diffractions as beam splitters ($n = 5$), and usually apply 125 - 200 Bloch oscillations ($N = 125 - 200$). Our laser beam is roughly 14 GHz blue detuned from the cesium $F = 3 \to F' = 4$ D$_2$ line. We fix the timing of the second and third Bragg beam splitters as well as the start of Bloch oscillations in the experiment sequence: the second Bragg pulse happens at 1.32 s in the sequence; $T_1' = 5$ ms, $T_2' = 15.3727$ ms. The duration of a single Bloch oscillation T_B is also fixed: $T_B = 66.3556$ μs. T usually varies from 5 ms to 80 ms, as long as we have enough contrast for ellipse fitting.

Before taking data, the frequency and power of the laser beams need to be optimized. As mentioned in Section 3.3, in the experiment, the center frequency of the two counter-propagating beams $\omega_L = (\omega_1 + \omega_2)/2$ (see Figure 4.1) is fixed. We have the degree of freedom to tune the difference between these two frequencies $\delta\omega = \omega_2 - \omega_1$. $\delta\omega$ mainly affects the diffraction phase. $\delta\omega$ is thus optimized to minimize the total measured differential phase Φ_d at $T = 40$ ms (the center of the range of T values). The power of the Bragg beam is usually optimized by maximizing the contrast of the ellipse at $T = 40$ ms. The power of the Bloch oscillation beam is tuned to the point where the efficiency is maximized.

Once the frequency and power of the laser beams is fine tuned, we start taking data. The data taking procedure works as follows: We choose several different T values in the range from 5 ms to 80 ms. At every T, we alternate between the setting of $\omega_m + \delta\omega_m$ and $\omega_m - \delta\omega_m$ for 30 times. This gives us two ellipses, each of which contains 30 data points. Φ_d at that T then can be obtained with the ellipse fitting technique and using the Equation 4.17. Measuring the Φ_d for all chosen T values yields one "run" of the experiment. This process was repeated until the system was interrupted due to, e.g. the spectroscopy was unlocked. This yields one "measurement" of h/m_{Cs} (equivalently, α). One measurement usually lasts roughly for one day. The final result is an weighted average of several measurements. Details about how h/m_{Cs} is computed will be discussed in the next section.

Figure 4.4 shows the measurements we performed to determine α. There are 28 measurements in total, collected from December 2016 to July 2017. In each measurement, only one Bloch oscillation order N was used. In order to control the systematic effects depending on N and T, different choices of N's and T's have been used for different measurements. This information is summarized in Table 4.1. The final result is obtained by weighted averaging all these measurements. The overall statistical uncertainty is 0.16 ppb. The reduced χ^2 for

the combined data is 1.2, with a p-value of 0.2, indicating that the data follows a normal distribution.

While the signal-to-noise ratio of our experiment would allow us to reach a 0.2-ppb precision in less than one day, our data were collected over the course of seven months. During the measurement campaigns, we have taken extensive data to suppress and control systematic effects. We have also realigned the system several times for best performance. For example, we would adjust the polarization and power balance of the MOT beams to make sure the atom cloud is launched straight up; we would fine tune the position and pointing of the bottom fiber port to make sure the atom cloud is always at the center of the laser beams; we would also adjust the top retro-reflection mirror so that the reflected laser beams can be back-coupled to the bottom fiber port. All these efforts have allowed the system to maintain its best sensitivity.
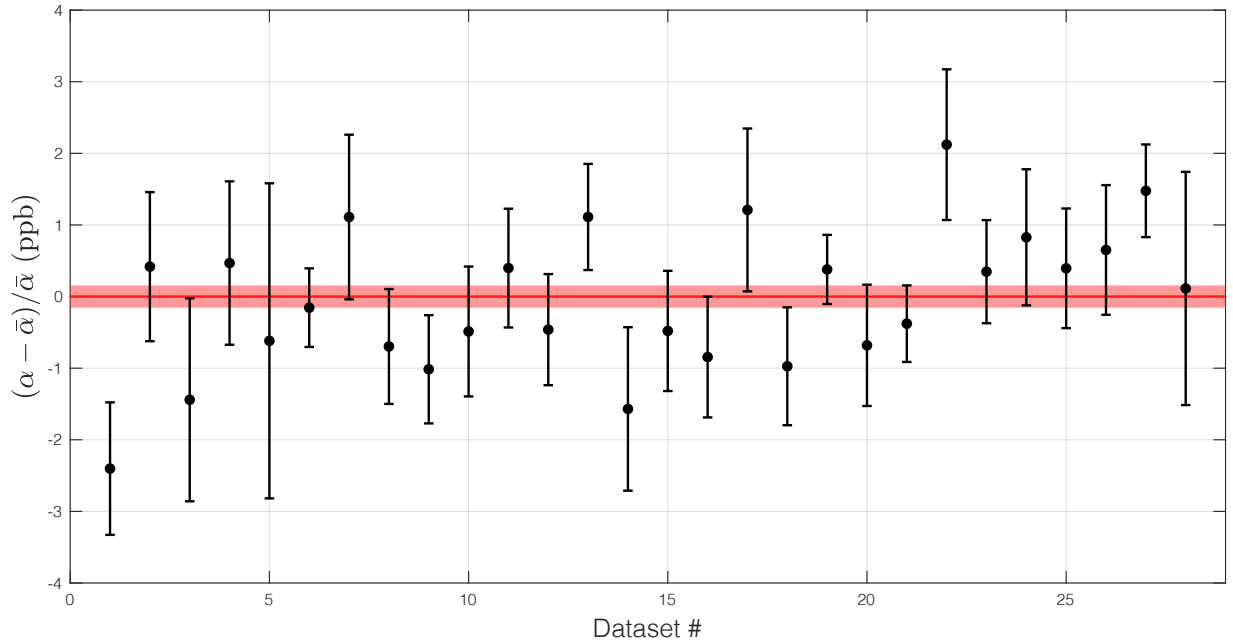
Figure 4.4: Data sets used in the determination of α. The pink band represents the overall $\pm 1\sigma$ statistical error. The reduced χ^2 for the combined data is 1.2, with a p-value of 0.2. $\bar{\alpha}$ is the weighted average of the measurements. Error bars indicate 1σ uncertainty.

4.3 Data Analysis

To extract the value of h/m_{Cs} from one measurement of data, we process the data twice. In the first pass, we filter out the outliers. In the second pass, we calculate h/m_{Cs} as well as its uncertainty.

Index	Date	N	T (ms)	# of runs
1	161213	125	10, 40, 70	46
2	161214	150	5, 10, 20, 40, 60	28
3	161215	200	5, 10, 20, 30	67
4	161221	200	5, 10, 20, 30	79
5	161222	200	5, 10, 20, 30	18
6	170102	125	5, 10, 20, 40, 60, 75	89
7	170103-0	125	5, 10, 20, 40, 60, 75	18
8	170103-1	125	5, 10, 20, 40, 60, 75	50
9	170104	125	5, 10, 20, 40, 60, 75	45
10	170105	125	5, 10, 20, 40, 60, 75	45
11	170109	125	5, 10, 20, 40, 60, 75	35
12	170110	125	5, 10, 20, 40, 60, 75	41
13	170311	125	5, 10, 20, 40, 60, 70	29
14	170313	125	5, 10, 20, 40, 60, 70	11
15	170327	125	10, 40, 60	144
16	170328	125	10, 40, 60	56
17	170329	125	10, 40, 60	53
18	170330	125	10, 40, 60	49
19	170404	125	5, 10, 20, 40, 60, 70	89
20	170405	125	5, 10, 20, 40, 60, 70	13
21	170406	125	5, 10, 20, 40, 60, 80	19
22	170602	125	5, 10, 20, 40	64
23	170603	125	5, 10, 20, 40	115
24	170607	125	5, 10, 20, 40, 60, 70	33
25	170609	125	5, 10, 20, 40	135
26	170610	125	5, 10, 20, 40	33
27	170611	125	5, 10, 20, 40, 60, 80	68
28	170612	125	5, 10, 20, 40, 60, 80	7

Table 4.1: Settings of each α measurement.

First Pass

After neglecting the higher order effects Φ_γ, $\Phi_{\delta k}$ and $\Phi_{\text{separation}}$, we can rewrite Equation 4.1 as

$$\omega'_m = \frac{\Phi_0}{2nT} + 4(n+N)k^2\frac{\hbar}{m_{\text{Cs}}}, \tag{4.18}$$

where $\omega'_m = \omega_m + \Phi_d/(2nT)$ can be viewed as a theoretical value that would lead zero measured phase. We see that ω'_m has a linear relationship with $1/T$. The slope of this linear relationship is $\Phi_0/(2n)$, and the intercept $4(n+N)k^2\hbar/m_{\text{Cs}}$. As mentioned in last section, each run of experiment includes several different T's. By linearly regress ω'_m on $1/T$, we can get $(\hbar/m_{\text{Cs}})_i$ and $(\Phi_0)_i$ for each run (i denote the ith run in one measurement). We then compute the standard deviation σ of the values of $\hbar/m_{\text{Cs}}$ from all runs. Runs with results which are 3σ away from the mean are viewed as outliers and will be filtered out.

Second Pass

Now including the higher order effects, Equation 4.1 can be rewritten as

$$\omega'_m = \frac{\Phi_0}{2nT} + \lambda\frac{\hbar}{m_{\text{Cs}}}, \tag{4.19}$$

where

$$\omega'_m = \left[1 - \frac{g(3T+2T'_1+2T'_2)}{2c} + \frac{v_0}{c}\right]\omega_m + \frac{\Phi_d}{2nT}, \tag{4.20}$$

and

$$\lambda = 4(n+N)k^2 + \frac{k^2}{3}\gamma\Big[n\big(2T^2 + 3TT'_2 + 3(T'^2_1 + T'^2_2)\big) \tag{4.21}$$
$$+2N\Big(T^2 + 3T\big(T'_2 - \frac{NT_B}{2}\big) + 3T'_2(T'_2 - NT_B) + \big(N^2 - \frac{1}{4}\big)T^2_B\Big)\Big] - nk^2\frac{\omega_m}{\omega_L}.$$

$\hbar/m_{\text{Cs}}$ and Φ_0 can be fitted from our data using this equation. In the fitting, we assume each run of experiment has a different diffraction phase Φ_0 (as the various experimental parameters may drift slowly over time), but the value of $\hbar/m_{Cs}$ is the same through out the whole measurement. Two different algorithms have been used to solve the problem. One is a Levenberg-Marquardt algorithm [66]. The other is weighted linear regression. The results from these two methods agree with other.

For the weighted linear regression method, we minimize the weighted residual sum of squares

$$\sum_{i=1}^{K}\sum_{j=1}^{L}\left(\frac{(\Phi_0)_i}{2nT_j} + \lambda_{i,j}\frac{\hbar}{m_{\text{Cs}}} - (\omega'_m)_{i,j}\right)^2/\sigma^2_j. \tag{4.22}$$

The subscript i denotes the ith run in the measurement, and the subscript j denotes any quantities related to the jth T in one run. There are K runs in total, each of which contains

L different T's. The weight σ_j is the standard deviation of $(\omega'_m)_{i,j}$ from all runs at T_j. σ_j can be interpreted as the uncertainty of the measured ω_m at T_j. In the matrix form, the problem can be stated as

$$\min_u \ ||Cu - \Omega||^2, \tag{4.23}$$

where u is a $(K+1)$ vector: the first element $u_1 = \hbar/m_{\text{Cs}}$, other elements $u_{i+1} = (\Phi_0)_i$; Ω is a $K \cdot L$ vector: $\Omega_{(i-1)\cdot L+j} = (\omega'_m)_{i,j}/\sigma_j$. C is a $(K \cdot L) \times (K+1)$ matrix: the first column $C_{(i-1)\cdot L+j,1} = \lambda_{i,j}/\sigma_j$; other columns contain zeros except for $C_{(i-1)\cdot L+j,j+1} = 1/(2nT_j\sigma_j)$. The best estimation of u can be solved as

$$\tilde{u} = (C^T C)^{-1} C^T \Omega, \tag{4.24}$$

with the fitted $\hbar/m_{\text{Cs}}$ being the first element of $\tilde{u}$. The uncertainty of $\tilde{u}$ is

$$\beta_u = \sqrt{\frac{||C\tilde{u} - \Omega||^2}{K \cdot L - 2}} diag((C^T C)^{-1}). \tag{4.25}$$

The uncertainty of the fitted $\hbar/m_{\text{Cs}}$ is the first element of β_u.

Once we have computed the values and uncertainties of $\hbar/m_{\text{Cs}}$ from all measurements, the final result is an average of all measurement results weighted by their variance

$$\frac{\hbar}{m_{\text{Cs}}} = \sum_l \frac{(\hbar/m_{\text{Cs}})_l}{\sigma_l^2} \Big/ \sum_l \frac{1}{\sigma_l^2}. \tag{4.26}$$

The final statistical uncertainty is

$$\sigma_{stat}^2 = 1 \Big/ \sum_l \frac{1}{\sigma_l^2}. \tag{4.27}$$

Here the subscript l denotes the lth measurement.

In Equation 4.20, the wave vector k should be a corrected value. The correction comes from the frequency comb measurement, alignment correction, and wavefront correction including the Gouy phase and the small scale wavefront distortions. We will talk about them in detail in the systematic effect section.

We performed the data-taking and analysis blind, so that our result would not be influenced by the knowledge of how ours compared to those of previous measurements. To achieve this, the frequency (equivalently, k) calibration of the reference laser versus spectroscopy laser power was given to Prof. Rana Adhikari, who added a random offset in the range -1 MHz to +1 MHz, and obfuscated this blinded calibration in a Matlab p-code that prevented us from deciphering the random offset. This allowed us to work without knowledge of the exact laser frequency (i.e. 'blind') to within a +/- 3 ppb window. After all the data was taken and analyzed, Prof. Adhikari provided the random offset to 'unblind' the result, which was then submitted for publication with no further modifications, other than the correction of a typo in the phase calculation and the addition of an analysis of the effect of small-scale intensity variations on the Bragg beam (see Section 3).

4.4 Statistical Sensitivity

The overall uncertainty σ_{total} of α is a combination of the statistical uncertainty σ_{stat} and the systematic uncertainty σ_{sys}:

$$\sigma_{\text{total}} = \sqrt{\sigma_{\text{sys}}^2 + \sigma_{\text{stat}}^2}. \tag{4.28}$$

σ_{sys} will be discussed in the next section. The way we calculate σ_{stat} is discussed in last section. σ_{stat} roughly scales with

$$\sigma_{\text{stat}} \sim \frac{1}{C\Phi_{\text{total}}\sqrt{\mathcal{N}T_{\text{int}}}}, \tag{4.29}$$

where C is the contrast of the signal, Φ_{total} is the total measured phase, $\mathcal{N}$ is the atom population in one shot and T_{int} is the integration time. We see that σ_{stat} scales with $1/\sqrt{T_{\text{int}}}$. In order to reduce the statistical uncertainty by a factor of 10, the data-taking time will have to be 100 times longer. To integrate σ_{stat} down faster (equivalently, improve the sensitivity of the experiment), we need to increase the total phase Φ_{total} or the contrast C.

For our experiment, Φ_{total} can be calculated from Equation 4.19 as

$$\Phi_{\text{total}} = 2n\omega_m'T \approx 16n(n+N)\omega_r T. \tag{4.30}$$

It scales quadratically with the Bragg order n when $N = 0$. By using 5th-order Bragg diffraction as beam splitters, we increase Φ_{total} by a factor of 25 compared to the standard two-photon Raman transition. At the current detuning level, this number is limited by the output power of the laser.

Φ_{total} can also be increased by using a longer pulse separation time T. The maximum T we can achieve is usually limited by the contrast of the ellipse. Figure 4.5 shows the typical ellipses we observe at various T's when 125 Bloch oscillations are applied. We can see that as T increases, the contrast of the ellipse decreases. When T goes from 5 ms to 80 ms, the y (signal from the upper interferometer) contrast decays from 33% to 21%, and the x (signal from the lower interferometer) contrast decays from 26% to 17%. This decay in contrast can be explained from two aspects. Firstly, our laser beams have roughly Gaussian wave fronts. The intensity is lower at the position that is further away from the center of the beam. Due to the thermal expansion of the atom cloud during the flight, the laser intensity that the atoms experience will change. Therefore, the driving efficiencies of the four Bragg pulses are not uniform. Using a longer T will increase this nonuniformity, as the atom cloud expands more between the four Bragg pulses. Secondly, as T is increased, distortions in the wave fronts of the Bragg and Bloch beams (which originate from the same fiber port) will result in spatially varying ac Stark shifts that lead to decoherence. The distortions can be caused by diffraction from obstructions such as dust on optics or viewports, the circular aperture of the fiber port, and the inner wall of the vacuum system. The ellipses we are showing here are taken with the ac Stark compensation beam (see below). Without the compensation beam, this decay in contrast will be even more severe.
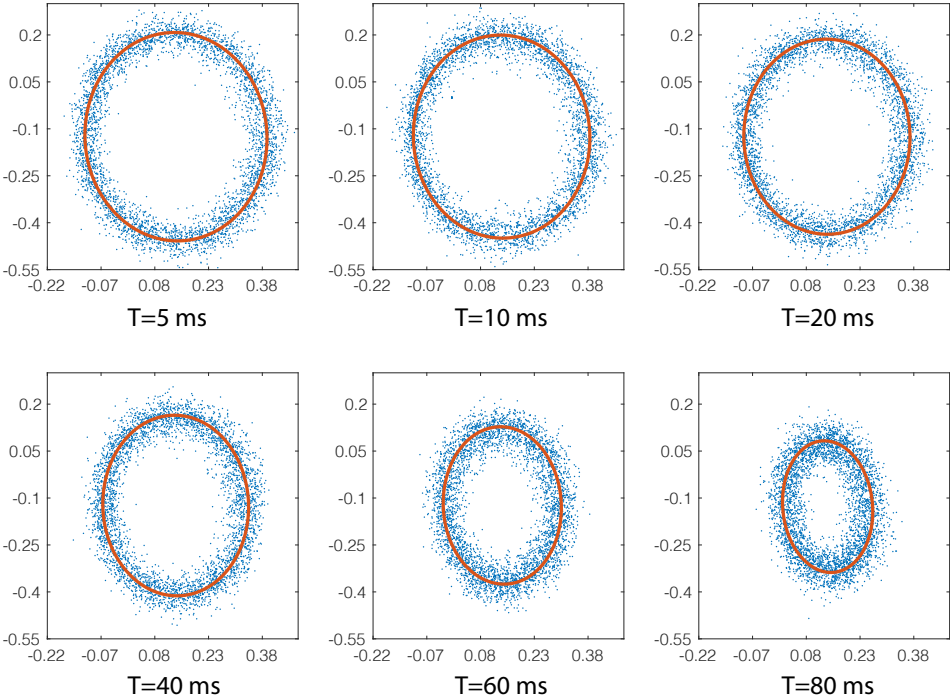
Figure 4.5: Interference ellipses at different T's when $N = 125$.
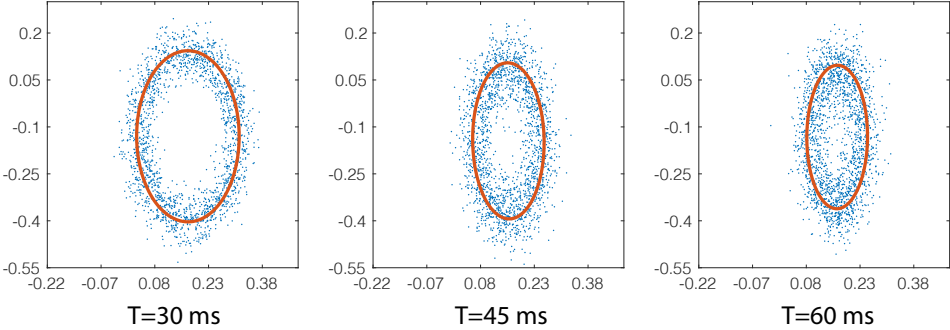
Figure 4.6: Interference ellipses at different T's when $N = 200$.
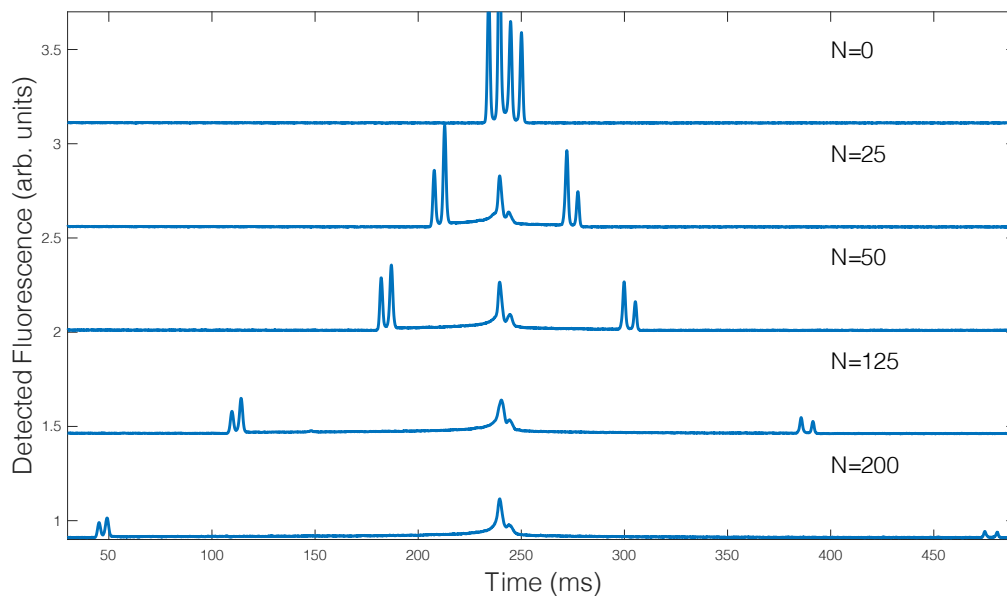
Figure 4.7: Fluorescence signals of the atom clouds as they fall through the detection region, after the interferometer sequence, for varying number N of Bloch oscillations, measured with fixed laser power and acceleration of the atoms during Bloch oscillations. For visibility, a vertical offset has been applied to each trace. The four outer peaks correspond to the four output ports A to D of the interferometers. Atoms left behind by the Bloch oscillations form the central peaks. $T = 5$ ms for these data sets.

Another way to increase Φ_{total} is to apply more Bloch oscillations. We have achieved up to $N = 200$ Bloch oscillations in our experiment. The relative velocity between the output ports A and B in Figure 4.1 reaches 2.9 m/s (830 recoil velocities, 1 recoil velocity of cesium D_2 transition is about 3.5 mm/s) at this setting. However, using a higher Bloch oscillation order will deteriorate the contrast, and lower the maximum T we can achieve. Figure 4.6 shows the typical ellipses we observe when 200 Bloch oscillations are applied. At $T = 60$ ms, the ellipse is barely visible. This is because, when more Bloch oscillations are used, the signal-to-noise ratio will decrease dramatically due to various loss mechanisms, such as single photon scattering and Landau–Zener tunneling. Figure 4.7 shows the fluorescence trace we observe when different number of Bloch oscillations are applied. When higher-order Bloch oscillations are applied, the signal size is much smaller. As atoms stay in the optical lattices of Bloch oscillation beams longer, the decoherence from the spatially varying ac Stark shifts also becomes more severe.

To suppress decoherence from ac Stark shifts, we apply a beam from the same fiber port as the Bragg and Bloch beams, with the same intensity but the opposite single-photon detuning, as suggested in [49]. This beam is single frequency, does not satisfy Bragg resonance, and does not drive Bragg transitions. This beam compensates for the variable ac Stark shifts, and improve the contrast at large T. Figure 4.8 shows the contrasts of the ellipses we observe with and without the compensation beam when $N = 125$ Bloch oscillations are applied. At lower T's, the contrast is lowered by the compensation beam, as the compensation beam introduces additional single photon scattering. But at higher T's, the compensation beam increases the contrast. Loss of contrast with increasing pulse separation time and Bloch order used to limit us to $N \sim 75$ Bloch oscillations at $T = 80$ ms pulse separation time. With the help of the compensation beam, we are able to get useable contrast at an increased Bloch order of $N = 125$ at $T = 80$ ms or $N = 200$ at $T = 60$ ms, as shown in Figure 4.5 and 4.6.

Additional methods have been used to improve the sensitivity of the apparatus. For example, we steer the Bragg beam directions to undo Earth's rotation, thus zero the Coriolis effect on the atoms [53]. Beams from a step-index optical fiber have substantial non-Gaussian intensity tails [84], which will be reflected from the vacuum chamber wall, interact with the atoms and cause decoherence and systematic shifts. To suppress this effect, beams for Bragg diffraction as well as Bloch oscillations first pass through an apodizing filter before they enter the vacuum chamber, as shown in Figure 3.2. Taken together, these efforts allow us to demonstrate more than 12 million radian measured phase and set a record for Ramsey-Bordé interferometers.
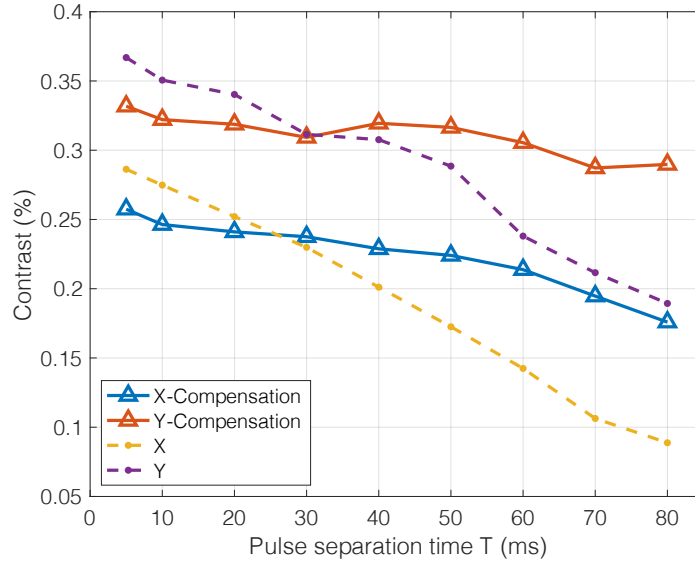
Figure 4.8: Contrast in the interferometer as a function of the pulse separation time T is increased, after the addition of the apodizing filter, for $N = 125$. Data with (blue, solid line) and without (red, dashed line) ac Stark compensation is shown.

4.5 Systematic Effects

Error Budget

Table 4.2 gives an overview of the systematic effects that we have considered. The total systematic uncertainty is controlled at 0.12 ppb level. Many systematic effects like the laser frequency, acceleration gradients caused by gravity and magnetic fields, beam alignment, density shifts, index of refraction from hot and cold atoms, and the Sagnac effect are commonly known in atom interferometers [20]. We also include the systematic effects which have not been considered before, such as the speckle phase shift, thermal motion of atoms, and parasitic interferometers. We will introduce them one by one.

Laser Frequency

The frequency of the reference spectroscopy is monitored using a femtosecond optical frequency comb (Menlo systems). Variations in the laser power used for the reference spectroscopy will result in correlated variations in the lock frequency. We therefore monitor this laser power and apply a dynamical correction to the laser frequency. The long-term stability of this approach has been found to be better than 10 kHz, which results in a 0.03 ppb uncertainty in α [52].

Effect	Direct Measured Value	$\delta\alpha/\alpha$ (ppb)
Laser frequency	$f = 351.74507211$ THz	-0.24±0.03
Acceleration gradient	$\gamma = (2.256 \pm 0.014) \times 10^{-6}$ s^{-2}	-1.79±0.02
Gouy phase	N/A	-2.60±0.03
Beam alignment	N/A	0.05±0.03
Bloch Oscillation light shift	N/A	0±0.002
Density shift	N/A	0±0.003
Index of refraction	N/A	0±0.03
Speckle phase shift	N/A	0±0.04
Sagnac effect	N/A	0±0.001
Modulation frequency wave-vector	N/A	0±0.001
Thermal motion of atoms	N/A	0±0.008
Non-Gaussian waveform	N/A	0±0.03
Parasitic interferometers	N/A	0±0.03
Total systematic error	N/A	**-4.58±0.12**
Statistic error	$h/m_{\text{Cs}} = 3.0023694721 \times 10^{-9}$ m^2/s	**±0.16**
Other studies		
Electron mass [57]	$m_e = 5.4857990907 \times 10^{-4}$ u	±0.02
Cesium mass [8]	$m_{\text{Cs}} = 132.9054519615$ u	±0.03
Rydberg constant [57]	$R_\infty = 1.0973731568508 \times 10^7$ m^{-1}	±0.003
Combined results		
Total uncertainty in α	$\alpha^{-1} = 137.035999046$	**±0.20**

Table 4.2: Error budget of the fine-structure-constant measurement. The laser frequency is the theoretical value without frequency comb calibration. u is the atomic mass unit.
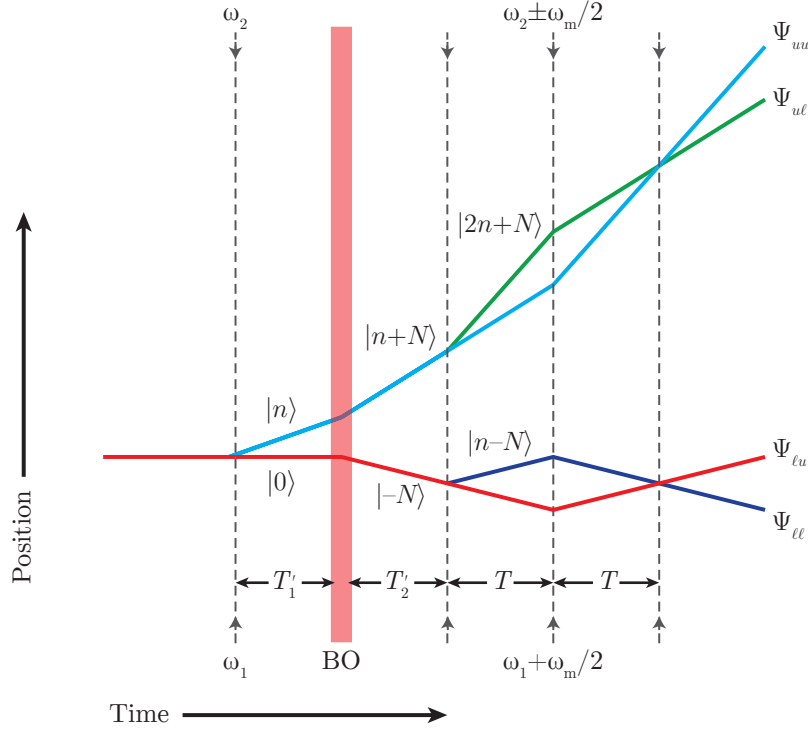
Acceleration gradient

Figure 4.9: Gradiometer Geometry. The interferometer geometry used to measure the gravity gradient. Figure is taken from [66].

The measured phase depends on the acceleration gradient γ, see Equation 4.2. We measure γ in situ using a gradiometer consisting of two vertically separated Mach-Zehnder interferometers [95], as shown in Figure 4.9. The differential phase of this configuration is

$$\Delta\Phi_\gamma = 8n\omega_r\gamma T^2[N(2T - NT_B + 2T'_2) + n(T + T'_1 + T'_2)] + \frac{8gn(n + 2N)T^2\omega_r}{c}, \quad (4.31)$$

where T, T'_1 and T'_2 are separation times defined in Figure 4.9. We take data at $N = 125$, $T'_1 + T'_2 = 50$ ms, with T varying between 60 and 100 ms. γ is measured to be $\gamma = (2.256 \pm 0.014) \times 10^{-6}$ s^{-2}.

We also consider the effect of second-order variations of gravity, the gradient of the gradient. This will be dominated by the local mass distribution, particularly the M $\sim$ 15 kg detection chamber below the atom interferometer. As the atoms are never closer than $r = 40$ cm from the detection chamber, we can calculate the gradient to be at most $2GM/r^3 = 2.9 \times 10^{-8}$ s^{-2} at the closest approach of the atoms, decaying rapidly with distance. If the atom interferometer measuring α and the gravity gradiometer are sensitive to the gradient at the same effective location, this cancels out between the two measurements,

but these locations differ by 5 cm. (Additional suppression is provided by the fact that this extra gradient drops sharply with distance; we will not consider this.) This results in a contribution of 0.01 ppb, which is added in quadrature to the error from the gradiometer measurement for an overall uncertainty of 0.02 ppb. Objects further away have even smaller influences that we neglect. For example, 1000 kg at $r = 2$ m (the optical table weighs about 700 kg) lead to 0.003 ppb and 6×10^3 kg (an estimate for the weight of $(2.5 \text{ m})^2$ of the floor) at 2.5 m to 0.002 ppb.

The effects of magnetic fields can be fully accounted for as a contribution to the acceleration gradient. Our atoms are in the $F = 3$, $m_F = 0$ state and only experience a quadratic Zeeman shift of about $\beta = +213$ Hz/G^2. The magnetic field in the interferometer region can be modeled as a polynomial $B(z) = B_0 + B'z + B''z^2 + ...$ The corresponding energy shift changes the Lagrangian for the atoms by

$$L_B = \frac{g_J^2 \mu_B^2}{4 \Delta E_{\text{hfs}}} B^2(z) \approx \hbar \beta [B_0^2 + 2B_0 B' z + (B'^2 + 2B_0 B'')z^2]. \tag{4.32}$$

The B_0^2 term is common mode to all arms of the interferometer and can be ignored. Comparing this Lagrangian to the one due to gravity, $L = p^2/(2m) - mgz + m\gamma z^2/2$, shows that the term linear in z is similar to the one caused by a linear gravitational potential and cancels out between the two interferometers. The term proportional to z^2 causes an acceleration gradient and can be absorbed into the gravity gradient term by substituting $\gamma \to \gamma + 2\beta(B'^2 + 2B_0 B')/m$. By applying gravity gradient corrections from the gradiometer measurements, we have already dealt with these magnetic gradients.

As an independent verification of this approach, data on the fine structure constant was taken with bias B-fields of 0.38 G and 3.7 G, with the resulting recoil frequencies consistent with each other to within 1σ (1.4 ppb). This puts an upper-bound on any systematic due to magnetic fields at the smaller bias field at 0.014 ppb, which is further reduced after the acceleration gradient is measured and taken out.

Gouy phase

While a plane electromagnetic wave at frequency ω has a wave-vector of exactly $k = \omega/c$, inhomogeneities of the laser intensity will lead to shifts of the wave-vector k as

$$\delta k = \frac{1}{2k} \text{Re}\left(\frac{\nabla_T^2 E}{E}\right), \tag{4.33}$$

where E is the electric field and $\nabla_T^2 = \frac{\partial^2}{\partial x^2} + \frac{\partial^2}{\partial y^2}$ the transverse Laplace operator for a beam propagating along the $z-$axis. Since the photon momentum is proportional to k, the change

in k will shift our measured phase by [95]

$$
\Phi_{\mathrm{Gouy}} = 4n^2\omega_r T\frac{\delta k_2^{\uparrow} + \delta k_2^{\downarrow}}{k} + 2n^2\omega_r T\frac{\delta k_{3l}^{\uparrow} + \delta k_{3l}^{\downarrow} + \delta k_{3u}^{\uparrow} + \delta k_{3u}^{\downarrow}}{k} \tag{4.34}
$$

$$
+ 4nN\omega_r T\frac{\delta k_{Bl}^{\uparrow} + \delta k_{Bl}^{\downarrow} + \delta k_{Bu}^{\uparrow} + \delta k_{Bu}^{\downarrow}}{k} + 4n(N+n)\omega_r T\frac{\delta k_{4l}^{\uparrow} + \delta k_{4l}^{\downarrow} + \delta k_{4u}^{\uparrow} + \delta k_{4u}^{\downarrow}}{k}
$$

$$
+ 2n\omega_r(nT_1' + nT_2' + 2NT_2')\frac{\delta k_{4l}^{\uparrow} + \delta k_{4l}^{\downarrow} + \delta k_{4u}^{\uparrow} + \delta k_{4u}^{\downarrow} - \delta k_{3l}^{\uparrow} - \delta k_{3l}^{\downarrow} - \delta k_{3u}^{\uparrow} - \delta k_{3u}^{\downarrow}}{k}
$$

$$
+ 8nN\omega_r T_1'\frac{\delta k_2^{\uparrow} + \delta k_2^{\downarrow} - \delta k_1^{\uparrow} - \delta k_1^{\downarrow}}{k},
$$

where k_1, k_2, k_3, k_4, k_B represents wave-vectors of the four Bragg pulses and the Bloch beam. The superscript $\uparrow$ or $\downarrow$ indicates the up-going or down-going beam. The subscript u or l indicates the upper or lower interferometer. If E has a Gaussian profile, Equation 4.33 reproduces the usual Gouy phase of a Gaussian beam.

Our laser beam profiles deviate from Gaussian profiles, because they are delivered using a step-index optical fiber and sent through an apodized filter. Imperfection of optics will also lead to small-scale intensity variations on the wavefronts. These small-scale intensity fluctuations do not average out completely, since the probability $P(I)$ of an atom to take part in the interference is a function of the local beam intensity I. In particular, the efficiency of Bloch oscillations rises sharply with intensity near a threshold intensity I_c [9].

To characterize the shift in α due to the Gouy phase, we construct a 3D Monte Carlo simulation which uses actual beam profiles as inputs. The beam profiles are measured with a CCD camera. For each atom position (corresponding to a specific Bragg or Bloch pulse), two images are taken (one for the up-going beam and one for the down-going beam). At each position 10 images are recorded and averaged, and there are 10 positions in total. Fig. 4.10 shows a typical raw image that we recorded. The Monte Carlo is similar to the one described in [65]. It evaluates the motion of a single atom as it interacts with each pulse, calculating not only the complex amplitude for each relevant momentum state, but also the local Gouy phase experienced by the atom at each pulse. The images are filtered using a 5x5 pixel average to suppress the effect of pixel noise (this filter is chosen to match the experimentally observed contrast). The overall Gouy phase shift can be analyzed to be (-2.60 ± 0.03) ppb in α. The error bar is determined by running the Monte Carlo with different images, and finding the histogram of the resulting shifts in α.

Small-scale Intensity Variations

We can verify the scale of the effect of small-scale variations on the beam in two ways: first, with an analytic calculation, and second, by experimental data. For analytic calculation, we average

$$
\left\langle \frac{\delta k}{k} \right\rangle = \frac{1}{k^2}\frac{\langle \kappa P(J) \rangle}{\langle P(J) \rangle}, \quad J \equiv \frac{I}{\bar{I}}, \quad \kappa \equiv \frac{1}{2}\frac{\nabla_{\perp}^2 E}{\bar{E}}, \tag{4.35}
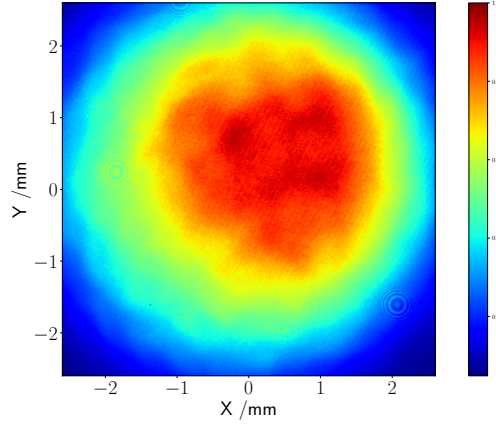$$

Figure 4.10: A raw beam profile image taken by the CCD beam profiler

where $I = |E|^2$ is the intensity and $P(J)$ the intensity-dependent probability that an atom takes part in the interferometer. We assume that J and κ are drawn from a bivariate normal distribution

$$f(J, \kappa) = \frac{1}{2\pi \sigma_J \sigma_\kappa \sqrt{1-\rho^2}} e^{-\frac{1}{2(1-\rho^2)} \left[\frac{(J-1)^2}{\sigma_J^2} + \frac{\kappa^2}{\sigma_\kappa^2} - \frac{2\rho}{\sigma_J \sigma_\kappa} J\kappa \right]}, \tag{4.36}$$

whose covariance matrix is given by

$$\mathrm{cov}\,(J, \kappa) = \begin{pmatrix} \sigma_J^2 & \rho \sigma_J \sigma_\kappa \\ \rho \sigma_J \sigma_\kappa & \sigma_\kappa^2 \end{pmatrix}. \tag{4.37}$$

The parameters of the model can be determined by measuring the autocorrelation function,

$$r_E(\vec{d}) = \frac{1}{\bar{E}^2} \langle [E(\vec{x}) - \bar{E}][E^*(\vec{x} + \vec{d}) - \bar{E}] \rangle, \tag{4.38}$$

where $\bar{E} = \langle E(\vec{x}) \rangle$. We define the spatial derivatives

$$r_E^{(2n)} \equiv \nabla_\perp^{2n} r_E(0), \tag{4.39}$$

where $\nabla_\perp$ is the two-dimensional Laplacian on a beam cross-section. The following results are obtained by integration by parts:

$$\begin{aligned} \bar{E}^2 r_E^{(0)} &= \langle EE^* \rangle - \bar{E}^2 \equiv \sigma_E^2, \\ \langle (E - \bar{E})\nabla_\perp^2 E \rangle &= \langle E\nabla_\perp^2 E \rangle = \bar{E}^2 \nabla_\perp^2 r_E(0) \equiv \bar{E}^2 r_E^{(2)}, \\ \langle (\nabla_\perp^2 E)^2 \rangle &= \langle E\nabla_\perp^2 \nabla_\perp^2 E^* \rangle = \bar{E}^2 \nabla_\perp^4 r_E(0) \equiv E_0^2 r_E^{(4)}. \end{aligned} \tag{4.40}$$

The elements of the covariance matrix Equation 4.37 are thus

$$r_E^{(0)} = \frac{\sigma_J^2}{4}, \quad \sigma_\kappa = \frac{\sigma_J \sqrt{r_4}}{4}, \quad \rho = \frac{r_2}{\sqrt{r_4}}. \tag{4.41}$$

This allows us to determine σ_J and σ_κ from the autocorrelation function: Since $\sigma_J = 2\sigma_E/\bar{E}$,

$$
\begin{aligned}
\sigma_J^2 &= \left\langle \frac{(I - I_0)^2}{I_0^2} \right\rangle = 4 \left\langle \frac{(E - E_0)^2}{\bar{E}^2} \right\rangle = 4 r_E^{(0)}, \\
\sigma_\kappa^2 &= \frac{1}{4\bar{E}^2} \left[\langle (\nabla_\perp^2 E)^2 \rangle - \langle \nabla_\perp^2 E \rangle^2 \right] = \frac{1}{4} r_E^{(4)},
\end{aligned}
\tag{4.42}
$$

where we have used that

$$
\langle \nabla_\perp^2 E \rangle = \iint \vec{\nabla}_\perp \cdot \left(\vec{\nabla}_\perp E \right) d^2 x = \oint_s \hat{n} \cdot \vec{\nabla}_\perp E \, dx = 0,
\tag{4.43}
$$

which holds because $\vec{\nabla}_\perp E$ goes to zero quickly enough. Furthermore,

$$
\rho \sigma_J \sigma_\kappa = \left\langle 2\frac{E - \bar{E}}{\bar{E}} \frac{1}{2} \frac{\nabla^2 E}{\bar{E}} \right\rangle = \frac{1}{\bar{E}^2} \langle (E - \bar{E}) \nabla^2 E \rangle = r_E^{(2)}.
\tag{4.44}
$$

Therefore,

$$
\text{cov}\,(J, \kappa) = \begin{pmatrix} 4 r_E^{(0)} & r_E^{(2)} \\ r_E^{(2)} & r_E^{(4)}/4 \end{pmatrix},
\tag{4.45}
$$

where $r_2 = r_E^{(2)}/r_E^{(0)}$ and $r_4 = r_E^{(4)}/r_E^{(0)}$.

From this model, the results in Ref. [10] can be reproduced. They have assumed a flat-top beam intensity distribution and that $P(J)$ is Heaviside-shaped

$$
P(J) = \theta(J - J_c),
\tag{4.46}
$$

where J_c is a critical intensity. In this case, $\langle \delta k/k \rangle = A/(Bk^2)$ where

$$
\begin{aligned}
A &= \int \kappa P(J) f(J, \kappa) dJ d\kappa = \frac{\sigma_\kappa \rho}{\sqrt{2\pi}} e^{-(J_c - 1)^2/(2\sigma_J^2)}, \\
B &= \int P(J) f(J, \kappa) dJ d\kappa = \frac{1}{2} \text{erfc}\left(\frac{J_c - 1}{\sqrt{2}\sigma_J} \right).
\end{aligned}
\tag{4.47}
\tag{4.48}
$$

If we assume a Gaussian autocorrelation function,

$$
r_E(\vec{d}) = r_E^{(0)} e^{-\frac{d^2}{2\ell^2}}, \quad r_E^{(2)} = \frac{-2 r_E^{(0)}}{\ell^2}, \quad r_E^{(4)} = \frac{8 r_E^{(0)}}{\ell^4},
\tag{4.49}
$$

we obtain

$$
\left\langle \frac{\delta k}{k} \right\rangle = -\frac{\sigma_J}{k^2 \ell^2 \text{erfc}\left(\frac{J_c - 1}{\sqrt{2}\sigma_J} \right)} e^{-(J_c - 1)^2/(2\sigma_J^2)}.
\tag{4.50}
$$

If we insert, e.g., $\ell = 180\,\mu\text{m}$, $\sigma_J = 0.01$, and $J_c = 0.8$, we obtain $\langle \delta k/k \rangle = -1.5 \times 10^{-96}$. The model of a constant beam intensity is too optimistic, as the influence of intensity noise

will rise sharply when the beam intensity I_0 approaches the critical intensity I_c at a certain radius from the center of the beam.

For a more realistic model, consider a laser beam with a Gaussian envelope,

$$J(r) = e^{-2r^2/w_0^2}, \tag{4.51}$$

where J is normalized to the peak intensity in the middle of the beam. We assume that the fractional amplitude noise in the laser beam is constant over the beam. We also assume Gaussian distribution of atoms,

$$\rho = \rho_0 e^{-r^2/2\sigma_c^2}. \tag{4.52}$$

To average $\langle \kappa P(J) \rangle$ over all radii, we calculate

$$
\begin{aligned}
\langle \kappa P(J) \rangle_r &= \sqrt{2\pi} \rho_0 \sigma_\kappa \rho \int_0^\infty r e^{g(r)} dr, \\
g(r) &= -\frac{(e^{-2r^2/w_0^2} - J_c)^2}{2\sigma_J^2} - \frac{r^2}{2\sigma_c^2}.
\end{aligned}
\tag{4.53}
$$

We now study the argument $g(r)$ of the exponential function. If $\sigma_J \ll 1 - J_c$, then $e^{g(r)}$ will be sharply peaked at the maximum of $g(r)$ at $r = r_0$. It is then sufficient to evaluate the integrand in this neighborhood. After a lengthy calculation, which involves a Taylor expansion of the exponent around r_0, we find

$$\frac{\delta k}{k} = \frac{\sigma_J r_E^{(2)} w_0^2}{16 r_E^{(0)} \sigma_c^2 k^2} J_c^{\frac{w_0^2}{4\sigma_c^2} - 1} \frac{1}{1 - \left(\frac{1}{I_c}\right)^{-w_0^2/4\sigma_c^2}}. \tag{4.54}$$

We determine the autocorrelation function from CCD images. The autocorrelation function is then fit to a 2D 4th-order polynomial using a least-squares algorithm. The rms amplitude of the noise is about 0.65% of the beam intensity, and $r_I^{(2)} = 2.44 \times 10^{-9}/\mu\text{m}^2$. With $w_0 = 3.5\,\text{mm}$, $I_c = (0.85 \pm 0.05)I_0$, and $\sigma_c = 0.58\,\text{mm}$, we find the magnitude of this systematic effect to be $-0.030 \pm 0.019\,\text{ppb}$.

We can also check the validity of this result by directly measuring the shift in α as the Bloch intensity is varied. The measured dependence on the Bloch efficiency is shown in Figure 4.11. No dependence is observed within 0.3 ppb (limited by statistics), consistent with the results of the analytic calculation and Monte Carlo simulation.

As a final check that the Gouy phase was accounted for correctly, data was taken with two different beam waists (the 5.7 mm beam and the apodized beam). The α values from these two measurements were within 1σ (Figure 4.12).

Beam Alignment

Misalignment of the retro-reflection angle θ of the Bragg beam reduces the effective wave vector as

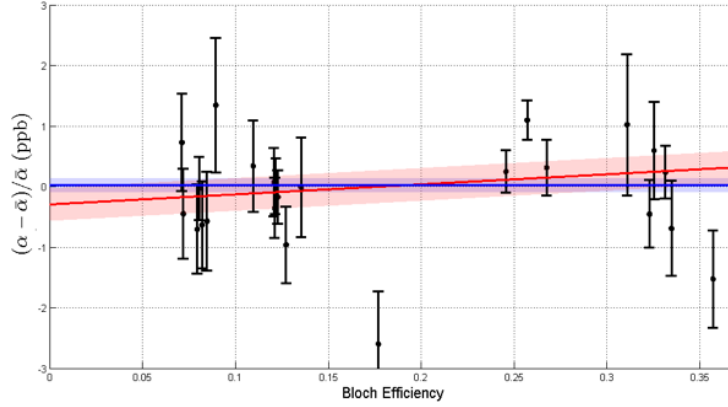$$k_{\text{eff}}^2 \approx k^2 \frac{1 + \cos\theta}{2} \approx k^2 - \frac{k^2\theta^2}{4}. \tag{4.55}$$

Figure 4.11: Experimental measurements of α, as the Bloch efficiency (i.e. intensity) is varied. The blue line is the final reported value of α, assuming no dependence on Bloch efficiency. The red line assumes a linear dependence; the shaded regions represent 1σ error bars.
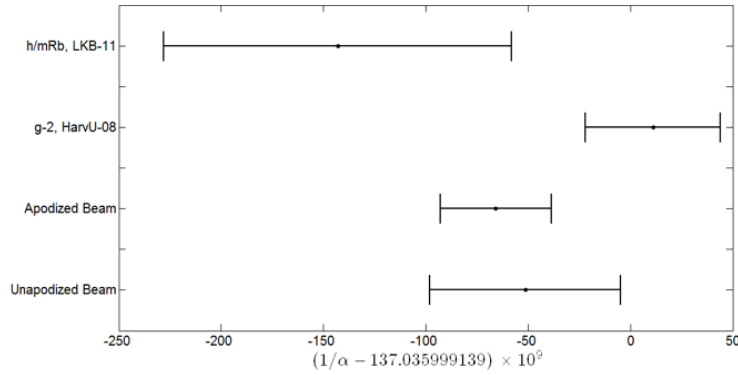
Figure 4.12: Experimental measurements of α, for two different beam sizes (the unapodized 5.7 mm beam, and the apodized flat-top beam). Also plotted are the LKB-11 and g_e-2 measurements of α for reference.

To measure θ, we monitor the back-coupling efficiency of the light to the fiber. We calibrated the back-coupling efficiency as a function of angle. By measuring the coupling efficiency during the experimental run, the relative angle (typically around 12 μrad) can thus be determined which allows for post correction of the data to reduce the beam alignment systematic.

Bloch Oscillation Light Shift

During Bloch oscillations, the atoms are shifted in energy by an amount

$$\delta E_{ac} = \frac{\hbar\Omega^2}{4\Delta} \tag{4.56}$$

due to the ac Stark effect, where Ω is the (local) Rabi frequency of the optical lattice on the atoms and Δ is the single-photon detuning. This light shift enters the phase of the interferometer. The energy shift applies for each component of the Bloch lattice beam for a total of 6 beams, as the three frequencies ω_1, $\omega_\pm$ travel up and down after retro-reflection. Since the Bloch lattice is blue-detuned, the atoms sit at a potential minimum of the lattice used to accelerate them. The dominant ac Stark shift is thus caused by the time-averaged energy shift from the remaining four beams, which is a function of the beam intensities at the location of the atoms.

Denote $I_1^\uparrow(z)$, $I_\pm^\uparrow(z)$ the intensities of these frequencies as function of z in the up-going laser beam and $I_1^\downarrow(z)$, $I_\pm^\downarrow(z)$ the same in the down-going beam. Denote z_{1-4} the positions of the partial wave packets during Bloch oscillations, measured relative to the top mirror, where z_1 is the position of the initially uppermost wave packet and z_4 the initially lowest.

For the atoms being accelerated upwards, the dominant ac Stark shift arises from $I_\pm^\uparrow$ and $I_1^\downarrow$, $I_+^\downarrow$. For the atoms being accelerated downwards, the dominant ac Stark shift arises from $I_\pm^\uparrow$ and $I_1^\downarrow$, $I_-^\downarrow$. Defining the abbreviation $J = I_-^\uparrow + I_+^\uparrow + I_1^\downarrow$, the total ac Stark shift entering the interferometer phase is proportional to $\Delta I = J(z_1) - J(z_3) - J(z_2) + J(z_4) + I_+^\downarrow(z_1) - I_+^\downarrow(z_3) - I_-^\downarrow(z_2) + I_-^\downarrow(z_4)$. This is valid for any shape or intensity profile of the laser beam.

A systematic shift can arise from the propagation of our Gaussian laser beam. To determine it, we write $z_1 = z_4 + d + \delta$, $z_2 = z_4 + d$, $z_3 = z_4 + \delta$, where $d = 2nv_rT$ is the separation of the interferometer arms and δ is the distance between the two interferometers during Bloch oscillations. We expand the intensities as $I(z_4 + \epsilon) = I + I'\epsilon + I''\epsilon^2/2$, where I, I', I'' are the intensities and their derivatives taken at z_4. This yields

$$\Delta I \approx \left[(I_+^\downarrow)' - (I_-^\downarrow)'\right]d + \left[J'' + (I_+^\downarrow)''\right]\delta d + \frac{1}{2}\left[(I_+^\downarrow)'' - (I_-^\downarrow)''\right]d^2. \tag{4.57}$$

The dominant contribution is the first term. The two beams involved come from the same optical fiber and were both retro-reflected at the mirror. The z-dependence of their intensities as well as any retro-reflection losses are thus common to both, and the derivatives are

$$(I_\pm^\downarrow)' = I_{0,\pm} \frac{2}{z_R^2} \frac{z_4 - z_0}{\left(1 + \frac{(z_0 - z_4)^2}{z_R^2}\right)^2}, \tag{4.58}$$

where z_0 and z_R are the common location of the waist and the Rayleigh range of these beams and $I_{0,\pm}$ are the intensities of the two beams at the waist. With $z_R = 35.0$ m, $z_0 - z_4 = 1.5$ m, $n = 5$, $v_r = 3.5$ mm/s, $T = 80$ ms, we obtain $\Delta I \approx 6.8 \times 10^{-6}(I_{0,+} - I_{0,-})$.

Each beam by itself causes an AC Stark shift of about $1.5\hbar\omega_r$ and within the 8-ms duration of our Bloch oscillations causes a phase shift of about 0.16 krad. With a 2% intensity balance between $I_{0,+}$ and $I_{0,-}$ (verified by comparing the Bragg diffraction efficiency when kicking atoms up and down), we estimate $\Delta\Phi_{\text{ac}} = 0.16\,\text{krad} \times 6.8 \times 10^{-6} \times 0.02 \sim 22\,\mu\text{rad}$, a 0.002 ppb change in α for $n = 5$, $N = 125$, $T = 80$ ms.

Density Shift

The energy shift in our cloud due to density shifts can then be approximated as

$$E_\rho = \frac{\rho 4\pi\hbar^2 a_s}{m}, \tag{4.59}$$

where $a_s = 280(10)a_0$ for cesium in the $F = 3$ state and a_0 the Bohr radius. For typical interferometer signals, the atom number density during detection is approximately 2.5×10^5 atoms/cm^3, and the density during the interferometer sequence is approximately 10^6 atoms/cm^3. For an exaggerated beam splitter imbalance of 3:1, the differential density shift will cause a net interferometer phase of

$$\Delta\Phi_{\text{Density}} = \frac{\Delta E_\rho}{\hbar}(2T + T') = \left(\frac{3\rho}{4} - \frac{\rho}{4}\right)\frac{4\pi\hbar a_s}{m}(2T + T') \tag{4.60}$$

For typical parameters of $T = 80$ ms and $T' = 10$ ms, this gives a phase of 8 μrad corresponding to a negligible 0.003 ppb shift in ω_r.

Index of Refraction

The effective wave vector k_{eff} of the laser is sensitive to the refractive index in the vacuum chamber, arising from room-temperature as well as cold background cesium atoms. The refractive index in an atomic vapor in the far-detuned limit is

$$n - 1 = \frac{\sigma_0 \rho \Gamma}{4k\Delta}, \tag{4.61}$$

where $\sigma_0 = 2.5 \times 10^{-9}$ cm^2 is the resonant cross section, ρ is the atom number density, Γ is the natural linewidth, $\Delta \approx 14$ GHz is the single photon detuning. As an upper bound for the density of cold cesium atoms, we use the density of the atom cloud during the interferometer sequence, 10^6 atoms/cm^3. The corresponding index of refraction is below $n - 1 = 0.003$ ppb, which we take to be negligible. The dominant contribution comes from room-temperature background atoms. An upper bound of 10^7 atoms/cm^3 on their density is obtained by assuming that the entire vacuum pressure of 10^{-9} torr is due to cesium, and the corresponding index of refraction shift is at most $n - 1 = 0.03$ ppb. For our low atom densities, no detailed simulation of the atom cloud is needed.

Speckle phase

The speckle phase is an estimate for any residual uncertainties that arise from stray reflection of the laser beam by the walls of the vacuum chamber. A single-mode, step-index optical fiber delivers a Gaussian beam only near the beam axis. Beyond a certain radius (typically at 10% of peak intensity), the beam intensity drops more slowly [84]. Thus, substantial intensity can be reflected off the vacuum chamber walls and interfere with the main beam, causing an irregular spatial dependent speckle pattern that led to random variations of the interferometer phase Φ_d as the pulse separation time was varied. This random phase variation can be as large as 30 mrad (see Figure 4.13, red data points).
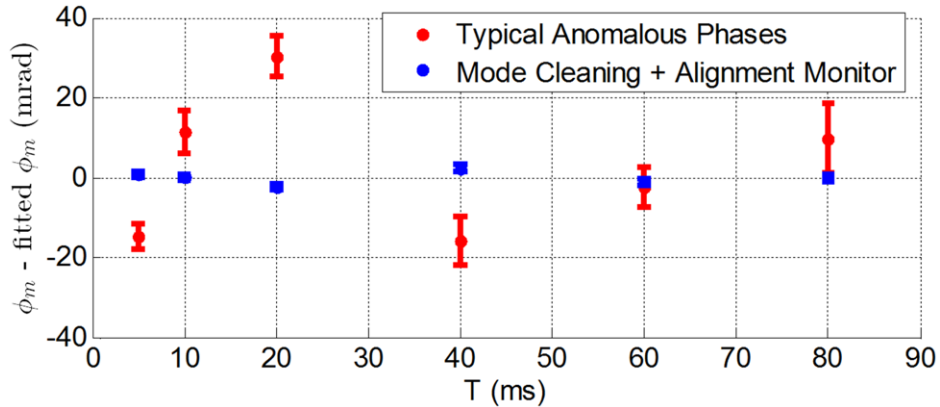

Figure 4.13: Anomalous phases measured after subtracting off all other known systematic errors, with $N = 0$. With no effort taken to suppress them, the speckle phases can be as large as 30 mrad (red data). With the real-time fountain monitor and apodizing filter, the speckle phases are kept below 3 mrad.

To reduce the amount of scattered light, we add an apodizing filter (Thorlabs NDYR20A) to the output of the fiber port, gradually attenuating the intensity as a Gaussian function of distance from the beam axis, as shown in Figure 3.2. The random phase variations caused by speckle is thus suppressed below 3 mrad (see Figure 4.13, blue data points).

Empirically, we found the speckle phase shifts to be independent of the Bloch order. Therefore, we can reduce their fractional significance by increasing the Bloch order. When $N = 0$, without mode cleaning (Figure 4.13, red), the T-dependent random phase variation would cause an about 8 ppb uncertainty in α. With mode cleaning (Figure 4.13, blue), the random phase variation is reduced by an order of magnitude. Operating at $N = 125$ further reduces the effect by a factor $n/(n+N) = 0.04$. Therefore, we expect a possible contribution to the error budget of approximately 0.03 ppb.

In order to verify this residual effect of any (unresolved) anomalous phases, residual stochastic variation in the data, we implement a model to estimate the error under the assumption that the residuals are entirely due to speckle phases (and not due to random

statistical fluctuations). The systematic error for the residuals shown in Figure 4.14 is below 0.04 ppb in α.

The data in Figure 4.14 verifies both our understanding of systematic shifts and the speckle phase. Any anomalous phase shifts that depend on the pulse separation times T are suppressed to the point where any remaining anomalous phases are unresolved.
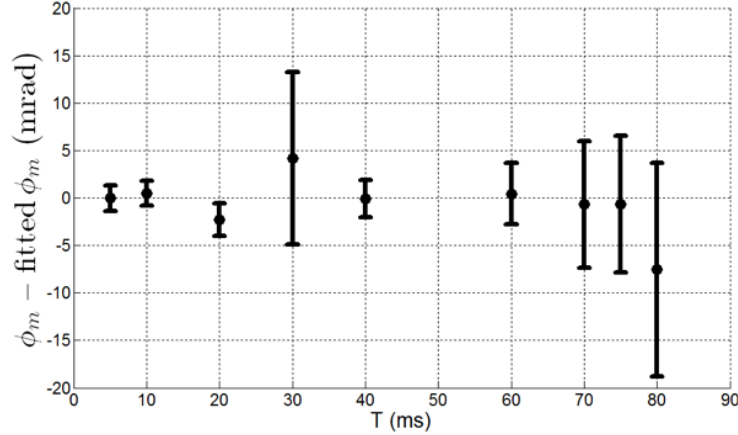

Figure 4.14: Anomalous phases measured after subtracting off all other known systematic errors, with the real-time fountain alignment monitor, apodizing filter, and $N \geqslant 125$. These are the residuals vs T for the data shown in Figure 4.4.

Sagnac Effect

Our Ramsey-Bordé interferometer configuration ideally has zero enclosed spatial area because all motion takes place in the vertical direction. If there is a misalignment such that the two interferometer paths enclose a spatial area A, then there will be an extra phase shift

$$\Phi_\Omega = \frac{4\pi m}{\hbar} \vec{A} \cdot \vec{\Omega}, \tag{4.62}$$

due to the Sagnac effect, where Ω is the rotation vector. The enclosed areas of the upper and lower interferometers mostly cancel, but a difference arises because of the gravity gradient γ if the laser beams are rotating in the atom's inertial frame at a rate ω as a result of imperfect Coriolis compensation. The laser rotation rate is zero with perfect Coriolis compensation and $\omega = \Omega_e$ (i.e. the rotation rate of the Earth) without compensation. The difference in area between the upper and lower interferometers is then

$$A_u - A_l = -n(n+N)v_r^2 T^2 \left[\frac{4}{3}(12 + \gamma T^2) - (12 + 5\gamma T^2)\cos\omega T \right] \sin\omega T, \tag{4.63}$$

which is below 0.001 ppb after being cancelled to below 10% using Coriolis compensation.

Modulation Frequency Wave-vector

$\Phi_{\delta k}$ in Equation 4.3 depends the gravity acceleration. Since the value of $g = \vec{g} \cdot \vec{k}/|k|$ is the projection of gravity onto the wave-vector, the vertical alignment of the Bragg beam introduces a slight uncertainty, but even with a misalignment as large as 10 mrad, it is below 0.001 ppb.

Thermal Motion of Atoms

According our data analysis method introduced in Section 4.3, the diffraction phase Φ_0 does not produce a systematic effect in α to leading order. However, there are higher-order effects that can produce a systematic effect by causing the diffraction phase to vary with the pulse separation time T. The dominant effect comes from the thermal motion of the atoms as they ballistically expand - this causes the atoms to see a different Bragg pulse intensity at different times during the interferometer sequence. Expanding the diffraction phase Φ_0 to first order in T results in an extra phase term when the total interferometer phase $\Phi_d = 0$, so that now the interferometer output is given by

$$2n\omega_m T = 16n(N+n)\omega_r T + \Phi_0 + \frac{d\Phi_0}{dT}T. \tag{4.64}$$

The extra term will contribute an uncertainty in α as

$$\frac{\delta\alpha}{\alpha} = \frac{\frac{1}{2}\frac{d\Phi_0}{dT}}{16n(N+n)\omega_r}. \tag{4.65}$$

One strategy to reduce this systematic effect is using a large number N of Bloch oscillations. This will increases the total measured phase, thus lower the fractional significance. It also further separate the two interferometers, reducing the influence of the off-resonant component of the dual-frequency Bragg pulses in each respective interferometer, and lowering the diffraction phase Φ_0.

To quantify this systematic effect, we run an end-to-end Monte Carlo simulation. The simulation is based on a Gaussian density and velocity profile of the initial atomic cloud. It takes into account the effect of state and velocity-selection pulses as well as the Bragg pulses at the location of each atom. Systematic effects from non-Gaussian waveform and parasitic interferometers are also included in the simulation (see the following subsections). The simulation also takes into account the ellipse fitting algorithm, and therefore its result will include any residual systematic effects from ellipse fitting. Details of the simulation can be found in reference [65]. The simulation is run for the particular experimental parameters (Bragg pulse intensity, cloud temperature, etc.) used in this work, as well as 1σ variations in those parameters limited by the experimental repeatability. The resulting systematic shifts are presented in Table 4.3. We run the simulation enough times so that each shift is well-resolved compared to the numerical error bar. In total the thermal motion of the atoms introduces a systematic uncertainty of 0.08 ppb in α.

Effect	Direct Measured Value	$\delta\alpha/\alpha$ (ppb)
Cloud radius (mm)	2.2 ± 1	± 0.026
Vertical velocity width (v_r)	1.5 ± 0.25	± 0.031
Ensemble horizontal velocity (v_r)	0 ± 0.5	± 0.032
Initial horizontal position (mm)	0 ± 1	± 0.034
Intensity ($I_{\pi/2}$)	1.02 ± 0.02	± 0.028
Last pulse intensity ratio	1.0 ± 0.02	± 0.034

Table 4.3: Results of Monte Carlo simulation quantifying the systematic shifts arising from thermal motion of the atoms, which introduces distortion in the ellipses used for phase extraction. The parameters used in the model are allowed to vary, replicating the level of control achieved in the actual experiment.

Non-Gaussian Waveform

The T-dependent diffraction phases described in the previous subsection can be amplified by imperfections in the experimental setup, particularly if the temporal waveform used for the Bragg diffraction is significantly non-Gaussian. A detailed treatment is given in Reference [65]. By using an intensity servo to stabilize the temporal waveform to a reference Gaussian waveform, this systematic effect can be kept below 0.03 ppb.

Parasitic Interferometers

As discussed in Reference [65], the multi-port nature of Bragg diffraction allows for the formation of unwanted Ramsey-Bordé interferometers that will close at the same time as the main interferometer and will not be suppressed by Bloch oscillations. These unwanted interferometers will produce small, oscillating phase shifts as the pulse separation time T is varied, and can produce a systematic shift as large as 1 ppb in α. Using the Monte Carlo described above, it was determined that the dominant contribution to this effect comes from unwanted population in the $n = 1$ order, which can be suppressed by appropriate choice of the Bragg pulse duration (109 μs for our experimental parameters). The simulation's prediction of the parasitic phases is in good agreement with experimental data, and the expected systematic shift at the 'magic' Bragg duration is below 0.03 ppb in α. See Reference [65] for more detail.

4.6 Discussion

Test the Standard Model

With a statistical uncertainty of 0.16 ppb and a systematic uncertainty of 0.12 ppb, the overall uncertainty of α reaches 0.20 ppb. This is a more than threefold improvement over the previous measurements of α using atom interferometry (see Figure 1.1). Using our measurement, the the electron's gyromagnetic anomaly can be calculated from Equation 1.2 as

$$a_e(\alpha) = \frac{g_e - 2}{2} = 0.00115965218161(23). \tag{4.66}$$

As discussed in Section 1.2, this calculation takes into account the contributions from QED theory as well as electroweak and hadronic contributions. Thus a comparison of the calculated value and the directly measured value can provide a test of the Standard Model of particle physics.

Comparison of the calculated value of a_e using our result with the most precise directly measured value [39] yields

$$\delta a_e = a_{e,\text{meas}} - a_e(\alpha) = -0.88(0.36) \times 10^{-12}. \tag{4.67}$$

For the first time, this kind of comparison reaches an error bar below the 5$^{\text{th}}$-order QED contribution to a_e (0.45×10^{-12}). It allows us to confront QED calculations with experiment. It also shows a $2.5\,\sigma$ tension between the theoretical calculation and experiment measurement. Based on frequentist statistics, the tension indicates that the Standard Model by itself is not consistent with existing measurements at 99% confidence level (C.L.). While this is not statistically significant enough to claim discovery of new physics, it warrants further investigation. Here we will talk about the implication of this tension on dark-sector particles. In particular, we consider dark photons and dark axial-vector bosons.

Dark Photons

A hypothetical gauge boson A' with mass $m_{A'}$ would couple to the Standard Model leptons through a Lagrangian [45, 25]

$$\mathcal{L}_{\text{coupling}} = A'_\mu \sum_f \bar{f}(c_V^f \gamma^\mu + c_A^f \gamma^\mu \gamma^5)f, \tag{4.68}$$

where A'_μ and f are fields of the bosons and leptons, respectively; γ_μ are Dirac matrices; c_V^f and c_A^f are vector and axial vector coupling constants to lepton f. The coupling constant c_V^f is sometimes written as $-e\epsilon$, where -e is electron's charge and ϵ the commonly used kinetic mixing parameter.

A dark photon is a vector boson. Based on QED, couplings of dark photons and electrons would lead to a nonzero shift in electron's gyromagnetic anomaly as [45]

$$\delta a_e = \frac{c_v^2}{4\pi^2} \int_0^1 \frac{x^2(1-x)}{x^2 + \frac{m_v^2}{m_e^2}(1-x)} dx. \tag{4.69}$$

In particular, dark photons are one proposed explanation for the well-known 3.7σ discrepancy between the prediction for the muon's a_μ and its measurement [14, 67]. However, dark photons cause a $\delta a_e > 0$, opposite to the sign measured in both our experiment and the rubidium measurement [16, 66]. With the improved error of our measurement, this tension has grown. A model consisting of the Standard Model and dark photons of any mass m_V or coupling c_V now is incompatible with our result at 99% C.L. according to frequentist statistics.

Figure 4.15 shows excluded parameter space for dark photons as a function of the dark-photon mass m_V and kinetic mixing parameter ϵ. Two statistical methods have been used to generate the excluded region using our results: the standard frequentist statistics and a more conservative method called power-constrained limits (PCL) [96]. For frequentist statistics, we use 99% C.L. For PCL, we use 90% C.L. and $M_{\min} = 16\%$. The figure also shows limits obtained from accelerator experiments. BaBar is searching for invisible decay of a dark photon produced in e^+e^- collision at SLAC [55]; NA64 is searching dark photons that decay into e^+e^- pairs at the European Organization for Nuclear Research (CERN) [11, 12]; E787 and E949 are searching rare kaon decays at Brookhaven National Laboratory (BNL)[1, 6]. Finally, the figure also shows the excluded region based on previous α measurement at LKB [16] and 2σ preferred region of muon $g_\mu - 2$ measurement [25, 57].

When comparing limits on dark photons, it should be noted that limits obtained from α and the gyromagnetic anomaly do not depend on assumptions on branching ratios for the decay of dark photons. Tabletop experiments like ours are as competitive as major accelerator experiments in searching new physics beyond the Standard Model.

Dark Axial-Vector Boson

A dark axial vector boson characterized by an axial vector coupling constant c_A and mass m_A would shift electron's gyromagnetic anomaly by [45]

$$\delta a_e = \frac{c_A^2}{4\pi^2} \frac{m_e^2}{m_A^2} \int_0^1 \frac{2x^3 + (x - x^2)(4 - x)\frac{m_A^2}{m_e^2}}{x^2 + (1-x)\frac{m_A^2}{m_e^2}} dx. \tag{4.70}$$

Contrary to dark photons, dark axial vector bosons are favored by our result because it would lead to a negative δa.
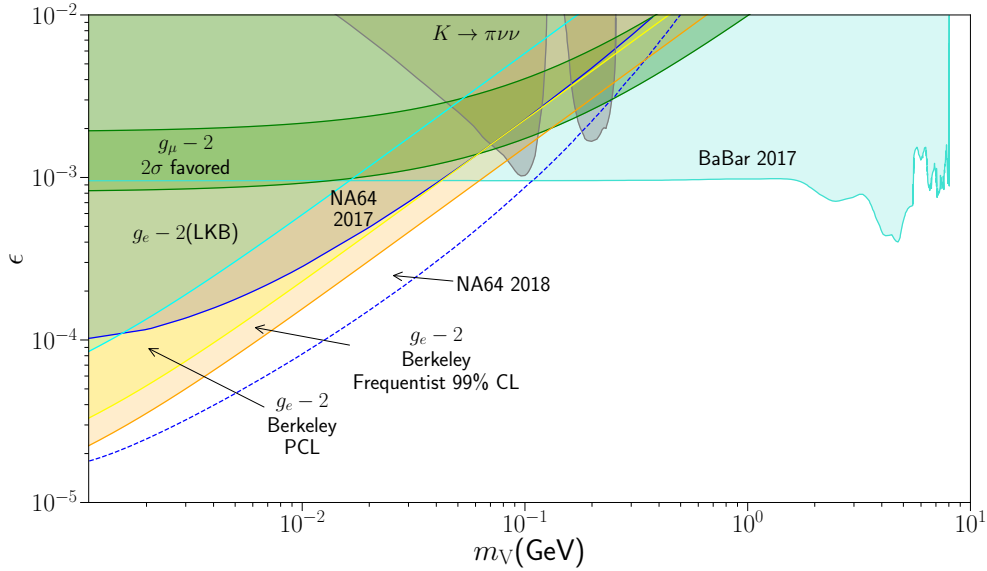
Figure 4.15: Excluded parameter space for dark photons as a function of the dark-photon mass m_V and kinetic mixing parameter ϵ. The green band is a 95% C.L. in which the muon $g - 2$ is explained by a dark photon based on frequentist statistics [57]. Constraints from BaBar were based on Bayesian limit/ frequentist profile likelihood statistics at 90% C.L. [55]. The profile likelihood method [74] is similar to CL_s. Constraints from rare kaon decay were obtained from BNL E787+E949 experiments at 95% C.L. [1, 6]. Constraints from NA64 2017 and NA64 2018 were based on CL_s statistics at 90% C.L. [11, 12]. Both electron $g_e - 2$ for LKB and Berkeley were analyzed under frequentist statistics at 99% C.L. [57, 39, 16, 66]. We have also included the excluded region of the Berkeley result analyzed under PCL($M_{\min} = 16\%$) with 90% C.L. This figure is taken from [96].

Figure 4.16 shows the excluded parameter space for dark axial vector bosons, as a function of mass m_A and axial-vector coupling constant c_A. The calculated δa using our result places limits on the axial vector parameter space from two sides. The allowed region is partially ruled out by other experiments. However, the region of parameter space consistent with our result and anomalous pion decay is also consistent with current accelerator limits. Here we emphasize that the 2.5σ tension in the data is insufficient to conclude the existence of a new particle. But the remaining region of parameter space warrants further study [45].

Electron Substructure

Our measurement can be used to probe a possible substructure within the electron. An electron whose constituents have mass $m* \gg m_e$ would result in a modification of the electron magnetic momentum by $\delta a \sim m_e/m*$. In a chirally invariant model, the modification scales as $\delta a \sim (m_e/m*)^2$. Following the treatment in [35], the comparison $|\delta a|$ of this measurement
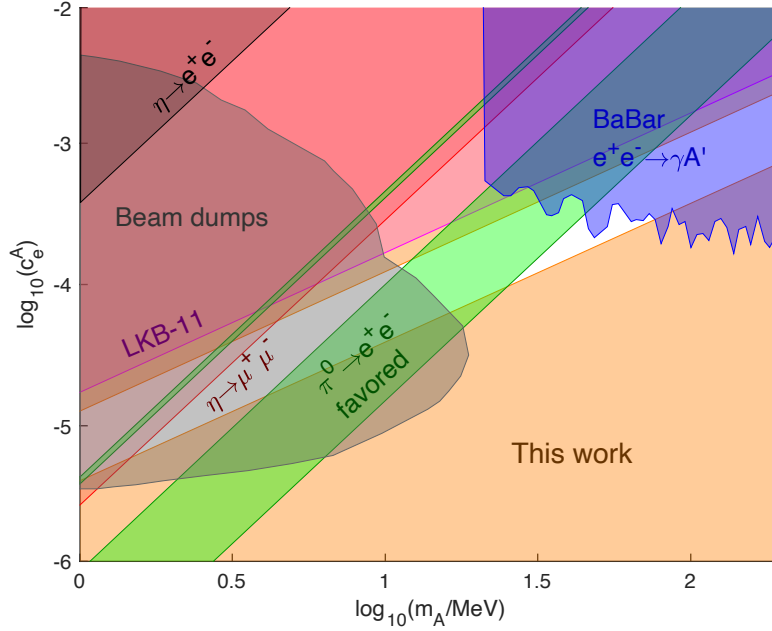
Figure 4.16: Excluded parameter space for dark axial vector bosons, as a function of mass m_A and axial-vector coupling constant c_A, whose existence would produce a negative δa and is thus favored. Our work results in a two-sided bound. The region suggested by anomalous pion decay is shown in green [45] at 95% CL. Accelerator limits are adapted from [55].

of α with the electron $g_e - 2$ result places a limit to a substructure at a scale of $m* > 411,000$ TeV/c^2 for the simple model and $m* > 460$ GeV/c^2 for the chirally invariant model (improvements over the previous limits of $m* > 240,000$ TeV/c^2 and $m* > 350$ GeV/c^2, respectively).

Chapter 5

Offset Simultaneous Conjugate Interferometers

5.1 Overview

In the α measurement that we discussed in Chapter 4, we successfully cancel the effect from gravity to first order by running two conjugated Ramsey-Bordé interferometers simultaneously and measuring the phase difference between them. However, because these two interferometers are running at different heights, the cancellation is not perfect. The second order effect, the gravity gradient γ, still enters the differential phase (see Equation 5.6). It is one of the largest corrections that needs be applied to α, as shown in Table 4.2. Inhomogenous magnetic fields and blackbody radiation [40] will cause effects similar to γ. We characterize the effect from γ by measuring it in situ with two vertically separated Mach-Zehnder interferometers, as shown in Figure 4.9. But this strategy takes long time to take data, and would inevitably assign an error to the measured γ, introducing uncertainty in α. In order to perform a more accurate measurement of α, we would want to find a way that can completely zero the effect from γ.

In this chapter, we propose and demonstrate a new atom interferometer geometry: Offset Simultaneous Conjugate Interferometers (OSCIs, Figure 5.1) [98]. This geometry can exactly cancel the effects of acceleration gradients. It can also substantially reduce diffraction phases from Bragg beam splitters. We split one atom sample into two using one Bragg diffraction pulse and two Bloch oscillation sequences. We then create two sets of simultaneous conjugate interferometers (SCIs) to form a multi-channel interferometer. The vertical offset between the two SCIs is precisely controlled by the timing of these two Bloch oscillation sequences. Different channels of this geometry can be used to amplify or suppress specific signals. Importantly, the offset required to cancel the gradient is independent of the magnitude of the gradient. The undesired diffraction phase from the Bragg beam splitters is suppressed due to the symmetry of this geometry. With these advantages, we expect this geometry to be useful for the next generation of the α measurement.
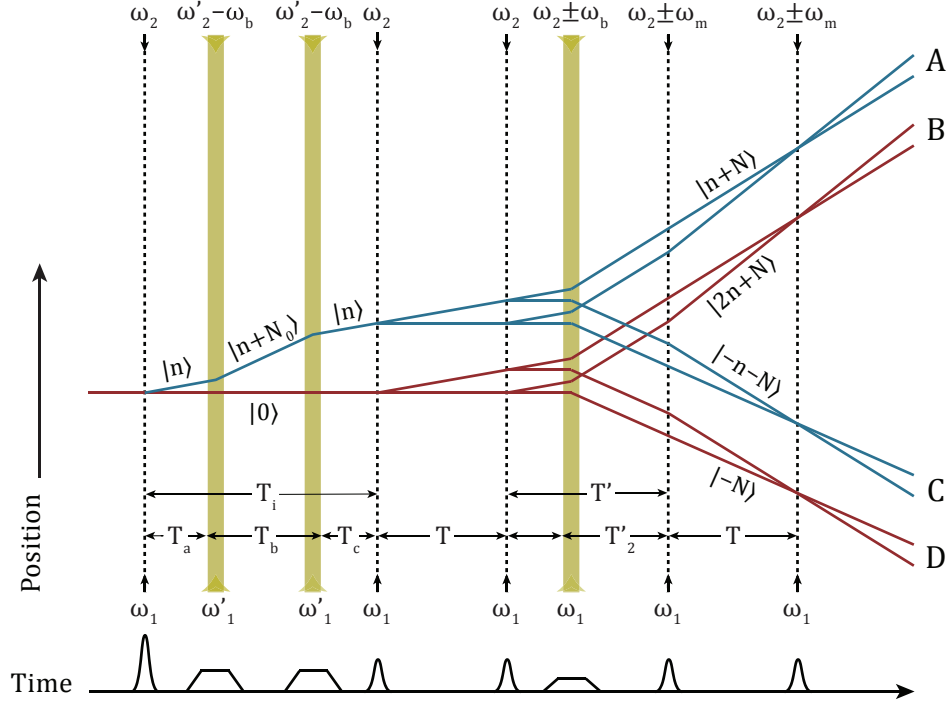
Figure 5.1: The upper panel shows the pulse sequence and atom trajectories in OSCIs. Every dashed line represents a pair of counter-propagating laser pulses that drive Bragg diffraction. Yellow bands represent the optical lattices that drive Bloch oscillations. We split the atom sample into two with one Bragg pulse and two Bloch oscillation sequences, and create two sets of SCIs (the blue one and the red one). The four output ports A to D constitute four output channels. Among these four channels, AC and BD are similar to the SCIs used previously, BC is the γ-insensitive channel, and AD is the channel most sensitive to γ. Momentum states are indicated above the lines. In the bottom are the temporal profiles of all the laser pulses. Bragg pulses have Gaussian temporal profiles. Bloch oscillations have trapezoid temporal profiles.

5.2 OSCI Geometry

For an atom interferometer where the atomic wave packets travel along the lower arm z_l and upper arm z_u, a vertical acceleration gradient γ will introduce a phase shift, to first order in γ, as

$$\Phi_\gamma = \frac{m\gamma}{2\hbar} \int \left(z_l^2 - z_u^2\right) dt = \frac{m\gamma A z_c}{\hbar}, \tag{5.1}$$

where m is the mass of the atom, $\hbar$ is the reduced Planck constant, $A = \int (z_l - z_u)\, dt$ is the space-time area enclosed between the two arms, and $z_c = \int (z_l^2 - z_u^2)\, dt / 2A$ is the center of this space-time area. For two simultaneous interferometers whose centers are separated by a vertical distance δz, the differential phase shift caused by γ is

$$\delta\Phi_\gamma = \frac{m\gamma A}{\hbar}\delta z. \tag{5.2}$$

This γ-related phase is an important systematic error source in many atom interferometer applications [61, 93, 75, 66]. Several schemes have been proposed to control this effect [17, 76, 23, 64]. For example, compensating the gravity gradient effect has been demonstrated in Raman-pulse Mach-Zehnder interferometers recently [23, 64]. The key idea in those experiments is to adjust the frequency of the central π pulse to compensate the phase shift produced by γ. However, so far these schemes require the gravity gradient to be measured, necessarily introducing a corresponding uncertainty. They also involve changing the frequency of the laser beams, which will complicate other systematic effects, such as diffraction phases.

OSCIs cancel the effect from acceleration gradients by spatially overlapping the centers of the two simultaneous interferometers, so that $\delta z = 0$ and $\delta\Phi_\gamma$ vanishes according to Equation 5.2. Not only does this technique not require a measurement of γ, it also works for both Bragg and Raman beam splitters, and can be applied to any atom interferometer geometry, even for the ones that are not intended for a gravity measurement, like Ramsey-Bordé interferometers.

Figure 5.1 shows the geometry of OSCIs. We first apply an nth order Bragg pulse, which transfers the momentum of $2n$ photons, and drives the atoms into a superposition of states $|0\rangle$ and $|n\rangle$. After time T_a, Bloch oscillations are applied to accelerate the upper arm to the state $|n + N_0\rangle$. A second deceleration Bloch oscillation sequence then brings this arm back to state $|n\rangle$. As the relative motion of these two arms comes from photon recoils, the displacement between them can be precisely controlled by the timing of these two Bloch oscillation beams. The initial Bragg pulse and the two Bloch oscillation sequences don't participate in interference. They are referred to as the offset-generating Bragg and Bloch beams henceforth. After another interval T_c, we initiate the normal SCI sequence: we apply a pair of nth order Bragg beam splitters, a sequence of N Bloch oscillations, and another pair of nth order Bragg beam splitters. Each pair of Bragg beam splitters has a separation time of T and the two pairs are separated by time T'. The second pair of Bragg beam splitters contains two frequencies, which are shifted by $\pm\omega_m$ relative to the first pair. These beams

are referred to as interferometer Bragg and Bloch beams. In the end, we have two sets of SCIs (the blue one and the red one) and four output ports (A to D), which constitute four output channels. Among these four channels, AC (a channel that outputs the differential phase between A and C) and BD are similar to the SCIs used previously. BC is the γ-insensitive channel, as B and C are spatially overlapped and can be used to cancel the γ effect. AD, AC, and BD are sensitive to γ, with AD having the largest sensitivity due to it having the largest displacement.

Required Offset for Cancelling γ

The offset-generating beams will offset the two SCIs by

$$\delta z = 2v_r(nT_i + N_0 T_b), \tag{5.3}$$

where $v_r = \hbar k / m_{\mathrm{Cs}}$ is the recoil velocity. Using Equation 5.2, this offset will cause a phase shift

$$\delta \Phi_\gamma = 8nT\omega_r \gamma (T + T')(nT_i + N_0 T_b) \tag{5.4}$$

where $\omega_r = mv_r^2/(2\hbar)$ is the recoil energy. T_i, T_b, T and T' are pulse-separation time defined in Figure 5.1. This phase shift has opposite signs on channel AD and BC.

The overall differential phase Φ_d from channel AC (or BD) is shown in Equation 4.1. Including the offset phase shift, the differential phase from every channel IJ ($IJ \in \{AC, BD, BC, AD\}$) now can be summarized as

$$\Phi_d = -2nT\left[\omega_m - 8\omega_r(n+N) - \omega_r \gamma C_{IJ}\right] + \Phi_{IJ}, \tag{5.5}$$

where Φ_{IJ} is the overall diffraction phase on every channel; C_{IJ} is the channel-dependent coefficient of the γ-related phase:

$$
\begin{aligned}
C_{BD} &= \frac{2}{3}n\left(2T^2 + 3TT' + 3T'^2\right) \\
&\quad + \frac{4}{3}N\left(T^2 + 3TT_2' + 3T_2'^2\right), \\
C_{AC} &= C_{BD}, \\
C_{AD} &= C_{BD} + 4\left(nT_i + N_0 T_b\right)\left(T + T'\right), \\
C_{BC} &= C_{BD} - 4\left(nT_i + N_0 T_b\right)\left(T + T'\right).
\end{aligned}
\tag{5.6}
$$

High order effects, including the phase terms that depend on the atom velocity, the duration of the Bloch beam, and the gravity acceleration g, are not shown for simplicity. By properly tuning the timing of the second offset-generating Bloch beam, we can zero C_{BC}, thus suppress the γ effect on channel BC. In the mean time, C_{AD} will be doubled, thus channel AD will have higher sensitivity to γ compared to AC and BD.

Suppressing the Diffraction Phase

The diffraction phase is suppressed in the γ-insensitive channel BC, which can be seen by examining the symmetries of OSCIs. After the offset-generating Bragg and Bloch beams, the upper SCI (the blue one) starts from the state $|n\rangle$, and the lower SCI (the red one) starts from the state $|0\rangle$. The two interferometers of channel BC now have a symmetric configuration compared to the regular SCI channel BD (or AC) where the two interferometers start from the same momentum state. This symmetry leads to the cancellation of the diffraction phase from the first two interferometer Bragg pulses. To show that, we follow the analysis in Reference [30, 65]. We use $\hat{B}_n$ to denote an nth order Bragg pulse. By numerically solving the optical Bloch equations that describe the process of Bragg diffraction [65], we obtain the matrix element $\langle b| \hat{B}_n |a\rangle$ as the complex amplitude for the Bragg pulse to drive an atom from state $|a\rangle$ into state $|b\rangle$. The diffraction phase from the beam splitter $\hat{B}_n$ is thus the argument $\arg(\langle b| \hat{B}_n |a\rangle)$,

Denote the diffraction phase from the mth interferometer Bragg pulse on output port I ($I \in \{A, B, C, D\}$) as $\Phi_{I,m}$. For A, the first interferometer Bragg pulse does not change the upper arm's state $|n\rangle$, but drives the lower arm from $|n\rangle$ to $|0\rangle$. Therefore, we have $\Phi_{A,1} = \arg(\langle n| \hat{B}_n |n\rangle / \langle n| \hat{B}_n |0\rangle)$. Similarly,

$$
\begin{aligned}
\Phi_{A,1} &= \Phi_{A,2} = \Phi_{B,2} = \Phi_{C,1} = \arg\left(\frac{\langle n| \hat{B}_n |n\rangle}{\langle n| \hat{B}_n |0\rangle} \right), \\
\Phi_{B,1} &= \Phi_{C,2} = \Phi_{D,1} = \Phi_{D,2} = \arg\left(\frac{\langle n| \hat{B}_n |0\rangle}{\langle 0| \hat{B}_n |0\rangle} \right).
\end{aligned}
\tag{5.7}
$$

For every channel IJ, the diffraction phase from the mth interferometer Bragg pulse, denoted as $\Phi_{IJ,m}$, is $\Phi_{I,m} - \Phi_{J,m}$. Using Equation 5.7,

$$
\begin{aligned}
\Phi_{AC,1} &= \Phi_{BD,1} = 0, \\
\Phi_{AD,1} &= -\Phi_{BC,1} = \Phi_{AC,2} = \Phi_{BD,2} = \Phi_{AD,2} \\
&= \Phi_{BC,2} = \arg\left(\frac{\langle 0| \hat{B}_n |0\rangle \langle n| \hat{B}_n |n\rangle}{\langle n| \hat{B}_n |0\rangle^2} \right).
\end{aligned}
\tag{5.8}
$$

Because $\Phi_{AC,1} = \Phi_{BD,1} = 0$, the diffraction phase from the first two Bragg pulses is zero in channels AC and BD, the main contribution comes from the second one; in the γ-insensitive channel BC, the diffraction phases from the first two interferometer Bragg pulses cancel each other because $\Phi_{BC,1} = -\Phi_{BC,2}$; conversely, in channel AD, the first two interferometer Bragg pulses introduce the same diffraction phase. Similar analysis shows that the diffraction phase from the third and fourth interferometer Bragg pulses is the same in all channels. Therefore, the overall diffraction phase is suppressed in channel BC and amplified in channel AD relative to channel AC and BD.

5.3 Experiment

We prepare the atom cloud with the steps introduced in Chapter 3. Similar to the α measurement, we use 5$^{\text{th}}$ order Bragg pulses ($n = 5$), and 125 Bloch oscillations ($N_0 = N = 125$) for offset-generating and interferometer. All the Bragg and Bloch beams are 14 GHz blue-detuned from the cesium $F = 3 \rightarrow F' = 4$ D$_2$ transition. The intensity of the offset-generating Bragg pulse is set so that output port A and B have roughly the same signal amplitude. The intensities of the two offset-generating Bloch oscillation beams are optimized to the highest efficiency. The frequencies of the offset-generating Bloch beams are generated in the same way as the interferometer Bloch beams. So the down-propagating beams contain a pair of frequencies. For them to only interact with the atoms in the momentum state $|n\rangle$, the frequencies of both counter-propagating beams are decreased by 20 kHz: $\omega_2 - \omega_2' = \omega_1 - \omega_1' = 2\pi \times 20$ kHz. Atoms left behind by the acceleration Bloch oscillations are mostly in the $|n\rangle$ state and would spatially overlap with the signals. To suppress these atoms, we apply a velocity selection Raman pulse to drive the atoms with $2n\hbar k$ momentum from the $F = 3$ ground state to the $F = 4$ ground state, and then apply a resonant beam to blow away the atoms in the $F = 4$ state. These pulses are not shown in Figure 5.1. Atoms left behind by the deceleration Bloch oscillations are in the $|n + N_0\rangle$ momentum state. They are spatially resolved from the output channels, thus will not affect the experiment.

We fix the timing of the offset-generating Bragg pulse, the acceleration offset-generating Bloch oscillations, the second and the third interferometer Bragg pulses relative to the experiment sequence: $T_a = 5$ ms, $T_i + T = 155$ ms, $T' = 50$ ms and $T_2' = 45$ ms. When T changes, we adjust T_b according to Equation 5.6, so that $C_{BC} = 0$. This guarantees channel BC has no sensitivity to γ.

5.4 Statistical Sensitivity

First we demonstrate the statistical sensitivity of OSCIs. We set T to 10 ms. T_b is calculated to be 37.6 ms from Equation 5.6. This results in an offset of about 3.2 cm between the two wave packets at the moment of the first interferometer Bragg pulse. Figure 5.2 shows the typical fluorescence signal we observe. The eight peaks on the two sides correspond to four output ports. The two peaks in the middle come from the atoms that are not driven by the interferometer Bloch oscillations. These atoms do not contribute to the measurement.

Similar to the α measurement, we use ellipse fitting to extract the differential phase between two output ports. The ellipses are shown in Figure 5.3. The x axis of each ellipse is the normalized signal of the lower interferometer (C or D), and the y axis is the normalized signal of the upper interferometer (A or B). The γ-insensitive channel BC has the same x contrast as channel AC (about 16%), and the same y contrast as channel BD (about 22%), demonstrating that introducing an offset doesn't lead to decoherence. After 13 hours of integration, we reach an uncertainty of about 3 part-per-billion (ppb) in the differential phase for every channel, which corresponds to 1.5 ppb statistical uncertainty in α [66]. This

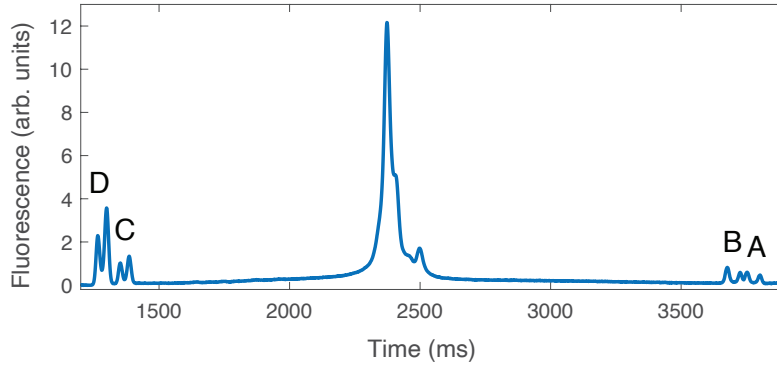demonstrates the world-class sensitivity of OSCIs.

Figure 5.2: Fluorescence trace taken at $T = 10$ ms and $T_b = 37.6$ ms. It is an average of 30 measurements. The eight peaks on the two sides correspond to four output ports. The two big peaks in the middle are the atoms not driven by Bloch oscillations, which do not contribute to the measurement.
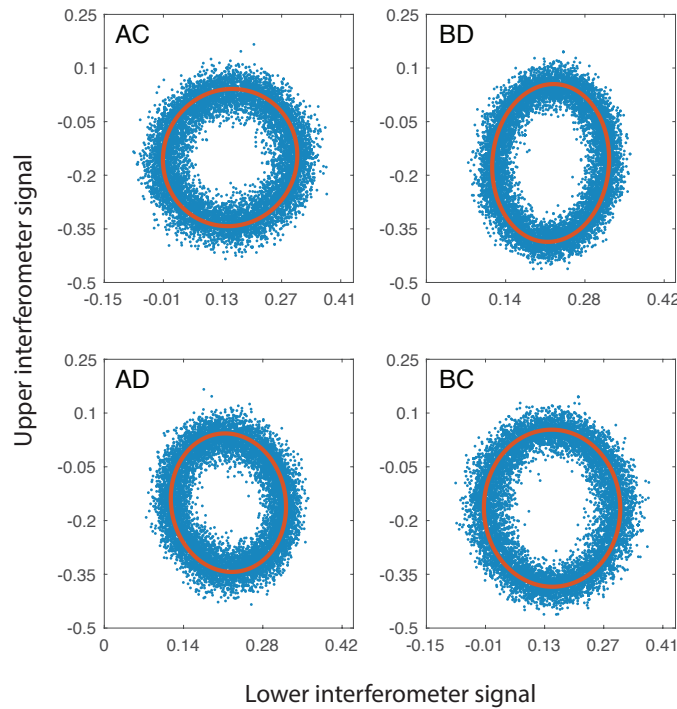

Figure 5.3: Ellipse observed from every channel at $T = 10$ ms and $T_b = 37.6$ ms. Data was collected over a period of 13 hours. The red curve is the fitted ellipse from every channel.
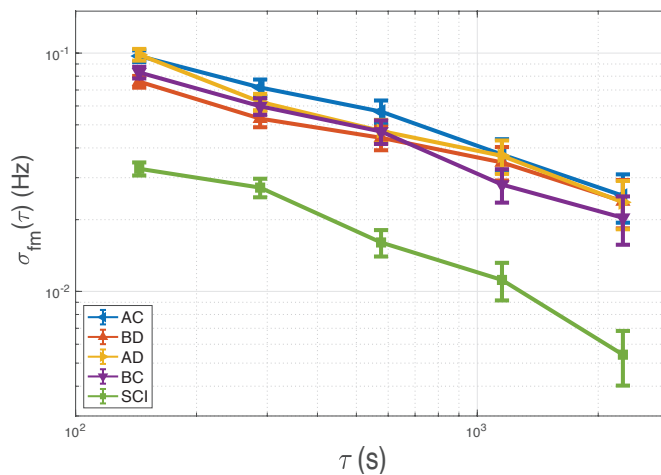
Figure 5.4: Allan deviation of the measured frequency at $T = 10$ ms for every OSCI channel. As a comparison, the Allan deviation for the SCI geometry with the same interferometer timing sequence is also plotted.
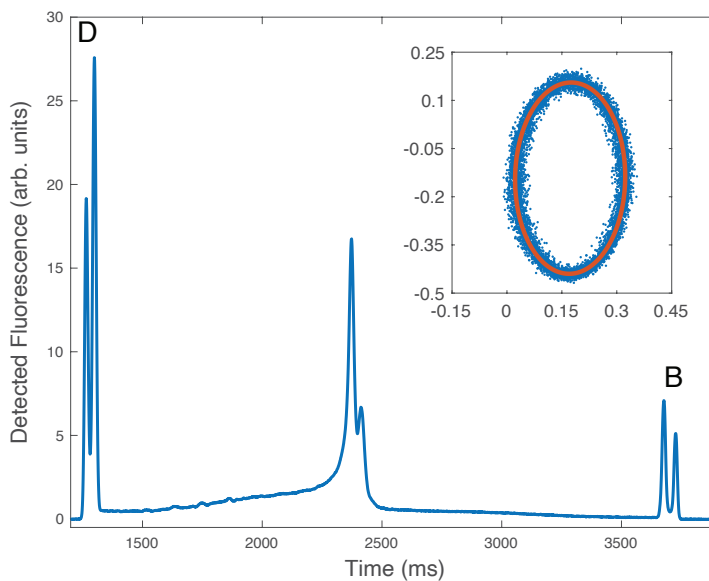

Figure 5.5: Fluorescence and ellipses from SCI configuration.

Figure 5.4 shows the Allan deviation of the measured frequency for every OSCI channel. The sensitivities of all channels are about the same, roughly at 1.1 Hz/$\sqrt{\text{Hz}}$. As a comparison, we remove the offset-generating beams and leave the interferometer beam sequence unchanged. This leads to a regular SCI geometry. The Allan deviation for this SCI geometry is also plotted, showing a sensitivity of 0.38 Hz/$\sqrt{\text{Hz}}$. The sensitivity of every OSCI channel is reduced by only a factor of 3 compared to the SCI geometry.

This reduction in sensitivity is mainly due to the low signal-to-noise ratio of OSCIs. It can be explained from two aspects. First, OSCIs distribute the atom population on four output ports. This reduce the effective signal size on each channel. Second, single-photon scattering and tunnelling loss introduced by the two offset-generating Bloch oscillation sequences further lowers the total signal size. Figure 5.5 shows the signal and ellipse we observe from the SCI geometry. Note that Figure 5.2 and Figure 5.5 have the same unit in the y axis. The signal in the SCI geometry is about ten times larger that the signals of OSCIs.

Increasing the detuning of the laser pulses to suppress single photon scattering, and using broader laser beams to drive Bragg diffraction and Bloch oscillations (so the intensity is more uniform across the atomic sample), is expected to improve the signal-to-noise ratio, thus benefit the sensitivity.

5.5 Consistent Output and Suppression of Diffraction Phase

Next, we show the consistency of the recoil frequency from every channel and the suppression of the diffraction phase. We vary the pulse separation time T from 5 ms to 20 ms, and adjust T_b accordingly. At each T, we adjust ω_m to the point where the total phase Φ is zero. Define the measured frequency as $f_m = \omega_m/(2\pi)$. According to Equation 5.5 and Equation 5.6, f_m can be fitted as a function of $1/T$ with two fitting parameters, the diffraction phase and the recoil frequency $f_r = \omega_r/(2\pi)$,

$$f_m = \frac{\Phi_{IJ}}{4n\pi T} + [8(n+N) + \gamma \times C_{IJ}] f_r. \tag{5.9}$$

Figure 5.6(a) shows the measurement results and the corresponding fittings. At short Ts, the contribution from the gravity gradient is small. f_m is roughly linear in $1/T$, with a slope proportional to the diffraction phase. The coefficients C_{IJ} scale with T^2. As T increases, the effect from the gravity gradient becomes more pronounced, thus the fitting curve is no longer linear. This represents a potentially large systemic effect in the α measurement. For instance, at $T = 80$ ms, the gravity gradient will shift the total phase in channel BD by 8 ppb, which is over two orders of magnitude larger than the required accuracy of the recoil frequency. By properly setting the timing, sensitivity to γ in channel BC is cancelled. The fitting for this channel is a straight line.

Figure 5.6(b) shows the fitted recoil frequency from all channels. They agree with each other within 1σ uncertainty, demonstrating the consistency of the output from every channel.

Fig. 5.6(c) shows the fitted diffraction phase from all channels: $\Phi_{AC} = 22 \pm 6$ mrad, $\Phi_{BD} = 41 \pm 3$ mrad, $\Phi_{AD} = 70 \pm 4$ mrad and $\Phi_{BC} = -7 \pm 5$ mrad. The diffraction phase is suppressed by a factor of 6 in channel BC compared to channel BD, and a factor of 10 compared to channel AD.

We also run Monte Carlo simulations to confirm the suppression of diffraction phase. The simulation is upgraded from the version which we used in the α measurement. It includes Bloch oscillations according to Reference [21, 48]. It predicts that the diffraction phase in channel BC is 3 times smaller than that in channel BD, and 6 times smaller than that in channel AD. It also predicts that channel AC and BD have roughly the same diffraction phase. While these results agree with experiments qualitatively, we attribute the discrepancy to features that are not included in the simulation, such as beam divergence and the different velocity distribution of the wave-packets in the two SCIs.

5.6   Discussion and Conclusions

A measurement of α using atom interferometers has two leading systematic error sources: acceleration gradients and non-Gaussian wavefronts, as shown in Table 4.2. With this new OSCI scheme, the uncertainty from the acceleration gradient will now be negligible. The effects from non-Gaussian wavefronts can be suppressed by driving Bragg diffraction and Bloch oscillations with larger-width laser beams, which as mentioned above also improves the sensitivity.

The ability to control the offset in OSCIs also enables new ways to check many systematic effects. For example, with the increased vertical separation between A and D, OSCIs can measure γ using channel AD; Comparing the results from Channel AC and BD allows us to identify and reduce effects such as the inhomogeneous magnetic field along the vertical direction, the divergence of the laser beams, and the stray light reflected by the vacuum chamber; Because these two channels have the same phase produced by gravity gradient, a comparison between them will also place a bound on third order gravity variation (the gradient of the gravity gradient). These systematic checks can be done simultaneously with data taken for a measurement of the recoil frequency.

The OSCI geometry can also be generalized for isotope mass ratio measurements [50]. With sensitive to the mass of atoms and immunity to gravity gradients, OSCIs provides a compelling scheme for precision mass ratio measurements with matter-wave interferometers.
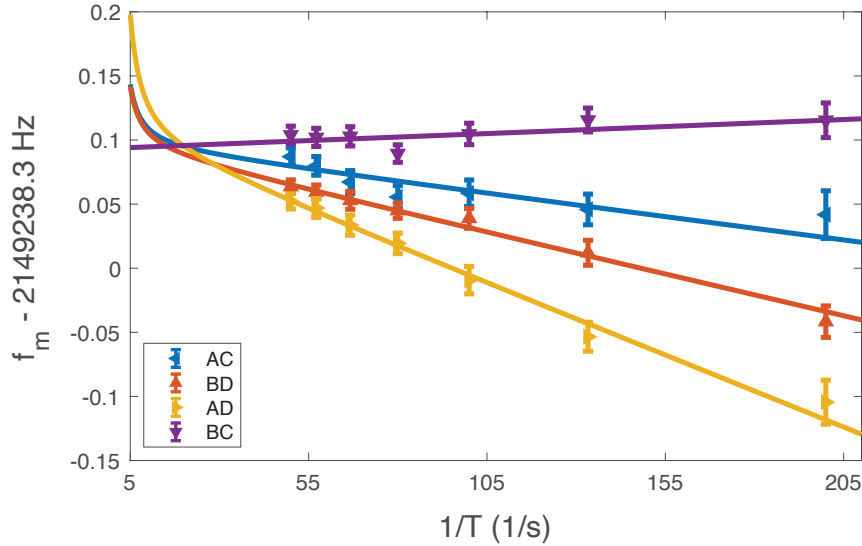
Figure 5.6: Measured frequency vs. $1/T$. The data points are from experimental measurements and curves are corresponding fittings using the functional form of Equation 5.9. The γ value comes from Ref. [66]. Channel BC has no γ effect, the fitting is a straight line. Data was taken over two successive days.
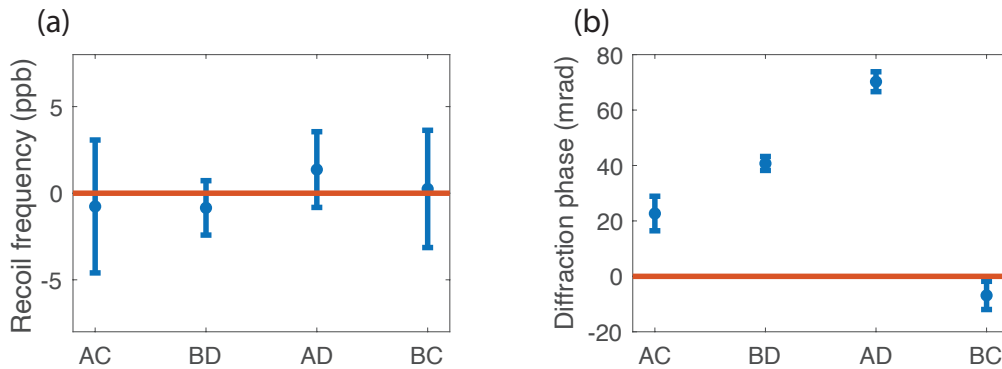

Figure 5.7: (a) Fitted recoil frequencies in all channels. They are consistent within in 1σ uncertainty. The red line is the average of these frequencies. (b) Fitted diffraction phases from all channels. The red line indicates zero. A 6-fold suppression of the diffraction phase in channel BC was observed compared to channel BD.

Chapter 6

Summary and New Experiment

6.1 Summary of the α Measurement

We have recorded the most accurate measurement of the fine structure constant $\alpha = 1/137.035999046(27)$ at an accuracy of 0.20 ppb via measuring h/m_{Cs}, the quotient of the Planck constant and the mass of a cesium atom. Our tools are simultaneous conjugate Ramsey-Bordé atom interferometers based on a cesium atomic fountain. Using Bragg diffraction and Bloch oscillations, we have demonstrated the largest phase (12 million radians) of any Ramsey-Bordé interferometer and controlled the systematic effects at a level of 0.12 ppb. Using our result, the Standard Model prediction of the electron gyromagnetic moment anomaly a_e has reached an uncertainty of 0.20 ppb, slightly better than its experimental measurement using Penning traps (0.24 ppb), see Figure 1.2. However, there is a 2.5σ tension between the prediction and the measurement of a_e. The tension motivates an improved measurement of α.

6.2 Motivation for an Improved Measurement

An improved measurement of the fine structure constant α will enable detecting new physics within the Standard Model. Currently the experimental measurement and the Standard Model prediction of a_e have reached the same level of accuracy. The accuracy of the Standard Model prediction is limited by the accuracy of α. If both measurement accuracies of α and a_e can be improved by an order of magnitude, we will be able to resolve the contributions from the weak interaction or even QED for tauon to the predicted a_e for the first time.

An improved measurement of α will also be a powerful probe for new physics beyond the Standard Model. The observed 2.5σ tension between the measured and predicted a_e provides hints of new physics beyond the Standard Model, such as dark photons and dark axial-vector bosons. Improved measurements of α and a_e will help resolve this tension.

The 2.5σ tension could be a potential sign of new physics that mirrors the well-known 3.7σ discrepancy observed in the muon's gyromagnetic moment anomaly a_μ [14, 57]. If the

discrepancy in a_μ is a caused by new physics beyond the Standard Model, it is expected to show up in a_e, scaled by the squared particle mass ratio at ~ 50 ppt. The two unexplained discrepancies combine to an overall 4.6σ deviation from the Standard Model for lepton magnetic moments[1]. This has given rise to a great deal of theoretical work. Theories that can explain both anomalies are arising [24, 22]. It also suggests that improved measurements of a_μ, a_e and α are in need. a_μ is currently being remeasured by E989 at Fermilab, which expects to reduce the error more than threefold [42]. Prof. Gerald Gabrielse is currently remeasuring a_e and expects an improvement by an order of magnitude to 20 ppt [36]. Improved measurement of α therefore is of great importance.

Currently we are building a new experiment, aiming to reduce the uncertainty of h/m_{Cs} to 15 ppt. This would be a 30-fold improvement relative to our previous measurement. Without improvements in the accuracies of cesium and electron masses, the uncertainty in α will be improved to 45 ppt. There is an anticipated improved measurement of the cesium mass with an accuracy of 10 ppt instead of 70 ppt [15]. This will further improve the accuracy of α to 20 ppt. We hope the ongoing improvements in h/m_{At} measurements will motivate a 2-5 fold improvement in the knowledge of the electron mass. With all the efforts, the accuracy of α will finally reach 10 ppt. In the following sections, we will talk about the upgrades we are currently working on or plan to implement in the near future to achieve the goal.

6.3 Vacuum Chamber

Figure 6.1 shows the vacuum chamber that we plan to use for the next-generation α measurement. The experiment will take place in an acoustically and electromagnetically shielded room, to shield against air currents, background magnetic fields and acoustics. It also helps maintain a constant temperature. The vacuum chamber is about 4.5 m long and weighs more than 1600 lb. It has an inner radius around 28 cm. The chamber is designed to be over-sized so that we can use a large-radius laser beam. This also avoids stray reflections of the laser beams at wall.

The chamber will be mounted using a hexapod style mechanical connection, with six support struts providing exact constraint in all six degrees of freedom. The three bipods composing the hexapod would connect to the optical table via three vibration isolation units. An example is the stages provided by Minus-K, which have been successfully used in previous interferometers. Theoretically vibration is cancelled by the interferometry geometry, but a low-vibration environment will help us to maintain the stability of the delicate beam alignment. It will also help us to run the atom interferometer in gravimeter mode, demonstrating new atom interferometer technologies. It may also be used in possible follow-up projects to detect dark matter.

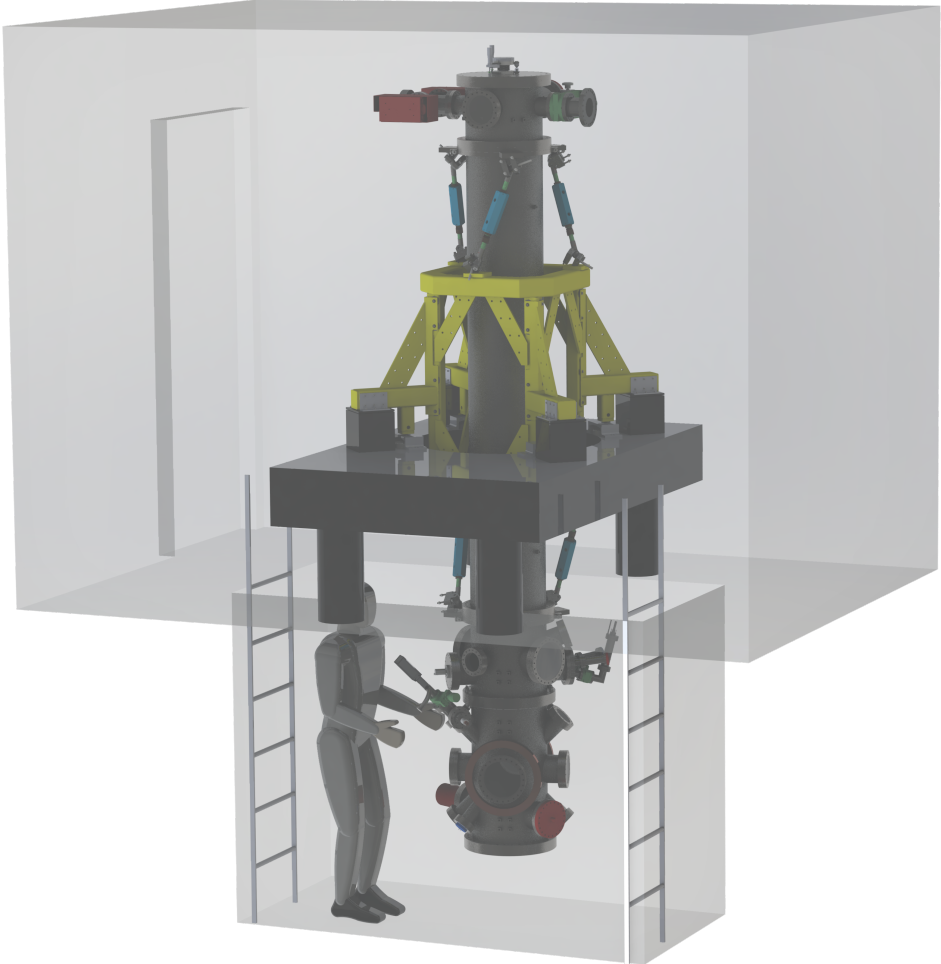[1]http://resonaances.blogspot.com/2018/06/alpha-and-g-minus-two.html

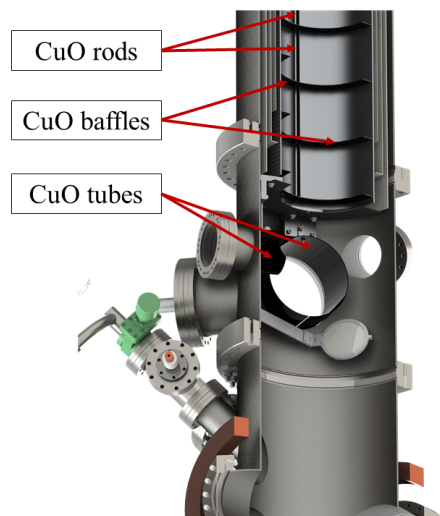Figure 6.1: Vacuum chamber for the new experiment.
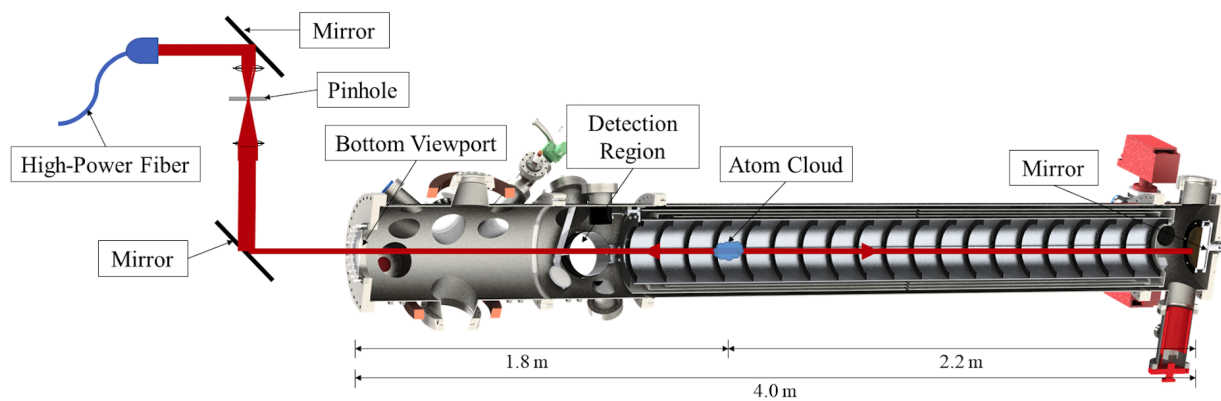
Figure 6.2: Cross section of the detection region.

Figure 6.3: Cross-section of the vacuum chamber including the high-power fiber and the pinhole fiber. In this drawing the vertical direction points to the right.

Figure 6.4 shows the cross section of the new vacuum chamber. Similar to the chamber used for the previous measurement, the new chamber consists of three parts: a MOT chamber, a detection chamber, and a tube where interferometry happens (see Section 3.1). Inside the interferometer tube are three layers of μ-metal magnetic shields, providing a shielding factor of 10000. Inside the magnetic shields is a solenoid that generates the magnetic field along the vertical direction to define the quantum axis for the atoms. To further suppress the stray reflection at the wall, we will install 20 black copper oxide ring baffles inside the solenoid. The baffles have an inner diameter of 21.64 cm and an outer diameter of 27.01 cm. They are prepared in a procedure similar to the reference [62]. They have been tested to be UHV compatible. We will also install copper oxide tube at the detection window to suppress the random light that would hit the detector and lower the signal-to-noise ratio, as shown in Figure 6.2.

6.4   High-power Laser System

As shown in Table 4.2, the non-Gaussian wavefront of the laser beam is one of the dominant error sources in this experiment. The effects scale with $(\lambda/w_0)^2$ (the squared ratio of the wavelength and the beam radius, which determines the flatness of the wave fronts) or $(r_c/w_0)^2$ (the squared ratio of the atomic sample radius and the beam radius, which determines intensity variations across the sample) [65, 66]. The new experiment will take the control over the laser wavefronts to the extreme by performing atom interferometry with a large-radius beam, $w_0 \approx 25$ mm waist, compared with the previous waist of 3 mm. This will suppress the leading systematic effects by almost two orders of magnitude.

To generate sufficient intensity, we are building a high-power laser system, as shown in Figure 6.5. The Nd:YAG seed laser outputs 500 mW continuous laser light at the wavelength of 1064 nm. One pre-amplifier and two main amplifiers are powered in pulse mode and will shape the laser beam into $100\,\mu$s-pulses. Every pulse will have more than 1 J energy, corresponding to more than 10 kW power. The amplifiers are from Northrop-Grumman Cutting Edge Optronics. An LBO second harmonic generator (SHG) will then convert the wavelength of the pulses to 532 nm. This has already been demonstrated by Prof. Dave DeMille from Yale, where more than 0.4 J at 532 nm has been observed. The 532 nm pulses will then be used to pump an optical parametric amplifier (OPA) which amplifies the 852 nm seed light. The seed beam will come from the MSquared laser used for the previous experiments. Each resulting 852 nm pulse from the OPA is expected to have a peak power of more than 300 W (30 mJ for a $100\,\mu$s-pulse).

The high-power $100\,\mu$s-pulses will be used for Bragg diffraction in the new experiment. The Bloch oscillation pulses, however, are substantially longer (15 ms). This will require different optimizations of the SHG and OPA. This upgrade is currently being studied. We will be likely to use two groups of SHG and OPA crystals, one for Bragg and one for Bloch, selected by acousto-optical modulators.

Figure 6.3 shows how the high-power laser pulses are delieved to the atoms. Single-mode
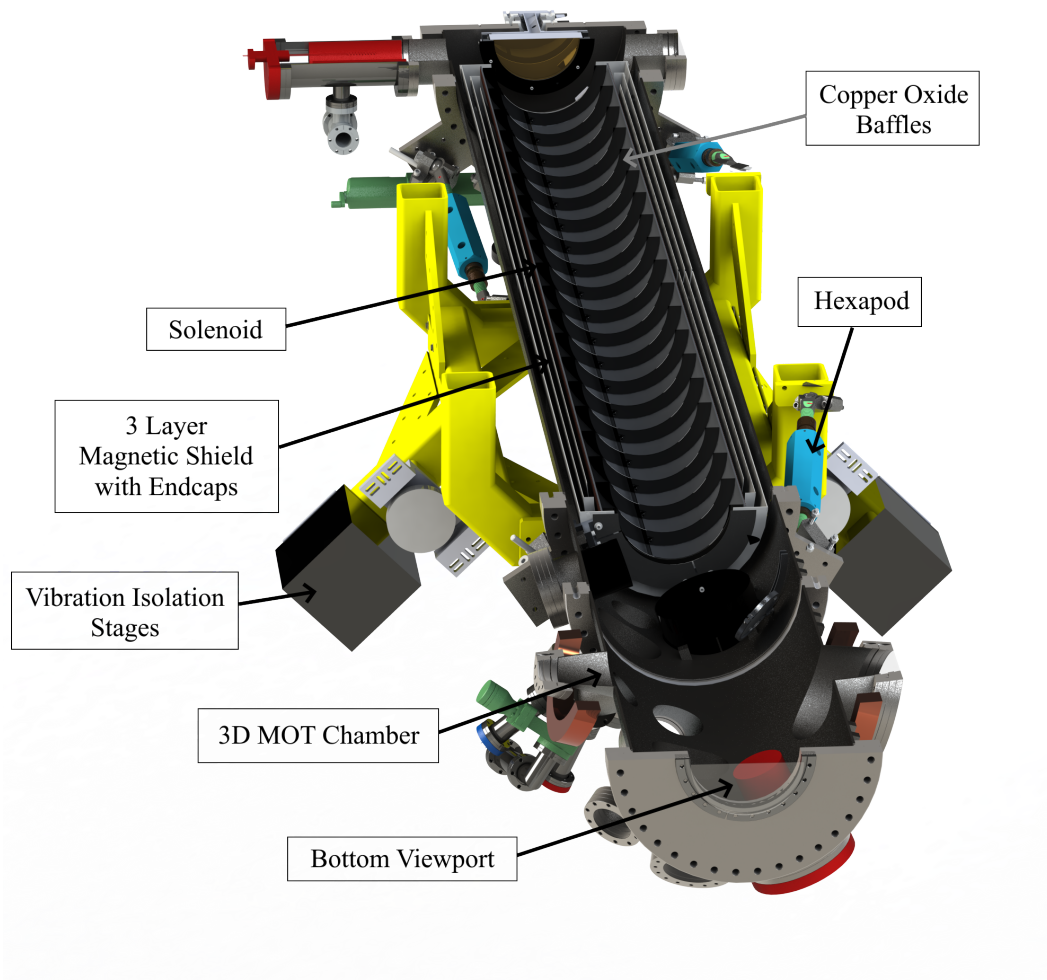
Figure 6.4: Cross section of the new vacuum chamber.

optical fibers have been used for beam delivery in the previous measurement. They provide mode-filtering and independence of the alignment of the physics system from the alignment of the laser. The main limiting factors for high-power operation of the fiber are the thresholds for nonlinear scattering, such as the stimulated Raman scattering (SRS) and the stimulated Brillouin scattering (SBS) [2]. Hollow-core fibers will be used in the new experiment. In a hollow-core fiber, only about 5% of the energy is in silica, while the rest is in air [43].

The mode shape from a hollow-core fiber is non-ideal due to the photonic crystal structure. There will also be distortions in the wavefronts due to non-perfection of the optics. To improve the small-scale structure of the laser beam, we will use a pin-hole filter, shown in Figure 6.3. The laser beam is focused through a pinhole. The intensity distribution in the focal plane is a two-dimensional Fourier transform of the input beam; thus, small-scale intensity fluctuations cause off-axis components are blocked by the pinhole. After collimating the beam, we will obtain a clean beam with a smooth intensity profile [71].
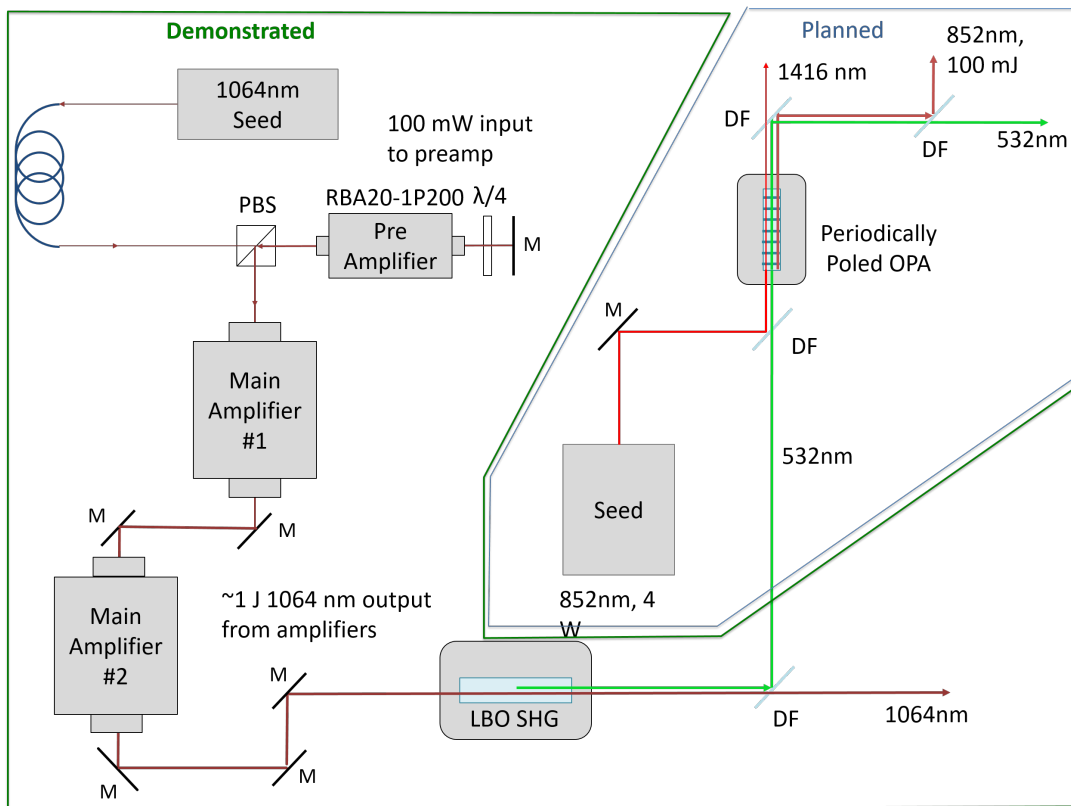

Figure 6.5: High-power laser system. The 532 nm pulsed power source has been shown to deliver more than 0.4 J at 532 nm at Yale. The planned OPA is conservatively designed for 0.1 J energy (and thus 1 kW power) in 100 μs pulses, but may deliver up to 0.3 J/ 3kW.

6.5 Gravity Gradient

Another main systematic source is the gravity gradient. The OSCI configuration will be used for the new measurement. We have demonstrated this method and verified the cancellation of the gravity gradient using the setup for the previous measurement of α, as discussed in Chapter 5. The influence of gravity is now limited to higher-order gradients (third and higher order derivatives of the gravitational potential). These effects come from the different mass distributions around the two simultaneous interferometers. In the new experiment, they are mainly from the gravity change caused by the pit and the optical table. The new vacuum chamber has been designed in a way such that interferometry happens when the atoms are well above the optical table. For the old setup, higher order gravity effects have been estimated to be 5 ppt (see Section 4.5). With an improvement by controlling the gravitational environment of the new experiment, this systematic effect will be suppressed to 3 ppt.

6.6 Other Upgrades

Detection with a CMOS Camera

In the previous experiment, atoms have been detected via fluorescence detection with a silicon photodiode. While this makes it easier for timing sequence control, detecting with a photodiode lacks spatial resolution. As a result, the experiment had to be repeated several times to study the dependence of the measurement on which part of the atom cloud is detected. In the new experiment, we will use a CMOS camera to detect the fluorescence. The recorded image will not only be used for extracting the interference signal, but can also provide the spatial resolution for future systematic checks.

Launch with Bloch Oscillations

In the previous experiment, the atom cloud was lunched with moving molasses. The launch direction depends on the power balance and the polarizations of the molasses beams. If the power of the molasses beams change due to misalignment of the fibers, or the polarizations drift due to temperature change in the lab, the launch direction will drift, lowing the final signal size and introducing systematic effects. Therefore, tremendous effort has been spent in babysitting the system during data collection. We even had to realign the fountain from scratch several times when it misaligned too much. In the new experiment, we plan to launch the atom cloud with Bloch oscillations. This is expected to make the system more robust and therefore facilitate the data collection.

Linearly Polarized Laser Pulses

For the previous experiment, the state and velocity selection Raman pulses as well as the Bragg and Bloch pulses are circularly polarized. That was achieved using two quarter waveplates, one at bottom of the vacuum chamber and one at the top. These waveplates will inevitably cause wavefront distortions. In the new experiment, we plan to use linearly polarized pulses to avoid the waveplates. Since Raman transition and Bragg diffraction require different polarization configurations for linearly polarized pulses (lin⊥lin for Raman and lin∥lin for Bragg [95]), extra efforts will be needed to make it happen.

Independent Laser for Bloch Oscillations

For simplicity, we have so far used the same laser source for both Bragg diffraction and Bloch oscillations. In order to suppress decoherence due to single-photon scattering, Bloch oscillations have to be operated at high single photon detuning (typically blue detuned by 14 GHz or more). But Bragg diffraction doesn't require such a large detuning. In order to unleash potential for both Bragg diffraction and Bloch oscillations, we will use a separate laser source to generate the Bloch-oscillation light, as mentioned in Section 6.4. With this scheme, we could increase the single photon detuning for Bloch oscillations even further to suppress single photon scattering. And given the power capacity limited by the laser, running at a smaller detuning will enable us to expand Bragg beam size further or increase momentum transfer for each individual Bragg beam splitter.

6.7   Expected Sensitivity

We expect a 5-fold increase in atom number, as the thick beam will allow us to use the entire sample. Using a thick beam with a more uniform wavefront and an increased single photon detuning for the Bloch oscillations will also help overcome the loss and decoherence mechanisms mentioned in Section 4.4. We therefore expect to increase the pulse separation time T to 500 ms. Scaling the current statistical sensitivity of $0.2\,\mathrm{ppb}$ in a day by $80\,\mathrm{ms}/500\,\mathrm{ms}$ for the increased pulse separation time, by $1/2$ for the increased diffraction order, by $1/\sqrt{5}$ for the increased atom number, and down by $\sqrt{3/2}$ for the increased cycle time, we anticipate a statistical error of 0.008 ppb in α in a day.

Bibliography

[1]   S. Adler and *et al.* "Further Evidence for the Decay $K^+ \to \pi^+ \nu \bar{\nu}$". In: *Phys. Rev. Lett.* 88 (4 2002), p. 041803.

[2]   Govind Agrawal. *Nonlinear Optics*. 4th ed. Academic Press, 2006.

[3]   Tatsumi Aoyama et al. "Erratum: Tenth-order electron anomalous magnetic moment: Contribution of diagrams without closed lepton loops [Phys. Rev. D 91, 033006 (2015)]". In: *Phys. Rev. D* 96 (2017), p. 019901.

[4]   Tatsumi Aoyama et al. "Tenth-order electron anomalous magnetic moment: Contribution of diagrams without closed lepton loops". In: *Phys. Rev. D* 91 (2015), p. 033006.

[5]   Tatsumi Aoyama et al. "Tenth-Order QED Contribution to the Electron $g-2$ and an Improved Value of the Fine Structure Constant". In: *Phys. Rev. Lett.* 109 (2012), p. 111807.

[6]   A. V. Artamonov and *et al.* "Study of the decay $K^+ \to \pi^+ \nu \bar{\nu}$ in the momentum region $140 < P_\pi < 199$ MeV/c". In: *Phys. Rev. D* 79 (9 2009), p. 092004.

[7]   "Atomic interferometry with internal state labelling". In: *Physics Letters A* 140.1 (1989), pp. 10–12. ISSN: 0375-9601.

[8]   G. Audi et al. "The Nubase2012 evaluation of nuclear properties". In: *Chinese Physics C* 36.12 (2012), p. 1157.

[9]   S. Bade et al. "Photon momentum in a distorted optical field". In: *ArXiv e-prints 1712.04023* (2017).

[10] Satyanarayana Bade et al. "Observation of Extra Photon Recoil in a Distorted Optical Field". In: *Phys. Rev. Lett.* 121 (7 Aug. 2018), p. 073603.

[11] D. Banerjee and *et al.* "Search for Invisible Decays of Sub-GeV Dark Photons in Missing-Energy Events at the CERN SPS". In: *Phys. Rev. Lett.* 118 (2017), p. 011802.

[12] D. Banerjee and *et al.* "Search for vector mediator of dark matter production in invisible decay mode". In: *Phys. Rev. D* 97 (2018), p. 072002.

[13] Maxime Ben Dahan et al. "Bloch Oscillations of Atoms in an Optical Potential". In: *Phys. Rev. Lett.* 76 (24 June 1996), pp. 4508–4511.

[14] G. W. Bennett et al. "Final report of the E821 muon anomalous magnetic moment measurement at BNL". In: *Phys. Rev. D* 73 (7 Apr. 2006), p. 072003.

[15] Klaus Blaum. "High-accuracy mass spectrometry with stored ions". In: *Physics Reports* 425.1 (2006), pp. 1–78.

[16] Rym Bouchendira et al. "New Determination of the Fine Structure Constant and Test of the Quantum Electrodynamics". In: *Phys. Rev. Lett.* 106 (8 Feb. 2011), p. 080801.

[17] Sheng-wey Chiow et al. "Gravity-gradient suppression in spaceborne atomic tests of the equivalence principle". In: *Phys. Rev. A* 95 (2 Feb. 2017), p. 021603.

[18] Sheng-wey Chiow et al. "Noise-Immune Conjugate Large-Area Atom Interferometers". In: *Phys. Rev. Lett.* 103 (2009), p. 050402.

[19] Pierre Cladé. "Bloch oscillations in atom interferometry". In: *arXiv:1405.2770* ().

[20] Pierre Cladé et al. "Precise measurement of h/m_{Rb} using Bloch oscillations in a vertical optical lattice: Determination of the fine-structure constant". In: *Phys. Rev. A* 74 (2006), p. 052109.

[21] Pierre Cladé et al. "Theoretical analysis of a large momentum beamsplitter using Bloch oscillations". In: *Eur. Phys. J. D* 59 (3 2010), pp. 349–360.

[22] A. Crivellin, M. Hoferichter, and P. Schmidt-Wellenburg. "Combined explanations of $(g - 2)_{-}\mu, e$ and implications for a large muon EDM". In: *ArXiv e-prints 1807.11484* (2018).

[23] G. D'Amico et al. "Canceling the Gravity Gradient Phase Shift in Atom Interferometry". In: *Phys. Rev. Lett.* 119 (25 Dec. 2017), p. 253201.

[24] H. Davoudiasl and W. J. Marciano. "A Tale of Two Anomalies". In: *ArXiv e-prints 1806.10252* (2018).

[25] Hooman Davoudiasl, Hye-Sung Lee, and William J. Marciano. "Muon $g - 2$, rare kaon decays, and parity violation from dark bosons". In: *Phys. Rev. D* 89 (2014), p. 095006.

[26] Xiao-Chun Duan et al. "Test of the Universality of Free Fall with Atoms in Different Spin Orientations". In: *Phys. Rev. Lett.* 117 (2 July 2016), p. 023001.

[27] I. Dutta et al. "Continuous Cold-Atom Inertial Sensor with 1 nrad/sec Rotation Stability". In: *Phys. Rev. Lett.* 116 (18 May 2016), p. 183003.

[28] Benjamin Elder et al. "Chameleon dark energy and atom interferometry". In: *Phys. Rev. D* 94 (4 Aug. 2016), p. 044051.

[29] Brian Estey. "Precision Measurement in Atom Interferometry Using Bragg Diffraction". PhD thesis. University of California, Berkeley, 2016.

[30] Brian Estey et al. "High-Resolution Atom Interferometers with Suppressed Diffraction Phases". In: *Phys. Rev. Lett.* 115 (8 Aug. 2015), p. 083002.

[31] A. Fitzgibbon, M. Pilu, and R. B. Fisher. "Direct least square fitting of ellipses". In: *IEEE Transactions on Pattern Analysis and Machine Intelligence* 21.5 (May 1999), pp. 476–480.

[32] J. B. Fixler et al. "Atom Interferometer Measurement of the Newtonian Constant of Gravity". In: *Science* 315.5808 (2007), pp. 74–77.

[33] G. T. Foster et al. "Method of phase extraction between coupled atom interferometers using ellipse-specific fitting". In: *Opt. Lett.* 27.11 (June 2002), pp. 951–953.

[34] Sebastian Fray et al. "Atomic Interferometer with Amplitude Gratings of Light and Its Applications to Atom Based Tests of the Equivalence Principle". In: *Phys. Rev. Lett.* 93 (24 Dec. 2004), p. 240404.

[35] G. Gabrielse et al. "Fundamental Physics in Particle Traps, W. Quint, M. Vogel, Eds." In: *Springer Tracts in Modern Physics Series* 256 (2014).

[36] G. Gabrielse et al. *Towards an Improved Test of the Standard Model's Most Precise Prediction*. 2019. arXiv: `1904.06174 [quant-ph]`.

[37] R. Geiger et al. "Detecting inertial effects with airborne matter-wave interferometry". In: *Nature Communications* 2 (2011), p. 474.

[38] P. Hamilton et al. "Atom-interferometry constraints on dark energy". In: *Science* 349.6250 (2015), pp. 849–851.

[39] D. Hanneke, S. Fogwell, and G. Gabrielse. "New Measurement of the Electron Magnetic Moment and the Fine Structure Constant". In: *Phys. Rev. Lett.* 100 (12 Mar. 2008), p. 120801.

[40] Philipp Haslinger et al. "Attractive force on atoms due to blackbody radiation". In: *Nature Physics* 14 (2018), pp. 257–260.

[41] Jason M. Hogan and Mark A. Kasevich. "Atom-interferometric gravitational-wave detection using heterodyne laser links". In: *Phys. Rev. A* 94 (3 Sept. 2016), p. 033632.

[42] J. L. Holzbauer. *The Muon g-2 Experiment Overview and Status*. 2017. arXiv: `1712.05980 [hep-ex]`.

[43] Piotr Jaworski et al. "Picosecond and nanosecond pulse delivery through a hollow-core Negative Curvature Fiber for micro-machining applications". In: *Opt. Express* 21.19 (Sept. 2013), pp. 22742–22753.

[44] A. M. Jeffery et al. "NIST comparison of the quantized Hall resistance and the realization of the SI OHM through the calculable capacitor". In: *IEEE Transactions on Instrumentation and Measurement* 46.2 (1997), pp. 264–268.

[45] Yonatan Kahn et al. "Light weakly coupled axial forces: models, constraints, and projections". In: *Journal of High Energy Physics* 2017.5 (2017), p. 2.

[46] Mark Kasevich and Steven Chu. "Atomic interferometry using stimulated Raman transitions". In: *Phys. Rev. Lett.* 67 (1991), pp. 181–184.

[47] Andrew James Kerman. "Raman sideband cooling and cold atomic collisions in optical lattices". PhD thesis. Stanford University, Jan. 2002.

[48]   Andrey R. Kolovsky and Hans Jürgen Korsch. "BLOCH OSCILLATIONS OF COLD ATOMS IN OPTICAL LATTICES". In: *International Journal of Modern Physics B* 18.09 (2004), pp. 1235–1260.

[49]   T. Kovachy et al. "Quantum superposition at the half-metre scale". In: *Nature* 528 (Dec. 2015), p. 530.

[50]   Tim Kovachy et al. "Optical lattices as waveguides and beam splitters for atom interferometry: An analytical treatment and proposal of applications". In: *Phys. Rev. A* 82 (1 July 2010), p. 013638.

[51]   E Krüger, W Nistler, and W Weirauch. "Determination of the fine-structure constant by a precise measurement of h/m_n : the final result". In: *Metrologia* 35.3 (1998), p. 203.

[52]   Pei-Chen Kuan. "Compton clock and recoil frequency measurements using a large momentum transfer atom interferometer". PhD thesis. University of California, Berkeley, 2013.

[53]   Shau-Yu Lan et al. "Influence of the Coriolis Force in Atom Interferometry". In: *Phys. Rev. Lett.* 108 (2012), p. 090402.

[54]   Stefano Laporta. "High-precision calculation of the 4-loop contribution to the electron g-2 in QED". In: *Physics Letters B* 772 (2017), pp. 232–238.

[55]   J. P. Lees and *et al.* "Search for Invisible Decays of a Dark Photon Produced in e^+e^- Collisions at BaBar". In: *Phys. Rev. Lett.* 119 (2017), p. 131804.

[56]   V. S. Malinovsky and J. L. Krause. "General theory of population transfer by adiabatic rapid passage with intense, chirped laser pulses". In: *The European Physical Journal D - Atomic, Molecular, Optical and Plasma Physics* 14.2 (2001), pp. 147–155.

[57]   Peter J. Mohr, David B. Newell, and Barry N. Taylor. "CODATA recommended values of the fundamental physical constants: 2014". In: *Rev. Mod. Phys.* 88 (2016), p. 035009.

[58]   Peter J. Mohr and Barry N. Taylor. "CODATA recommended values of the fundamental physical constants: 1998". In: *Rev. Mod. Phys.* 72.2 (2000), pp. 351–495.

[59]   H. Müller et al. "A new photon recoil experiment: towards a determination of the fine structure constant". In: *Applied Physics B* 84.4 (Sept. 2006), pp. 633–642.

[60]   Holger Müller, Sheng-wey Chiow, and Steven Chu. "Atom-wave diffraction between the Raman-Nath and the Bragg regime: Effective Rabi frequency, losses, and phase shifts". In: *Phys. Rev. A* 77 (2 Feb. 2008), p. 023609.

[61]   Anna M. Nobili. "Fundamental limitations to high-precision tests of the universality of free fall by dropping atoms". In: *Phys. Rev. A* 93 (2 Feb. 2016), p. 023617.

[62]   E. B. Norrgard et al. "In-vacuum scattered light reduction with black cupric oxide surfaces for sensitive fluorescence detection". In: *Review of Scientific Instruments* 87.5 (2016), p. 053119.

[63] Shin-ichi Ohshima et al. "Cesium Atomic Fountain with Two-Dimensional Moving Molasses". In: *Japanese Journal of Applied Physics* 34.Part 2, No. 9A (Sept. 1995), pp. L1170–L1173.

[64] Chris Overstreet et al. "Effective Inertial Frame in an Atom Interferometric Test of the Equivalence Principle". In: *Phys. Rev. Lett.* 120 (18 May 2018), p. 183604.

[65] Richard H. Parker et al. "Controlling the multiport nature of Bragg diffraction in atom interferometry". In: *Phys. Rev. A* 94 (5 Nov. 2016), p. 053618.

[66] Richard H. Parker et al. "Measurement of the fine-structure constant as a test of the Standard Model". In: *Science* 360.6385 (2018), pp. 191–195.

[67] C. Patrignani and Particle Data Group. "Review of Particle Physics". In: *Chinese Physics C* 40.10 (2016), p. 100001.

[68] Ekkehard Peik et al. "Bloch oscillations of atoms, adiabatic rapid passage, and monokinetic atomic beams". In: *Phys. Rev. A* 55 (4 Apr. 1997), pp. 2989–3001.

[69] A Peters, K Y Chung, and S Chu. "High-precision gravity measurements using atom interferometry". In: *Metrologia* 38.1 (), p. 25.

[70] Achim Peters, Keng Yeow Chung, and Steven Chu. "Measurement of gravitational acceleration by dropping atoms". In: *Nature* 400 (1999), pp. 849–852.

[71] A. K. Potemkin et al. "Spatial filters for high-peak-power multistage laser amplifiers". In: *Appl. Opt.* 46.20 (July 2007), pp. 4423–4430.

[72] E. L. Raab et al. "Trapping of Neutral Sodium Atoms with Radiation Pressure". In: *Phys. Rev. Lett.* 59 (23 Dec. 1987), pp. 2631–2634.

[73] F. Riehle et al. "Optical Ramsey spectroscopy in a rotating frame: Sagnac effect in a matter-wave interferometer". In: *Phys. Rev. Lett.* 67 (2 July 1991), pp. 177–180.

[74] Wolfgang A. Rolke, Angel M. López, and Jan Conrad. "Limits and confidence intervals in the presence of nuisance parameters". In: *Nuclear Instruments and Methods in Physics Research Section A: Accelerators, Spectrometers, Detectors and Associated Equipment* 551.2 (2005), pp. 493–503.

[75] G. Rosi et al. "Precision measurement of the Newtonian gravitational constant using cold atoms". In: *Nature* 510 (2014), pp. 518–521.

[76] Albert Roura. "Circumventing Heisenberg's Uncertainty Principle in Atom Interferometry Tests of the Equivalence Principle". In: *Phys. Rev. Lett.* 118 (16 Apr. 2017), p. 160401.

[77] D. Schlippert et al. "Quantum Test of the Universality of Free Fall". In: *Phys. Rev. Lett.* 112 (20 May 2014), p. 203002.

[78] C. Schwob et al. "Optical Frequency Measurement of the $2S - 12D$ Transitions in Hydrogen and Deuterium: Rydberg Constant and Lamb Shift Determinations". In: *Phys. Rev. Lett.* 82 (25 June 1999), pp. 4960–4963.

[79] Daniel Steck. "Cesium D line data". In: (Jan. 2010).

[80] Daniel Adam Steck. *Quantum and Atom Optics*. 2007.

[81] Pippa Storey and Claude Cohen-Tannoudji. "The Feynman path integral approach to atomic interferometry. A tutorial". In: *Journal De Physique Ii* 4 (Nov. 1994), pp. 1999–2027.

[82] Alex Sugarbaker et al. "Enhanced Atom Interferometer Readout through the Application of Phase Shear". In: *Phys. Rev. Lett.* 111 (11 Sept. 2013), p. 113002.

[83] M. G. Tarallo et al. "Test of Einstein Equivalence Principle for 0-Spin and Half-Integer-Spin Atoms: Search for Spin-Gravity Coupling Effects". In: *Phys. Rev. Lett.* 113 (2 July 2014), p. 023005.

[84] Vincent Trudel and Yves St-Amant. "One-dimensional single-mode fiber-optic displacement sensors for submillimeter measurements". In: *Appl. Opt.* 48.26 (Sept. 2009), pp. 4851–4857.

[85] P. J. Ungar et al. "Optical molasses and multilevel atoms: theory". In: *J. Opt. Soc. Am. B* 6.11 (Nov. 1989), pp. 2058–2071.

[86] Robert S. Van Dyck, Paul B. Schwinberg, and Hans G. Dehmelt. "New high-precision comparison of electron and positron g factors". In: *Phys. Rev. Lett.* 59 (1987), pp. 26–29.

[87] D. S. Weiss, B. C. Young, and S. Chu. "Precision measurement of $\hbar/m_{\mathrm{Cs}}$ based on photon recoil using laser-cooled atoms and atomic interferometry". In: *Applied Physics B* 59.3 (Sept. 1994), pp. 217–256.

[88] David S. Weiss, Brenton C. Young, and Steven Chu. "Precision measurement of the photon recoil of an atom using atomic interferometry". In: *Phys. Rev. Lett.* 70 (18 May 1993), pp. 2706–2709.

[89] David S. Weiss et al. "Optical molasses and multilevel atoms: experiment". In: *J. Opt. Soc. Am. B* 6.11 (Nov. 1989), pp. 2072–2083.

[90] Martin Weitz, Brenton C. Young, and Steven Chu. "Atomic Interferometer Based on Adiabatic Population Transfer". In: *Phys. Rev. Lett.* 73 (19 Nov. 1994), pp. 2563–2566. DOI: 10.1103/PhysRevLett.73.2563. URL: https://link.aps.org/doi/10.1103/PhysRevLett.73.2563.

[91] Andreas Wicht et al. "A Preliminary Measurement of the Fine Structure Constant Based on Atom Interferometry". In: *Physica Scripta* 2002 (2002), p. 82.

[92] E. R. Williams et al. "A low field determination of the proton gyromagnetic ratio in water". In: *IEEE Transactions on Instrumentation and Measurement* 38.2 (1989), pp. 233–237.

[93] Jason Williams et al. "Quantum test of the equivalence principle and space-time aboard the International Space Station". In: *New Journal of Physics* 18.2 (2016), p. 025018.

[94]   Mingjie Xin et al. "An atom interferometer inside a hollow-core photonic crystal fiber". In: *Science Advances* 4 (2018).

[95]   Chenghui Yu. "Measuring the fine structure constant with a state-of-the-art atom interferometer". PhD thesis. University of California, Berkeley, 2018.

[96]   Chenghui Yu et al. "Atom-Interferometry Measurement of the Fine Structure Constant". In: *Annalen der Physik* 0.0 (), p. 1800346.

[97]   Clarence Zener and Ralph Howard Fowler. "Non-adiabatic crossing of energy levels". In: *Proceedings of the Royal Society of London. Series A, Containing Papers of a Mathematical and Physical Character* 137.833 (1932), pp. 696–702.

[98]   Weicheng Zhong et al. "Offset simultaneous conjugate atom interferometers". In: *Phys. Rev. A* 101 (5 May 2020), p. 053622.

[99]   Lin Zhou et al. "Test of Equivalence Principle at 10^{-8} Level by a Dual-Species Double-Diffraction Raman Atom Interferometer". In: *Phys. Rev. Lett.* 115 (1 July 2015), p. 013004.

[100] Fei Zi et al. "Laser frequency stabilization by combining modulation transfer and frequency modulation spectroscopy". In: *Appl. Opt.* 56.10 (Apr. 2017), pp. 2649–2652.